Laminar vortex shedding past a flat plate at 90°

An experimental study on the effects of acceleration and viscoelasticity

Ilambharathi Govindasamy

Delft University of Technology

TU Delft

Laminar vortex shedding past a flat plate at 90°

An experimental study on the effects of acceleration and viscoelasticity

by

Ilambharathi Govindasamy

to obtain the degree of Master of Science
at the Delft University of Technology
to be defended publicly on
Friday, September $16^{\text{th}}, 2022$ at 1 PM

Student number:	5352797	
Project Duration:	November 2021 - September 2022	
Supervisor:	Dr. Abel-John Buchner	TU Delft
Thesis committee:	Prof.dr.ir. Johan T Padding	TU Delft
	Prof.dr.ir. Willem Van De Water	TU Delft
	ir. Jesse Reijtenbagh	TU Delft

TU Delft

Acknowledgments

First and foremost, I would like to wholeheartedly thank *Dr.Abel-John Buchner* for his guidance throughout my internship and thesis. I cannot thank enough for the detailed and thought-provoking discussions in every weekly meeting and, most of all, for all the freedom, encouragement and support to try out different things. Although there were challenges throughout the thesis, it never felt like a struggle after discussing further directions with him; he made sure I did not get into rabbit holes of research. I am highly grateful to him for introducing to me, a variety of techniques in the fluid dynamics, sources to learn from and all the support to attend seminars and symposium. Apart from technicalities, I sincerely thank him for his inspiring as an academic researcher and mentor.

I would also like to thank *Jesse* for many suggestions on literature, clear questions and fruitful discussions about accelerating flows.

I sincerely thank *Jan* for helping me with the linear traverse and *Jasper* for timely support while building the experimental setup. The experimental setup would not have been possible without the support of *Edwin,* and special thanks to him for sharing his expertise in PIV.

I would like to thank *Prof. Willem Van De Water* for his discussions on LCS and interesting aspects of causality in fluid flows, *Prof. Johan Padding* for his discussions on Time-Temperature-superposition principle and viscoelasticity, *Yavuz* for sharing his expertise and helpful discussions on Rheology, *Sowmya* for her very clear questions on fluid physics, that helped me to reflect and arrange my thoughts. I am extremely grateful to *Fulin* and *Kavya* for their discussions and a great company throughout my thesis. I am grateful to everyone in *the Laboratory of Aero & Hydrodynamics* for their consistent support, and sharing their knowledge. I sincerely thank *Surya* for daily discussions on fluid dynamics, sharing his knowledge, and interesting aspects of interfacial phenomena.

I would like to extend my sincere gratitude to *Dr.Wim-Paul Breugem*, *Prof. Jerry Westerweel* , and *Dr.Daniel Tam* for their inspiring lectures and challenging problems during my coursework that motivated me to work on fluid flows.

This journey would not have been possible without the support of my friends and family. I specially thank my friends *Karthik*, *Adithya*, *Shiva*, *Raj*, *Bhagya* and *Nikita*, for their company, support, and good times. Finally, and the most important of all, I thank my parents for their support.

Ilambharathi Govindasamy
Delft, September 2022

Abstract

Fluid flows such as rowing and animal flight involve both acceleration and vortex shedding. Some of such flows also involve complex fluids, as in blood flow from left atrium into the left ventricle in a human heart. Among the complexities of such fluids, we are interested in the viscoelastic nature. The effect of acceleration in vortex dynamics and forces has been studied for a long time. However, there have been discrepancies in the origin of the unsteady forces and modelling them. It is still not very well understood how unsteady forces scale in laminar, highly separated flows? On the other hand, the presence of viscoelasticity alters the vortex dynamics and hence the forces. It has been well studied how the viscoelasticity may affect steady state forces. However, the change in vortex dynamics and forces due to presence of viscoelasticity during acceleration is not well understood. This experimental study aims to add to the literature on unsteady force modelling, effect of viscoelasticity in unsteady forces and vortex dynamics. To begin with, shear and extensional rheological experiments were performed to identify a weakly elastic fluid. An experimental setup was built with a linear traverse, PIV system and force sensor. The experiments were performed with an accelerating flat plate (aspect ratio of two), in the identified viscoelastic fluid and also in a viscosity matched Newtonian fluid for one-one comparison. To understand the vortex dynamics, we use FTLE fields, Lamb-Oseen model, and Q-criteria. We quantify the vortex formation time and other properties of a vortex ring. Overall, we observe that both the vortex growth rate and the decay rate are enhanced by the presence of viscoelasticity. We extend the idea of optimal vortex formation to two time-scales instead of one. One, when the plate no longer provides energy and the other, when the vortex is filament free without any more addition of coherent fluid parcels. Furthermore, a limit for optimal vortex formation is proposed to indicate a completely different type of vortex dynamics at lower accelerations. The drag reduction and enhancement due to the presence of viscoelasticity qualitatively agrees well with the trend in literature. In terms of unsteady forces, we try to interpret an equivalent mass for potential flow's added mass in separated Newtonian flows. We propose a model using wake's mass, and it reasonably agrees with our experimental results in Newtonian cases. We use FTLE ridges and vortex-frame streamlines to estimate wake mass, along with a literature driven model for third dimension. We also propose that the added mass in separated flows is time varying and eventually reaches a constant value. Furthermore, the effect of viscoelasticity is primarily observed in unsteady forces for acceleration less than optimal vortex formation limit.

Contents

Nomenclature

Symbols

Symbol	Definition	Unit
u	Velocity	[m/s]
u_∞	Free stream velocity	[m/s]
U_{plate}	Plate's velocity	[m/s]
m_h	Hydrodynamic mass	[kg]
m_p	Plate mass	[kg]
m_{wake}	Wake mass	[kg]
a	Acceleration	[m/s^2]
T	Temperature	[K]
N_1	First normal stress difference	[N/m^2]
N_2	Second normal stress difference	[N/m^2]
F_n	Normal Force	[N]
R	Radius	[m]
G'	Storage modulus	[N/m^2]
G''	Loss modulus	[N/m^2]
G^*	Complex modulus	[N/m^2]
G	Modulus	[N/m^2]
R_g	Universal gas constant	[kgm^2/s^2.K.mol]
M_w	Molecular weight	[g/mol]
c	Concentration	[ppm]
D	Filament thread diameter	[m]
K	Flow consistency index	[mPa.s]
n	Power law constant	[-]
a	Transition parameter	[-]
g	Gravitational acceleration	[m/s^2]
p	Pressure	[[N/m^2]
L_c	Geometric characteristic length	[m]
F	Force	[N]
m	Mass	[kg]
F_D	Drag force	[N]
F_L	Lift force	[N]
A	Area	[m^2]
f_s	Vortex shedding frequency	[1/s]
A_p	projected area of geometry	[m^2]
A_t	Cross-section area of test section	[m^2]
L_f	Vortex formation length	[m]
s	Length of vortices from the rear end	[m]
c_s	Speed of viscoelastic shear waves	[m/s]

Symbol	Definition	Unit
ρ	Density	[kg/m^3]
η	Shear viscosity	[Ns/m^2]
η_0	Zero Shear viscosity	[Ns/m^2]
η_∞	Infinite Shear viscosity	[Ns/m^2]
η_p	Intrinsic polymer viscosity	[Ns/m^2]
η_s	Solvent viscosity	[Ns/m^2]
η^*	Complex Shear viscosity	[Ns/m^2]
η_e	Extensional viscosity	[Ns/m^2]
σ	Total stress	[N/m^2]
τ	Shear stress	[N/m^2]
$\dot{\gamma}$	Shear strain rate	[1/s]
$\dot{\epsilon}$	Extensional strain rate	[1/s]
Ψ_1	First Normal stress difference coefficient	[Ns^2/m^2]
Ψ	Stream function	[m^2/s]
ω	Angular frequency	[1/s]
λ	Characteristic Relaxation time	[s]
λ_z	Zimm Relaxation time	[s]
λ_m	Maxwell Relaxation time	[s]
λ_o	Oldroyd-B Relaxation time	[s]
λ_e	Extensional Relaxation time	[s]
λ_r	Retardation time	[s]
σ_t	Surface tension	[N/m]
Γ	Circulation	[m^2/s]
$^\triangledown$	Upper convected time derivative	[1/s]
$\boldsymbol{\omega}$	Vorticity	[radians/s]
ν	Kinematic viscosity	[m^2/s]
δ	Boundary layer thickness	[m]
$\boldsymbol{\gamma}$	Strength of vortex sheet	[m/s]

Dimensionless numbers

Symbol	Name
Re	Reynolds number
Tr	Troutan ratio
C_D	Drag coefficient
C_L	Lift coefficient
St	Strouhal number
BR	Blockage ratio
AR	Aspect ratio
t_f	FTLE based Vortex formation time
t_v	Non-dimensional viscous diffusion time
t_a	Acceleration time
Wi	Weissenburg number
De	Deborah number
El	Elastic number
M	Viscoelastic mach number
Stk	Stokes number
α	Dimensionless acceleration
β_r	Viscosity ratio
C_x	Added mass coefficient
T^*	Non-dimensional distance/time travelled by plate
T_a^*	Non-dimensional acceleration distance/time
E^*	Vorticity distribution based energy
D_v^*	Non-dimensional vortex ring diameter
D_c^*	Non-dimensional vortex core diameter
U^*	Non-dimensional velocity

Abbreviations

Abbreviation	Definition
SAOS	Small Amplitude Oscillatory Shear
LVE	Linear Viscoelastic
CFD	Computational Fluid Dynamics
PAM	Polyacrylamide
NaCl	Sodium Chloride
ppm	parts per million
PIV	Particle Image Velocimetry
FTLE	Finite Time Lyapunov exponent
LCS	Lagrangian coherent structures
LAVD	Lagrange Averaged Vorticity Deviation
3D	Three dimensional
2D	Two dimensional
1D	One dimensional

List of Figures

List of Tables

1

Introduction

Vortex shedding is a classic phenomenon in fluid dynamics that we come across every day, in the form of a cyclone, wake of flying and swimming animals, etc. To put it simply, the region in a flow where fluid revolves around an axis can be termed as a vortex. When fluid flows past a bluff geometry that opposes flow streamlines, vortices form, grow and eventually lead to vortex shedding. This phenomenon has wide impacts in the living world such as Jellyfish propulsion, swimming, drag acting over a car and cyclist, etc. Hence, a large amount of research was done in the last century to understand the dynamics of the flow separation at the geometry, wake (disturbed flow region downstream of the geometry) and the associated forces. One of the most notable people in fluid dynamics, Theodore Von Kármán, studied vortex shedding due to flow past a cylinder and observed a repeating pattern of swirling vortices, which are now termed as Von Kármán vortex street. An example of such a naturally occurring Von Kármán vortex street is shown in Figure 1.1.

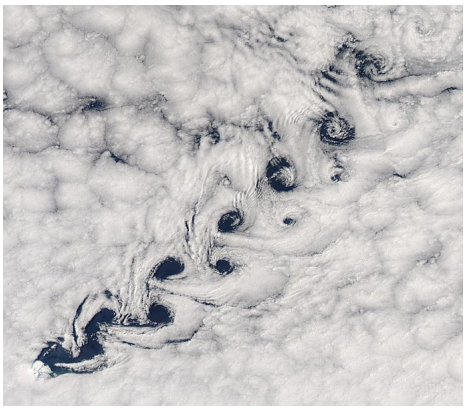

Figure 1.1: Kármán vortex street around Heard Island. This figure is taken from [1]

Early steps to understand these dynamics started with fundamental studies in canonical geometries. If a geometry opposes flow streamlines, it is called a bluff body, whereas a geometry that is aligned with streamlines is called a streamlined body. In bluff bodies, cylinder and flat plate (oriented 90°to flow) are widely used as the canonical geometry. The flat plate has been investigated mostly involving unsteady kinematics for their significance in drag based propulsion of various systems like rowing[2], insect flight, and micro air vehicles[3]. It is important to note that flat plates, oriented 90°to flow have a fixed point of flow separation, unlike curved geometries such as cylinder. The fixed separation point is due to the inability of highly inertial fluid ($Re \gtrapprox 50$) to change the flow direction instantaneously at sharp edges; whereas the Reynolds number (Re) is defined as the ratio of inertial forces to viscous forces. Therefore, flat plate can be preferred over cylinder as it is easier to study a sharp-edged separation compared to a curved section with moving separation point. Vortex shedding behind such bodies is not only seen in simple fluids like water and air, but also other complex fluids like blood, polymers etc.

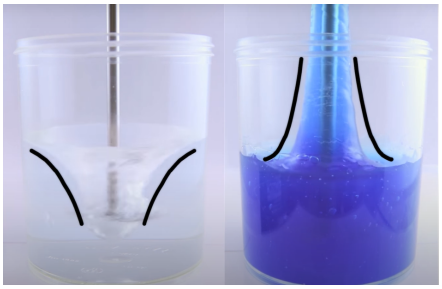

Figure 1.2: Rod climbing effect: Newtonian water (left) behaves differently than Non-Newtonian polyethylene oxide in water (right), when a rotating rod is inserted. Newtonian fluid experience being thrown outward, whereas positive normal stresses are induced in the Non-Newtonian fluid, drawing fluid towards and up the rod. This figure is taken from[5]

1.1. Viscoelastic fluids

Fluids like water, and air consist of small molecules with simple structures. These fluids have a constant viscosity for any applied shear stress, following Newton's law of viscosity, and so they are termed as Newtonian fluids. However, many fluids in nature do not show such a simple behaviour due to the presence of large internal structures, which are often caused by large molecules. These type of fluids are called Non-Newtonian fluids. Some examples include, paint, mucus, polymer solutions and wheat dough, etc[4]. Many types of Non-Newtonian fluids exist, often as a combination of viscoelasticity (decaying elastic memory), time dependent viscosity and stress dependent viscosity. In the Non-Newtonian fluids involving viscoelasticity, many notable studies have been done in both polymer fluids and biofluids. Unlike Newtonian fluids, viscoelastic fluids exhibit peculiar effects such as Rod climbing/Weissenberg effect (refer Figure1.2) due to the presence of normal stress differences caused by viscoelasticity. The normal stress differences are caused as an effect of polymer relaxation in viscoelastic fluids. When such normal stress differences exist, it will be interesting to see how vortex shedding is affected, compared to a Newtonian fluid. Let's first discuss the relevance of viscoelastic vortices to real world applications to motivate the study.

1.2. Motivation

Microscale collective flows

Viscoelastic flows are studied in both micro and macro scale. Inspired from nature, various robotic microswimmers have been developed for biomedical applications such as microsurgery, drug delivery, etc[6]. To further understand and advance such microswimmers, many studies focused on microbe-biofluid interactions, which are often viscoelastic. In collective behaviour of pusher swimmers, vortex structures are found to be suppressed, whereas swimmer aggregation is enhanced in the presence of viscoelasticity [7]. These microswimmers however, operate mostly in inertia-less viscoelastic regimes.

Red mud transport

Viscoelastic polymer solutions also have wide applications in macro flows, one such example is using viscoelasticity for red mud transport in pipes without clogging[8]. In such cases of viscoelastic transport, it is critical to understand the vortex dynamics, as the viscoelastic effects may affect the local separation regions at pipe junctions or bends. Often, red mud waste produced during alumina production were stored in large dams because of difficulty in transport and sometimes resulted in deadly accidents like 'Hungarian red mud disaster' causing casualties, long term economical and ecological damage[9]. Although, viscoelastic transport provide a safer solution to avoid such disasters, it is important to understand the change in local vortex dynamics that it may bring along.

Flocculation

Polymer additives are also used in waste water treatment as flocculants to bind the suspensions together [10] and flocculation is enhanced by mixing the solution with the help of impeller shed vortices [11]. Thus, a viscoelastic solution during flocculation involves vortex dynamics and may even affect the impeller forces required.

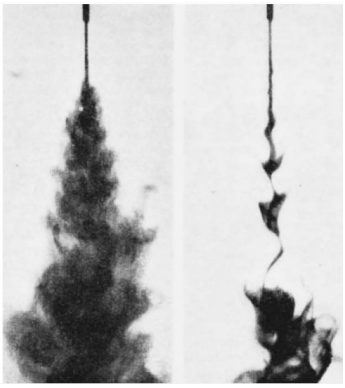

Figure 1.3: Turbulent jet mixing in water (Newtonian-left) and dilute Polyox solution (Viscoelastic-right) shows that viscoelasticity suppresses mixing. This figure is taken from[13]

Turbulent drag reduction & Mixing inhibition
When high molecular weight polymers are added to a Newtonian fluid, the drag acting in turbulent pipe flow is reduced, thus saving pumping energy[12]. As turbulent flows are made up of vortices that form and evolve continuously, understanding vortex dynamics is critical to interpret the mechanisms of drag reduction. On the other hand, it has a negative effect on mixing as the typical turbulent structures are suppressed as shown in Figure 1.3 [13], which would mean more energy is required for mixing these solutions.

Blood flows
The viscoelastic effects on vortex dynamics can also provide insights on blood flows in heart and arteriovenous fistula, since blood is also viscoelastic. Blood's viscoelastic behaviour is a due to the presence of large protein molecules and deformation of red blood cells [14, 15]. Interestingly, it has been reported that vortex rings formed in a healthy heart follows the optimal vortex formation as in starting propulsive vortex rings in Newtonian fluids, which will be discussed in later chapters [16] (see Figure 1.4).

Viscoelastic effect on unsteady vortex dynamics and forces
All the aforementioned applications, do not always occur in steady flow regimes, which has been well investigated for both viscoelastic and Newtonian cases. They also act in accelerating flows such as startup of the system, pulsating flows and propulsion. Despite their widespread applications discussed so far, a clear understanding of viscoelastic vortex dynamics and force changes in accelerating flows is still scarce to the best of our knowledge. Hence, this study aims to understand the vortex dynamics due to an accelerating flat plate in a constant viscosity viscoelastic fluid (see section.2.9) compared to a Newtonian fluid and their implications in forces. In this study, a flat plate oriented normal to its direction of motion shall be used to understand the effect of viscoelasticity and acceleration in vortex dynamics and corresponding forces.

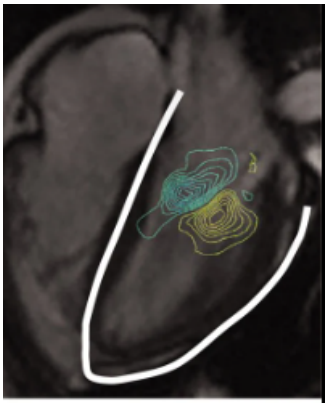

Figure 1.4: Vorticity contours: Optimally formed vortex ring during diastole in heart. This figure is taken from[16]

2

Background & Literature review

In order to study viscoelastic effects on vortices and forces, the theory and state of current literature will be discussed in this chapter. The discussion will include vortex dynamics, relevant forces, viscoelastic theory and viscoelastic effects on vortex dynamics and forces.

2.1. Vortex dynamics

Let's first define some important terminologies to understand and study vortex dynamics.

2.1.1. What is a vortex?

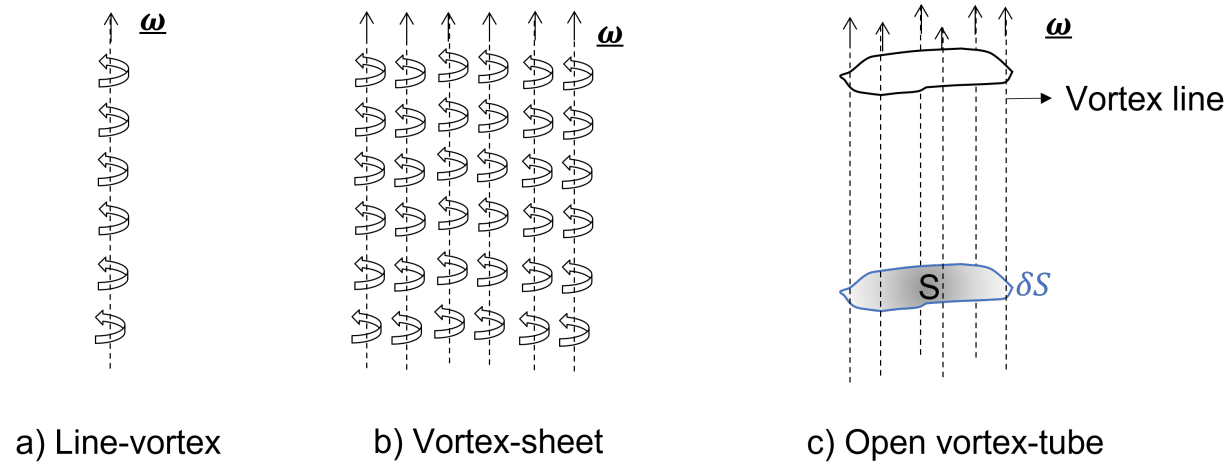

Figure 2.1: Fluid parcels aligned as a line vortex(a), line vortices arranged as a vortex sheet (b), Vortex sheet rolled up as a vortex tube(c). These figures are self-made inspired from [17]

The most important term to begin with is vorticity, which is conventionally defined as the curl of velocity, $\underline{\omega} = \underline{\nabla} \times \underline{u}$ and a concentration of codirectional vorticity can be called as a vortex. In reality, a region of non-zero vorticity can be interpreted as a set of fluid parcels experiencing an angular/rotational motion, since angular velocity of a fluid parcel is the half of its vorticity. In other words, a local region without any vorticity is called irrotational and otherwise is rotational. Based on this definition, ideal vortices can be classified as rotational and irrotational vortices. In rotational vortex, fluid parcel rotate about themselves and revolve around an axis, in crude words, similar to earth around the sun. On the other hand, in an irrotational vortex (not physically realizable) fluid parcels do not rotate about their own axis but only around a fixed centre with decreasing velocity along the radial direction. The dynamics of

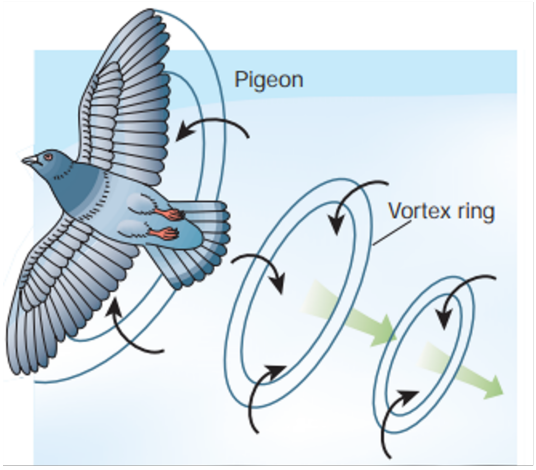

a) Vortex ring of pigeon

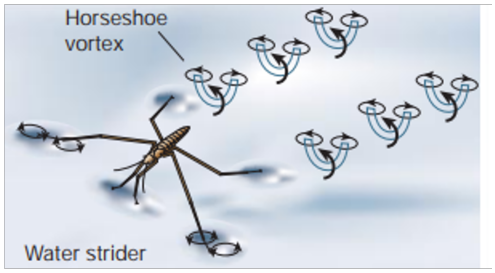

a) Half vortex ring of water strider

Figure 2.2: Vortex ring formed due to finite size and wing symmetry in a pigeon(a), U-shaped ring formed due to surface discontinuity in a water strider(b).This figure is taken from[19]

vorticity can be expressed by applying curl to the Navier-Stokes equation (Equation 2.36),

$$\frac{D\underline{\boldsymbol{\omega}}}{Dt} = (\underline{\boldsymbol{\omega}} \cdot \underline{\nabla})\underline{u} + \nu\nabla^2(\underline{\boldsymbol{\omega}}) \tag{2.1}$$

The left-hand side characterizes the motion of the vorticity due to advection and local time variations, whereas $\nu\nabla^2(\underline{\boldsymbol{\omega}})$ refers to the diffusion of the vorticity and $(\underline{\boldsymbol{\omega}} \cdot \underline{\nabla})\underline{u}$ refers to the tilting and stretching of vorticity which occurs only in three dimensions. The lines drawn tangent to the vorticity vector can be called as vortex lines, and a large set of them parallel to each other is a vortex sheet. When vortex sheets roll up forming a cylindrical material volume, it can be called as a vortex tube [17, 18] as visualized in Figure2.1.The vortex tubes have a constant strength across any cross-section, similar to volume flow rate in a tube and this strength is called as circulation Γ, defined as the flux of vorticity

$$\Gamma = \oint_{\delta S} \underline{u}.\underline{dl} = \iint_S \underline{\boldsymbol{\omega}}.\hat{n}dA \tag{2.2}$$

As a consequence of constant circulation, the vortex tube can be a closed loop or infinitely long or end at solid boundary or discontinuity. Such examples can be found in nature, as in Figure 2.2[19]. A closed vortex line is often formed because of the flow symmetry, and the resulting closed tube can be called a vortex ring[18].

2.1.2. Laws of vortex motion

In 1858, Helmholtz published Helmholtz-vortex theorems on vortex motion in an *ideal inviscid barotropic flow* with conservative body forces, described as follows[17, 18]:

- Vortex lines/tubes move with the fluid. They can only be a closed loop, infinitely long or end at boundaries.
- Circulation is constant along the length of a vortex tube and in time
- Fluid parcels originally free of vorticity, remain so

The aforementioned laws can also be approached using kelvin's circulation theorem, defined as "In an *inviscid, barotropic flow with conservative body forces*, the circulation around a closed curve moving with the fluid remains constant with time" for a closed contour[17].

$$\frac{D\Gamma}{Dt} = 0 \tag{2.3}$$

This can be extended to a viscous fluid by substituting equation 2.2 for Γ, and the right-hand side of the Navier-Stokes equation by assuming the fluid to be *barotropic and incompressible*, we get[20]

$$\frac{D\Gamma}{Dt} = \nu \oint_{\delta S} \nabla^2 \underline{u}.d\underline{x} = \nu \oint_{\delta S} (\underline{\nabla}(\underline{\nabla}.\underline{u}) - \underline{\nabla} \times \underline{\boldsymbol{\omega}}).d\underline{x} = \nu \iint \nabla^2 \underline{\boldsymbol{\omega}}.\hat{n}dA \tag{2.4}$$

where $\nu = \eta/\rho$, is the kinematic viscosity. Thus, in real fluids with viscosity, the vortex core (solid-body like rotating fluid parcels) will be influenced by viscosity and there exists an irrotational region outside the core region. Vortices have high energy due to rotating fluid parcels, and so they lose energy by viscous dissipation in the core. This region of viscous dissipation around a vortex follows[21],

$$\frac{dE}{dt} = -\nu \iiint \boldsymbol{\omega}^2 dV \tag{2.5}$$

where E is the kinetic energy and dV is the control volume around the core.When there is no energy input, the vortex core expands and gradually becomes a rigid body motion surrounded by irrotational flow. Such a decaying vortex can be modelled using Lamb-Oseen vortex, which can be derived from vorticity equation in 2D (without stretching/tilting) with circular symmetry and an initial condition of $\underline{\boldsymbol{\omega}} = \Gamma_0\ \delta x \delta y$. The exact solution is[18],

$$u_\theta = \Gamma/2\pi r \tag{2.6}$$

$$\Gamma = \Gamma_0(1 - e^{-r^2/4\nu t}) \tag{2.7}$$

where u_θ is the tangential velocity and the radius of the viscous core, $R_c = \sqrt{4\nu t}$ which changes over time due to viscous diffusion. In unsteady flows, the vortex core radius and circulation can be estimated by fitting the ideal Lamb-Oseen model, when the vortex core centre is identified[22]. It could be noted that circulation decay, dissipation of kinetic energy and diffusion of vorticity in above equations are simply viscous stress effects in different representations. Speaking in terms of kinetic energy using the mean kinetic energy equation *without fluctuations* (see Turbulence section of [17]), the viscous stress can be written as a sum of diffusive energy transport and energy dissipation, in which the aforementioned dissipation equation only represents the dissipation component. The vortex tubes also induce a velocity around them due to the circulation it has, and it can be estimated using Biot-Savart's law[17].

2.1.3. Vortex ring

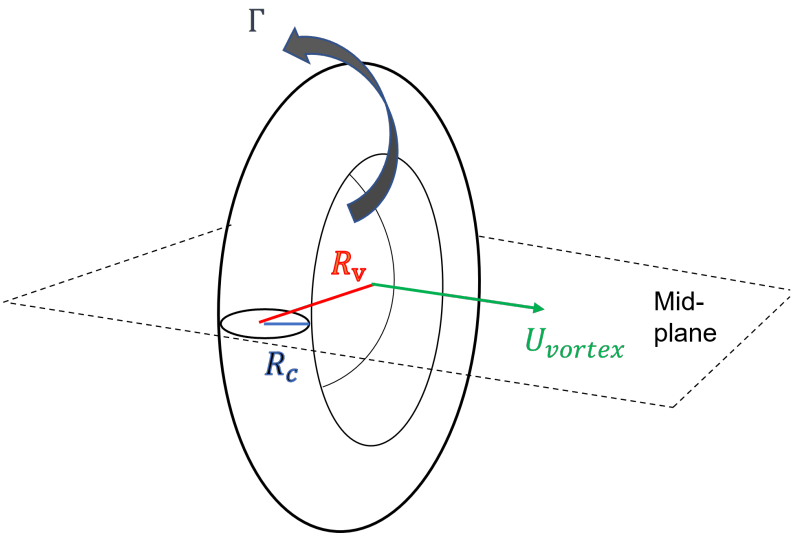

Figure 2.3: A Circular vortex ring with circulation Γ, radius R_v,core radius R_c and translational velocity U_{vortex}. This figure is self-made

As we discussed so far, a vortex filament (a strip of concentrated vorticity) can form a tube that is infinitely long, end at boundaries or loop to form a ring. In most real life applications, such as human heart, animal flight, Dandelion flight, fish swimming, etc[16, 19], the ratio of major to minor axis of

a geometry is finite. Such geometries very often does not have a nearby boundary to end the tube, resulting in vortex rings. Even in flow past a normal flat plate at small major to minor axis ratio similar to the aforementioned applications, vortex rings are formed. A vortex ring is characterized by vortex ring radius R_v ($= D_v/2$), vortex core radius R_c ($= D_c/2$), translational velocity of vortex ring U_{vortex}, circulation Γ and Energy E_{vortex} of the vortex ring. An example of such a vortex ring is illustrated in Figure.2.3

Drag vs Propulsive vortex rings

Fortunately, a lot of analytical and experimental studies were conducted in the past decades on vortex rings[18, 23]. However, the majority of experimental works are based on the propulsive vortices, where a piston cylinder setup is used to propel the fluid and the flow gets separated at the sharp edges to form a vortex ring [23]. Recently, there have been a few studies on drag vortex rings (formed due to flow past a bluff body) mainly in the context of biomimetics and added mass, but at relatively high Reynolds numbers[2, 24, 25]. The propulsive vortices reach their maximum energy, separates and outpaces the shear layer at the same time, so understanding the causality is difficult. By using drag vortices, it has been found that vortex pinch-off does not necessarily cause the maximum vortex energy and the theoretical velocity of these vortex rings based on steady case were found to match the experimental data very well. Furthermore, the dimensionless energy, translational velocity and circulation were reaching constant value in their experimental window [24]. A notable distinction between drag and propulsive vortices is that the induced translational velocity would be pointed towards the source in drag vortices and away from the source in propulsive vortices.

Parameters of a vortex ring

For a circular steady vortex ring, analytical solutions exist to calculate the corresponding energy and translational velocity when Γ, R_c and R_v are measured using along a cross-sectional plane of the vortex ring. It will be interesting to see how far circular steady vortex ring equations for U_{vortex} can predict the behaviour of equivalent elliptical steady vortex rings with different major and minor axis and their applicability to viscoelastic cases. The early equation for translational velocity of thin vortex rings was given by Lord Kelvin[18]. However, in experiments with propulsive vortices, Fraenkel's second order velocity equation has been successfully used at relatively high Reynolds numbers[26].It has been reported that at relatively low Reynolds numbers, these equations does not hold due to thicker core and so, a new relation was proposed based on experimental findings[27].

$$U_v^* = \frac{16\pi}{k}(D^*)^{-3/2} \tag{2.8}$$

where U_v^* is the non-dimensional velocity of the vortex ring defined as $2\pi U_{vortex} L_c/\Gamma_v$ and D^* is the non-dimensional vortex ring diameter defined as D_v/L_c, assuming the initial diameter is the same as the chord length L_c. In the above, U_v is the vortex ring velocity, Γ_v is the circulation in the vortex core and D_v is the vortex ring diameter. Now expanding D^*,

$$D^* = 1 + 16k't^* \tag{2.9}$$

where $t^* = \nu t/4L_c^2$ and $k = 14.4$, $k' = 7.8$ are the empirical constants found using experimental data[27]. We can interpret this as, when there is enough time for viscosity to act, the radius of the vortex ring increases. Saffman's[18], velocity equation for axisymmetric viscous vortex rings has also been tested at relatively high Reynolds numbers. This was done by measuring the average of axial velocity in the vortex core, assuming the circulation induced translational velocity of a steady vortex ring would be the same as the average velocity at the core [24]. Saffman's velocity equation in relation to dimensionless energy E^* can be written as[18],

$$U_{vortex}/U_{plate} = \frac{\Gamma^*}{D^*\pi}(E^*\sqrt{\pi} + \frac{3}{4}) \tag{2.10}$$

where Γ^* is the dimensionless circulation, E^* is the dimensionless energy of the vortex ring and $D^* = D_v/L_c$ is the non-dimensional vortex ring diameter. These terms will be further discussed separately in the results and discussion.Now, let's further discuss how vortex rings are formed, and they are related to the phenomenon of vortex shedding.

2.2. Vortex shedding

To describe vortex shedding, first we need to understand the basic difference in geometric types, as any object can be classified as either a bluff body or streamlined body. A bluff body is defined as an object with geometry that opposes the flow streamlines and vice versa for streamline bodies[28]. As we are interested in flow past a bluff body (flat plate oriented perpendicular to flow), let's discuss how vortex shedding would occur in such a bluff body.

Process of vortex shedding

The separation of boundary layer is the foremost reason behind vortex shedding. A *boundary layer* is a fluid layer closer to the bounding surface where no-slip at the wall imparts velocity gradient, whereas a *shear layer* is a region with velocity gradient containing both a separated region and a recirculation region after separation. When a boundary layer with $Re \gtrapprox 50$, approaches a sharp edge, the fluid parcels separate away from the body due to their high inertial forces, resulting in a shear layer emanating from the plate's edge. Consequently, the free end of the shear layer roll up into a solid body like rotational region called *vortex core*, surrounded by an irrotational region[29]. The vortex core grows over time due to more rotating fluid parcels fed by the shear layer till reaching a threshold energy. Then vortex is shed from the shear layer and this remaining shear layer repeats the aforementioned process, resulting in the phenomenon of called vortex shedding. Thus, vortex shedding is a periodic flow that emerges when a fluid flows past a body, and it is characterized by the velocity, shape, size and kinematics of both the body and flow. The region behind the bluff body that are disturbed compared to mean flow is called a *wake*.

Relevance to living world

This periodic shedding of vortices in the near wake, leads to large fluctuating pressure forces and may cause structural vibrations, acoustic noise, or resonance. We experience these phenomena in everyday life even with simplest of geometries such electric cables, pipeline suspension bridges, chimneys and structural buildings[30]. This not only has negative effects such as failure of aforementioned components but also useful in natural cases such as animal flight, swimming and atmospheric mesocyclones to maintain the ecosystem and geophysical cycles[31]. These structures are often studied using generalized fundamental geometries. One such example that we are interested in this study is flow past a flat plate. We are particularly interested in flat plate oriented perpendicular to the flow, as they provide rich information and are often used as a canonical case to understand flight and swimming in nature.

What affects vortex shedding?

Apart from kinematics and shape of the body, the vortex shedding also depends on the constitutive equations. For example, in a Newtonian fluid, only viscous and inertial forces play a vital role, whereas in a viscoelastic fluid, elastic forces are also included. First, let's discuss Newtonian vortex shedding in order to compare and understand the viscoelastic effects. Since, viscous and inertial forces dominate the flow, it can be characterized by Reynolds number Re,

$$Re = \frac{\text{Inertial stress}}{\text{Viscous stress}} = \frac{\rho u^2}{\eta u / L_c} = \frac{\rho u L_c}{\eta} \tag{2.11}$$

where L_c is the characteristic geometric length scale which is often the diameter in case of cylinders and plate width in case of flat plates. In case of Newtonian fluids, bluff bodies with separation has enormous pressure/form drag, which due to the integrated surface pressure distribution acting over the body. In attached flows, friction drag is more important, which is due to the friction between surface and fluid. In this study, our focus is limited to bluff bodies. The important regions in such a bluff body flow are the boundary layer, wake and separated shear layer[28, 32]. A typical shedding of a starting vortex can be distinguished into different phases as following[33] (see Figure. 2.4),

- Boundary layer separation
- Shear layer formation
- Vortex roll up
- Pinch-off

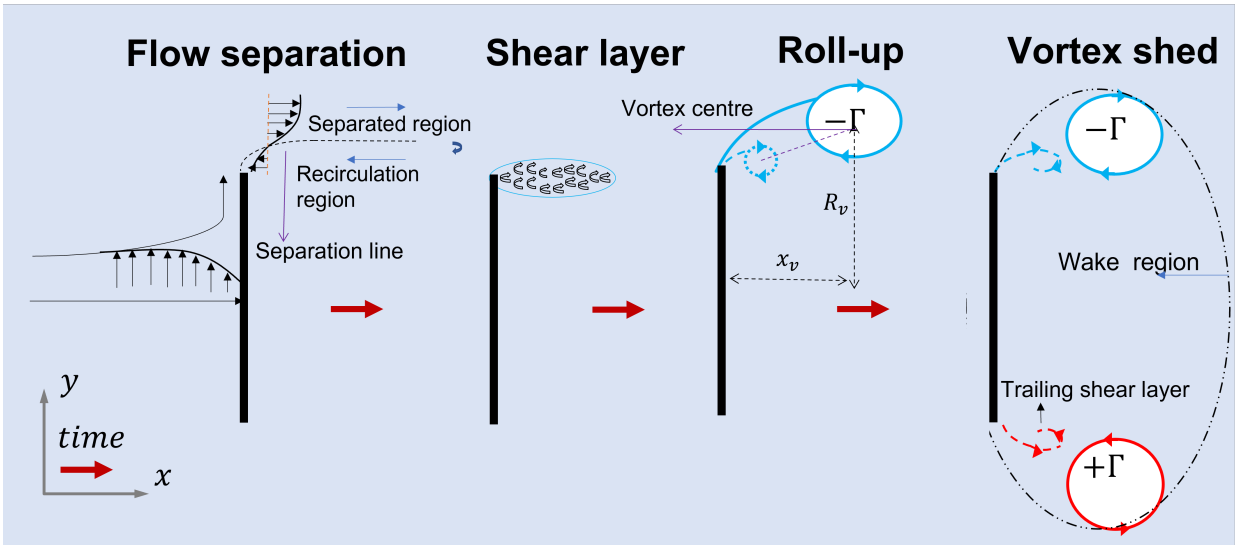

Figure 2.4: Stages of vortex formation: Boundary layer separation leading to a shear layer, shear layer roll up forming a vortex core and wake, finally vortex pinches off fro shear layer. This figure is self-made

2.2.1. Boundary layer separation

The concept of boundary layer was introduced by Prandtl in 1904[34].When a viscous fluid flows past a body, it shears and slows down in areas in proximity to the solid-fluid interface (due to no slip) forming a moving boundary layer. Within the boundary layer, the positive (adverse) pressure gradient causes a decrease in momentum in the flow direction till the flow reverses towards a favourable gradient, thus affecting fluid parcel separation from the interface. This phenomenon is called the boundary layer separation.Typically, in blunt bodies and sharp edges, the separation happens due to inability of inertial fluid parcels to follow a sudden discontinuity in geometric profile. Thus, it is easy to keep track of separation points along such sharp edges. An example of boundary layer separation is visualized in the Figure. 2.4. Although there are no analytical solutions to understand a separating boundary layer perpendicular to the flow, Hiemenz boundary layer could provide some insights on boundary layer for stagnation region in a flat plate normally oriented to flow, before separation. The boundary layer thickness of Heimenz flow, for a flat nosed body with velocity gradient of $B \approx 1.57\frac{U_\infty}{L_c}$, is given by[35],

$$\frac{\delta}{L_c} = \frac{2.41}{\sqrt{1.57Re}} = \frac{1.92}{\sqrt{Re}} \tag{2.12}$$

It is notable that the boundary layer thickness for a stagnation flow is constant as the effects of fluid acceleration due to geometric profile is balanced by the viscous diffusion[35].

2.2.2. Vortex formation

Once the boundary layer is separated, we have a separated region and recirculating region on either side of the separation line (see flow separation in Figure.2.4). This would cause concentrated regions of vorticity along the separation line, resulting in the formation of a vortex sheet in the leeward side of a body, also called shear layer. By law of vortical induction, every fluid parcel in a vortex sheet with would induce a motion on other parcels and the sheet itself (self-induction) resulting in evolution of the sheet. According to Helmholtz, these sheets are inherently unstable, as any irregularity in otherwise stationary flow should give rise to a progressive spiral unrolling. This results in a self-similar roll up with respect to the plate's velocity, where the shape remains the same but grows with time, resulting in a vortex was explained with theoretical formulations by Pullin based on Kelvin-Helmholtz instability and Kaden based on wing tip vortex.Furthermore, it has also been established that the centre moves in a oblique line with a velocity proportional to $t^{2/3}$, while rolling up[36]. An example of vortex sheet roll up is show in Figure.2.5.

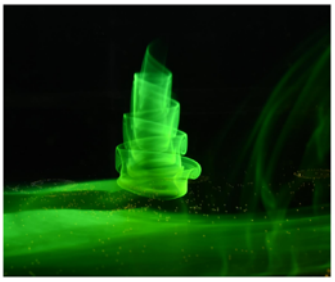

Figure 2.5: Dye visualization of vortex formation due to drain hole by rolling up of vortex sheets. This figure is taken from[39]

2.2.3. Optimal vortex formation distance

The aforementioned growth of vortex by roll up has been reported to reach its threshold at a distance of, $4L_c$ universally for propulsive vortex rings[23]. This was explained by using Kelvin-Benjamin variational principle which states that "a steady-translating axis-touching vortex ring possesses maximum energy with respect to impulse-preserving iso-vortical perturbations", in other words, energy is locally maximized such that impulse is preserved. By using this idea, it has been established that a vortex cannot accept any more vorticity when the impulse normalized energy of the vortex ring reaches higher than the piston in case of propulsive vortices, furthermore it was concluded that ring impulse is equal to total momentum flux at exit for propulsive vortex ring[37]. This principle has also been found to work on non-axisymmteric vortex rings [38].

2.2.4. Effects of flow separation

The above processes lead to cause a wake in the leeward side of the body. The pressure inside the wake region is low after separation, forming a net pressure drag on the body, and the shear stress at the wall gives rise to skin friction drag. This theoretical link between vortex street and drag was established by Von Kármán in 1912[32]. For a wake due to steady flow over a bluff body, on applying continuity and momentum surface balance for a chosen control volume, we get the drag experienced by the body as[40],

$$F_D = \int_A \rho u(U_{mean} - u)dA \tag{2.13}$$

The alternate shedding of vortices in the near wake, leads to large fluctuating pressure forces and may cause structural vibrations, acoustic noise, or resonance. This alternate shedding is characterized by Strouhal number St,

$$St = \frac{f_s L_c}{u} \tag{2.14}$$

where f_s is shedding frequency. However, the topology of wake depends on the geometry of a bluff body. The widely studied bluff body geometries are finite curvature, sharp-edged and combined shapes. In the case of curved surfaces like circular and elliptical cylinders, flow separation may oscillate and occur over a segment of the surface, whereas in sharp-edged cases such as flat plates, flow separates at a defined point[41]. For further understanding, let's discuss vortex shedding past such canonical geometries with constant velocity (steady) and uniformly accelerated flows.

2.3. Canonical cases

2.3.1. Steady cylinder

The most well studied bluff geometry in a steady velocity flow is the unconfined infinitely long cylinder. Although, we are primarily interested in a flat plate, the cylinder provides a complete overview of vortex shedding regimes owing to their extensive literature. The flow behaviours are characterized based on Re. For $Re < 5$, there is no separation of boundary layer, which is called creeping flow. Till about a $Re = 49$, the wake is steady and laminar with two symmetrically placed vortices, then at $Re = 49$ Hopf bifurcation kicks in causing laminar, periodic vortices extending till $Re = 190$ and it is called primary von-karman vortex shedding. From $Re = 190$ to 260, the 3D wake transition occurs due to primary vortex

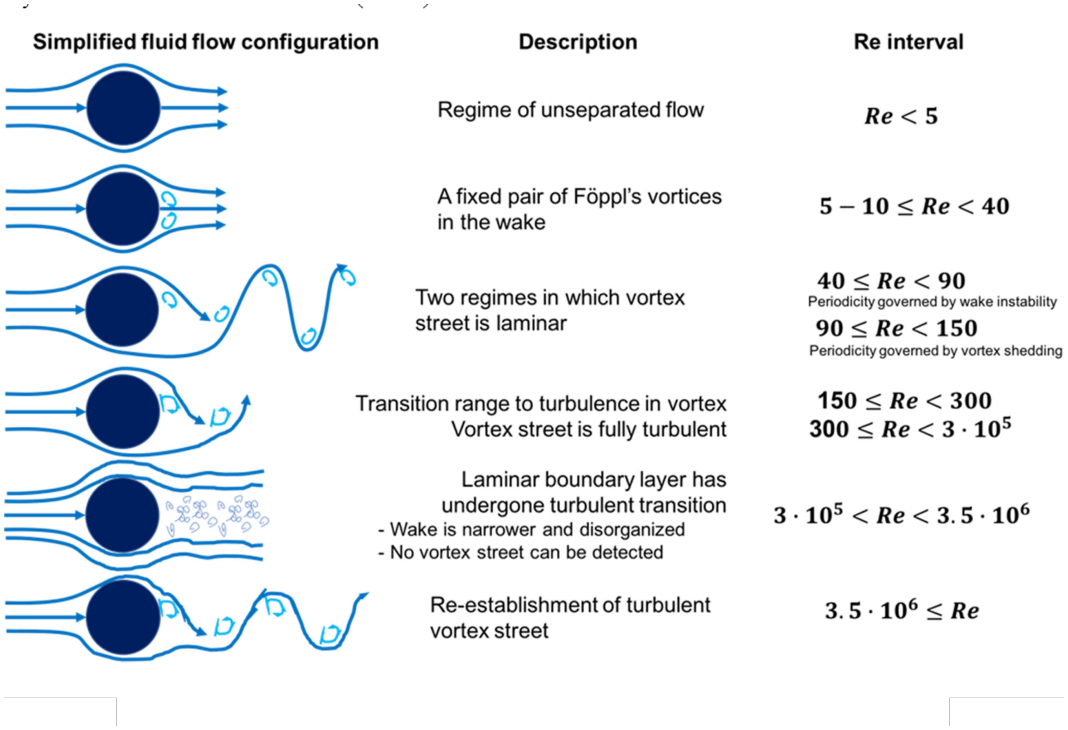

Figure 2.6: Re regimes in steady flow past a cylinder. The vortex street becomes turbulent only for $Re > 300$. This figure is taken from [43]

deformation and vortex phase dislocations. At $Re = 260$, the Reynolds stress reaches maximum and decreases till $Re = 10^3$ with periodic and fine 3D scales. So far, the drag coefficient C_D decreases with Re, whereas St increases with Re. On the contrary, from $Re = 10^3$ to 2×10^5, the C_D remains nearly to be a constant around 0.4, whereas the St is maintained around 0.2. In this region, Kelvin-Helmholtz instability occurs at the separated shear layer, transforming the shear layer turbulent.The drag crisis happens around $Re = 10^5$ to 10^6. This is due to the mixing of boundary layer with unseparated region aided by shear layer instabilities causing flow reattachment. It again separates, and eventually the boundary layer turns turbulent at extremely high Re [32, 42]. These discussed phenomena that occur at various Re are illustrated in Figure.2.6. In this study, vortex shedding regime at $Re < 300$ is focussed to avoid the complexity of turbulence, and they are further discussed for a flat plate in the below section.

2.3.2. Steady flat plate

Another important geometry is the thin flat plate as it is considered as the extreme bluff body with sharp edges and constant flow separation. It is generally used as a standard geometry for insect/bird hovering and Micro air vehicles. Although, it was studied first by Prandtl in 1904, the literature is not as extensive as cylinder. The flat plate with different inclinations has been studied in the past, however the flow normal to the plate is very rich in information. It has fixed separation points with twin vortices and the separated near-wake is known to remain symmetrical and steady in the Reynolds number range $Re = 5 - 20$. The near wake undergoes hopf bifurcation around $Re = 30 - 35$, resulting in onset of unsteady vortex shedding, then the quasi periodic mode destabilizes the wake at $Re = 105 - 110$, the dominant mode destabilizes at $Re = 125$ resulting in 3D wake transition at $Re = 200$[44–46]. On comparison with cylinder, the instabilities seem to occur even at slightly lesser inertial stresses.

2.3.3. Impulsively started cylinder

As we discussed earlier, the vortex dynamics and flow topology depend on a multitude of factors, kinematics being an important one. Various kinematics have been studied in the past, such as oscillation, constant rate of rotation and translation, accelerating rotation and translation. In this study, we limit

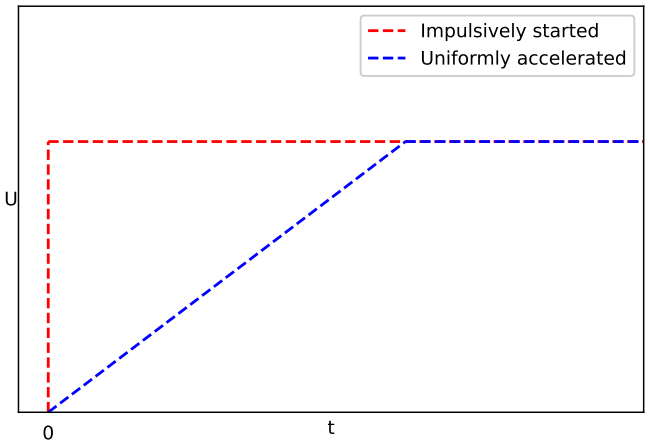

Figure 2.7: Unsteady translational velocity as a function of time in Impulsively started vs uniform accelerated. This figure is self-made

ourselves to translation motions of impulsively started and uniformly accelerated cases, as shown in Figure.2.7. The flow development around an impulsively started cylinder has been studied as one of the classic problems in both numerical and experimental studies. Typically, impulsively ($a = \infty$) started circular cylinder can be usually categorized into two phases. In the initial transient phase, the boundary layer grows as the square root of time, whereas in the second phase the vortices form. Many numerical studies have been done compared to experimental work[47, 48]. One of the earliest experimental work on impulsively started cylinder was done by Honji and Taneda in 1969 [49]. In the beginning, the flow is irrotational, and the boundary layer slows grows in thickness, causing flow separation followed by symmetrical twin vortices. Two non-dimensional numbers are used to characterize this flow, which Re and dimensionless viscous diffusion timescale t_v, which is defined as

$$t_v = \frac{\nu t}{L_c^2}$$

The length between cylinder and core centre for the twin vortices in an impulsively started cylinder has been reported to be scaled as,

$$\frac{x_v}{L_c} = k\frac{s}{L_c} \tag{2.15}$$

where x_v is the distance from rear to the vortex (see Figure.2.4 for x_v in plate) and s is the displacement of the body. This is found to be applicable till $Re < 550$, where k are constant values that change with different regimes of Re. At $Re = 550$, the secondary vortices are found to appear on the surface of the cylinder, but not earlier. In another study of an impulsively started cylinder, a classic closed wake occurs for $Re > 4.4$ and the recirculation zone grows in length and width. In the meanwhile, the separation point moves upstream with time and the wake length decreases continuously with increasing Re. This classic low Re regime is marked in the range $4.4 < Re < 60$. The intermediate secondary vortices are found to occur at $Re > 60$, unlike the earlier study. It is also noted that a bulge in streamline happens around $Re > 60$ with a pair of secondary vortices, furthermore the wake evolves in $Re = 60{-}500$ marking the intermediate range. The presence of streamline bulge and secondary eddies causes a kink in the exterior boundary of recirculation zone and secondary vortices isolate at $Re = 500$ [50].

2.3.4. Uniformly accelerated cylinder

The early study by Honji and Tandea [49] also included a case with accelerating cylinder characterized by Dimensionless viscous diffusion timescale t_v and dimensionless acceleration α, which is defined as

$$\alpha = \frac{aL_c^3}{\nu^2} = \frac{Re(t)}{t_v} = \frac{Re^2(t)}{2T^*} \tag{2.16}$$

where $Re(t)$ is the instantaneous Re defined using $u = at$. In this case, the distance between plate to vortex centre x_v is found to be scaled as

$$\frac{x_v}{L_c} = kt_v^2\alpha = k\frac{at^2}{L_c} = k\frac{s}{L_c} \tag{2.17}$$

The significance of these non-dimensional numbers can be realized using vorticity equation (Equation 2.1). The diffusion timescale t_v represents the viscous diffusion term in the right-hand side of the vorticity equation, Re or α represents the rate of change of vorticity on the left-hand side of the equation. It can be noted that both impulsively started and uniformly accelerated cases scale with s/L_c but with different constants of k. Therefore, $T^* = s/L_c$ can be defined as the non-dimensional time. When we try to generate impulsive or uniformly accelerated flows at high Re, it may be hampered by the formation of compression waves or cavitation bubbles in liquids. To account for these effects, an extra parameter of acceleration is used which includes initial flow history, defining it as

$$\alpha' = L_c a u_t^2 \tag{2.18}$$

where u_t is the terminal velocity after acceleration[51].

Characteristic formation time
As we have discussed earlier, when the circulation or energy of the vortex ring has reached a certain level, it ends up in the first shed vortex and this time is defined as characteristic vortex formation time. It is defined using the concept of optimal vortex formation time, based on instantaneous circulation Γ, strength of shear layer $(u - u_\infty)$ and characteristic length scale L_c of the shear layer

$$T_f = \frac{C\Gamma}{(u - u_\infty)L_c}$$

where C is the constant defined by the physical configuration of the flow. This was initially studied for vortex ring formation using piston-cylinder apparatus, for which C is 2 and $\Gamma = \frac{u^2 t}{2}$. Based on this, T_f is redefined as the T^* at which the formation is complete.Interestingly, for both a vortex ring and a starting cylinder, the pinch off time has been universally found to be $T_f = 4$. It has been suggested that it is reasonable to consider that optimal vortex formation may be a general feature in flows with coherent, three-dimensional vortex shedding[23].In case of a starting cylinder with low acceleration the wake remains symmetric till $T_f = 4$ and then it sheds, while for acceleration above a critical value, the initial symmetry breaks. The circulation Γ of the first shed vortex is found to be equal to the circulation at $T_f = 4$[33].

2.3.5. Impulsively started and uniformly accelerated flat plate

In this study, we are interested in the flow behaviour around a flat plate oriented normal to its accelerating direction. As stated earlier, this canonical flow is a simplification of the accelerating cylinder case as the boundary layer separation points are fixed, but it has been less extensively studied than the cylinder case. A flat plate accelerating to its normal direction was studied in 1970 by Taneda and Honji[52]. It was studied with both an impulsive and accelerating case, similar to cylinder. In either case, the initial motion is irrotational, then the separation occurs at the edges, and at small times the symmetrical twin vortices appear, they grow longer and longer with time. Finally, they become asymmetrical and the von Kármán street forms. For an impulsive case, the distance from plate to centre of twin vortices x_v (see Figure.2.4) scale as[52],

$$\frac{x_v}{L_c} = 0.89(Re\, t_v)^{2/3} = 0.89(T^*)^{2/3}, \qquad t_v < 0.1 \tag{2.19}$$

whereas for acceleration case, it is scaled as

$$\frac{x_v}{L_c} = 0.48(\frac{at^2}{L_c})^{2/3} \qquad t_v < 0.1 \tag{2.20}$$

An interesting point to note here is that this power of $2/3$ is the same as in vortex roll up studies we discussed earlier in section 2.2.2. In impulsive cases, once the two counter rotating vortices emanate from

the plate tip, they induce secondary vorticity behind the plate at early stages as shown in Figure2.8a. In this figure, the thin vortex at the plate tip is called primary vortex and the larger rolled vortex to the right of the plate is secondary vortex. The strength of this secondary vorticity increases for higher Re. Here diffusion increases the width of the shear layer, by weakening the secondary vortices, and ends up in a stable configuration. On the other hand, for accelerating cases, the primary vortex becomes stronger with a and forms closer to the tip of the plate. In accelerating cases at sufficiently high Re, the primary, secondary vortices interact causing Kelvin-Helmholtz instability due to variable shear as shown in Figure2.8. In both cases, a secondary vortex is formed by a strong primary vortex that interacts with the plate. [53]. For a finite plate accelerating normal to itself, the flow regimes can be classified into three

(a) Impulsively started case **(b)** Accelerating case

Figure 2.8: Vortices in unsteady flat plate: In accelerating case, Kelvin-Helmholtz instability can be found due to interaction of primary (near plate tip) and secondary vortices (behind the plate), unlike in an impulsively started flat plate. These figures are taken from[53]

different stages[54].

- The Rayleigh layer regime is the initial flow consisting of of uniform viscous boundary layer surrounding the plate and tip without any separation.
- The second regime is the self-similar growth of the vortex core till the plate moves to $T^* = 0.5 - 1$. The circulation grows and reaches maximum when the vortex detaches the plate
- Finally at the third regime, plate shape effects are found.

In an accelerating plate, at $1000 > Re > 20$, the effect of wall proximity has been reported to be significant compared to lower Re cases [44]. A study on accelerating starting vortex of normal flat plate has been reported using hydrogen bubbles[55] and they have reported that the growth rate of core diameter d_{core} and the translational speed of the vortex core U_{vortex} are constant for a range of accelerations at low Re. A peculiar aspect of the aforementioned study is the definition of non-dimensional acceleration as $Re_a = \sqrt{\alpha}$, a more compact way to represent α in terms of numerical values.

2.3.6. Effect of Aspect ratio

During experiments, a few parameters influence the flow behavior such as aspect ratio AR and end effects. The aspect ratio, AR can be defined as

$$AR = \frac{\text{Depth of geometry}}{\text{Diameter (or Width) of geometry}}$$

In this study we will focus on the mid-plane of the geometry with constant finite aspect ratio and so it is important to understand their influence. In general, 3D finite aspect ratio effects can be minimized using the geometry extending along fluid-air interface whereas lower end is placed in proximity to bottom surface. Although slight 3D effects maybe seen in such settings, they don't seem to vary with $AR > 10$ [56]. The critical Re for different regimes tend to delay for smaller aspect ratios, likewise $AR > 50$ is found to be required for $Re < 230$ to get results corresponding to a standard quasi-infinite cylinder. For different regimes, different minimum aspect ratios are found, ranging from 25 to 100 [57]. However, in terms of practical interest such as animal flight[58], rowing blade[2], have low aspect ratio of 2.75-6. The unsteady forces at high angle of attack are due to leading trailing edge vortex (TEV), tip vortex. The major lift forces are due to suction from the leading edge vortex(LEV), whereas free end causes a tip vortex (TV).Interaction of tip and leading-edge vortices generates a high transient drag of a local maximum in C_D vs Re graph[58].It has been found that the aspect ratios highly influence the pinch off, forces and vortex evolution. Vortex evolution has been shown to be strongly dependent on not only the total size of the shear-layer-feeding perimeter, which supplies vorticity to the separated wake, but also on the geometric area available for vortex growth, as defined by the hydraulic diameter. Pinch-off

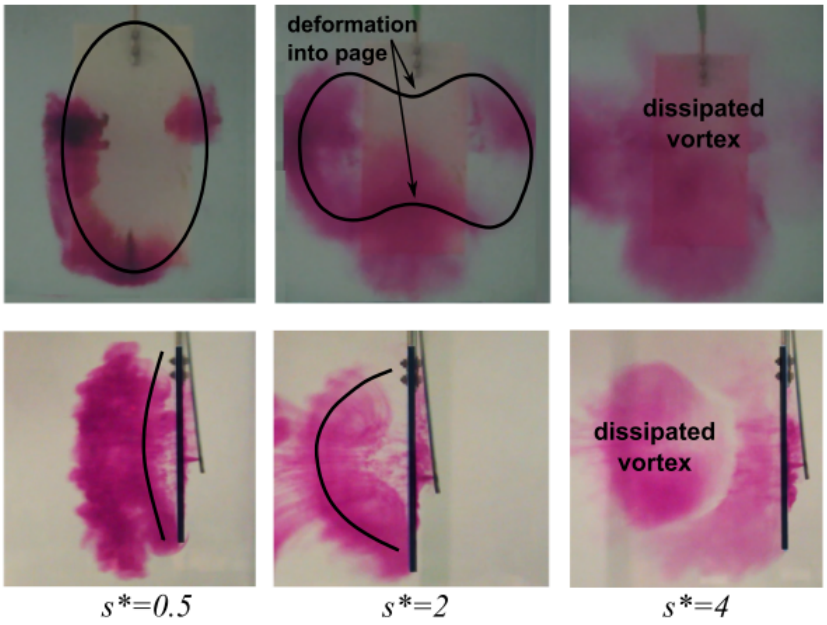

Figure 2.9: Dye-visualized vortex ring behind a flat plate with $AR = 2$ shows a 3D deformation switching their major and minor axis at $T^* = 2.5$ due to different induced velocities at varying curvatures.This figure is taken from[25] and, s^* here is $0.8T^*$

is expected to occur when a pressure maximum forms behind the vortex. In squares/rectangles, the formed vortex ring has slightly higher radius ($0.6L_c$) than in smooth cases ($0.5L_c$). It has also been shown that for rectangular plates with $AR = 2$, an elliptical vortex ring is formed and goes through axis-switching (periodical change of major axis to minor axis and vice versa) for $Re \approx 10^4$. This is because of different induced velocities along the filaments due to rectangular/elliptical nature, despite having the same circulation as visualized in Figure.2.9 [25].

2.4. Forces

The flow separation and vortex ring formation discussed so far cause a wake region beside the plate and circulation along the edges. A wake with velocity defect and circulation induce forces on the object. The forces acting on the plate can be decomposed into steady and unsteady forces corresponding to the effects of fluid velocity and acceleration, respectively.

2.4.1. Steady forces

An immersed bluff body is likely to experience forces and moments due to the external flow. The forces acting on a body can be decomposed into drag force F_D, that is aligned to the body's principal axis and lift force F_L, that is aligned perpendicular (y-direction) to the principal axis and side force on the other direction. The drag and lift forces are often denoted by non-dimensional coefficients defined as,

$$C_D = \frac{F_D/A}{\frac{1}{2}\rho U_{mean}^2} \tag{2.21}$$

$$C_L = \frac{F_L/A}{\frac{1}{2}\rho U_{mean}^2} \tag{2.22}$$

where U_{mean} is the free stream mean velocity and A is the reference area. The reference area is often frontal projected area for bluff bodies, top view area for wings and hydrofoils and wetted area in case of surface ships etc.[59]. The C_L of a body is mainly characterized by circulation produced [40]. However, C_D is of primary interest in bluff bodies, and it is mainly due to pressure drag as a result of wake. Any wake with velocity defect ($U_{mean} - u$>0) due to fluid flow past an object is likely to cause drag force on the object, as described by equation.2.13. It is important to note that, although self-propelled bodies have wake behind them, the net integral of velocity defect would be zero as it would have both regions of $U_{mean} - u$>0 and $U_{mean} - u$<0[40].

2.4.2. Added mass

An interesting aspect of unsteady flows, is the increase in force required to accelerate a body at a (apart from body's own mass contribution), compared with the force required to translate the body at a constant velocity. This additional force is represented by the concept of added mass or virtual mass. It can also be seen as the additional work (acts as force on body) done to impart kinetic energy (E) needed to cause fluid motion. The rate of change of kinetic energy $\frac{dE}{dt}$ required to accelerate the fluid is given by $-FU$, whereas kinetic energy can be written as

$$E = \frac{U^2}{2} \underbrace{\rho \iiint \frac{u_i^2}{U^2} dV}_{m^a} \tag{2.23}$$

Now assuming that the parameter m^a is independent of time, the inviscid unsteady force acting on an object is defined by[40],

$$F_{us} = \frac{1}{U}\frac{dE}{dt} = m^a a \tag{2.24}$$

where m^a is the added mass, U is the object's velocity, u_i is the fluid velocity component in each direction and a is acceleration.***However, the aforementioned assumption of time independent added mass that works with potential flows may not be applicable for vortex shedding flows[40]***. In potential flow theory, the added mass of a cylinder can be interpreted as the mass of displaced fluid, however it has been argued this correlation cannot always be extended. For example, in a thin flat plate with no displaced fluid, the ideal added mass is equal to the volume of a cylinder (called as drift volume of plate) with plate width as diameter[60],

$$m^a_{plate} = \frac{\pi}{4} L_c^2 H \tag{2.25}$$

where H is the height of the plate. It has been reported that, other than **ground/surface effects, viscosity in the form of boundary layer separation and vortex shedding** also might cause changes in the added mass. A few experiments with oscillating bodies were found to be supporting this argument, as values of added mass changed with acceleration[60]. For flat plate, there was no systematic effect was found with Re on these changes. Although such viscous effects are noted, it was concluded to be contradictory among the studies[60].

2.4.3. Modelling unsteady forces

In general, the drag force increases with time on acceleration, and after it reaches steady velocity, it reduces to steady state drag. At high Re,the total drag force can be decomposed into,

$$F_x(t) = F_s(t) + F_{us} = \frac{1}{2}\rho u(t)^2 C_D A + (m^a + m_p)a \tag{2.26}$$

where F_s is steady drag, F_{us} is the unsteady drag which can further be split into plate m_p and hydrodynamic added mass m^a contributions. For a rectangular normally oriented flat plate with an arbitrary aspect ratio, the hydrodynamic mass is given by an earlier study[61]

$$m^a_{(Yu)} = \rho\Bigg[0.788\frac{l_a^2 l_b^2}{(l_a^2 + l_b^2)^{1/2}} + 0.0619 l_a l_b l_c^{1/2}\Bigg[\tag{2.27}$$

where l_a, l_b are the dimensions of the flat plate with $l_a > l_b$ and l_c being the thickness of the plate.

Additional force due to entrainment rate

However, a recent study [2] indicated that there is a residual force that has not been taken into account for hydrodynamic mass and found it to be,

$$\frac{dm_h}{dt} a(t)(t - t_{sr})$$

where t_{sr} is the offset accounting for step response and $\frac{dm_h}{dt}$ is the rate of entrainment of fluid in plate wake. Now rewriting the unsteady total drag equation,

$$F_x(t) = F_s(t) + F_{us}(t) = \frac{1}{2}\rho u^2(t) C_D A + (m_p + m_h^{(Yu)})a(t) + \frac{dm_h}{dt} a(t)(t - t_{sr}) \tag{2.28}$$

Vorticity based modelling

Alternatively, the concept of added mass can be represented using vorticity. In potential flow theory, where the flow is inviscid, the vortices are infinitely thin attached to the surface. However, in a real fluid, the flow separates and forms a vortex. Based on this difference, the plate is represented by a vortex sheet due to u_1 and u_2 corresponding to the surface slip velocities on both sides of the plate. The boundary layer vorticity is represented by a vortex sheet of strength $\boldsymbol{\gamma_b}$, which is the circulation per unit length $\frac{d\Gamma}{dx} = u_2 - u_1$.

$$\boldsymbol{\gamma_b} = \boldsymbol{\gamma_{nc}} + \boldsymbol{\gamma_c} \tag{2.29}$$

here $\boldsymbol{\gamma_{nc}}$ is the added mass or non-circulatory component, $\boldsymbol{\gamma_c}$ is the circulatory. The circulatory component can be calculated from vorticity in the bulk flow field and can be subtracted from the experimental boundary layer component. PIV-acquired and potential theory-derived added-mass attributed vorticity are found to be in agreement, as they depend only on kinematics and geometry[62]. As viscous effects result in the transport of vorticity into the wake, it is included in the circulatory component[62]. Although a vertical flat plate is not inclined, the vortices behave similar to LEV (Leading Edge Vortex) and TEV (Trailing Edge Vortex). So the total force acting on the body can be separated into circulatory (corresponding to growth and advection of a LEV and TEV pair) and non-circulatory (corresponding to added mass) similar to the earlier study.

Lamb's vortex pair modelling

Another lower order model has been proposed in [22] where the flow was treated two-dimensional. It deconstructs total drag force into added mass and Lamb's circulatory force of a vortex pair. In this model, circular force has been represented by two counter rotating vortices separated by a distance d_v and a non-circulatory force from added mass. It has been proposed that added mass is a mechanism of vorticity production and also circulatory force coefficient is proportional to circulation growth $\dot{\Gamma}$[22]. Using Lamb's momentum of a vortex pair, the total force based on the lower order model is[22],

$$F = F_c + F_{nc} = \rho(\dot{\Gamma} d_v + \Gamma \dot{d_v}) + \frac{\rho \pi L_c^2}{4} H \tag{2.30}$$

where d_v is the distance between two vortices and $\dot{d_v}$ is the relative rate of advection.

Energized mass

In a recent study, a new approach based on Lagrange equations called energized mass was proposed, which is the total kinetic energy scaled with object velocity [63]. The added mass definition in equation 2.23 is reportedly called as energized mass m_e and applying to total force $F = \frac{D}{Dt} m_e u$ with time dependent m_e,

$$F = m_e \dot{u} + \dot{m}_e u \tag{2.31}$$

This is concluded to be in agreement with the measured force results[63, 64]. Furthermore, this approach reinforces the findings of other study about the influence of time dependent mass (entrainment) at high Re.

2.4.4. Effect of forming vortex in added mass

Added mass of vortex ring

An interesting effect of accelerating vortex rings is that have their own added mass, similar to an equivalent solid body [65]. In potential flow around solid bodies, the added mass of an object is calculated by the product of fluid mass corresponding to the object's volume and an added mass coefficient, C_i defining the factor of fluid volume accelerated (drifted) with respect to their own volume. The added mass coefficient C_i can be written as a matrix of components corresponding to each direction. In this study we limit to the stream wise direction added mass coefficient C_x as we are interested in the drag forces. For example, $C_x = 1/2$ for potential flow past sphere[60]. The standard way of calculating added mass coefficient based on the geometry is given by the ratio of drift volume (due to Lagrangian displacement of fluid parcels around, see Figure.2.10) V_D to geometric volume V_B,

$$C_x = \frac{V_D}{V_B} = \frac{m^a}{\rho V_B} \tag{2.32}$$

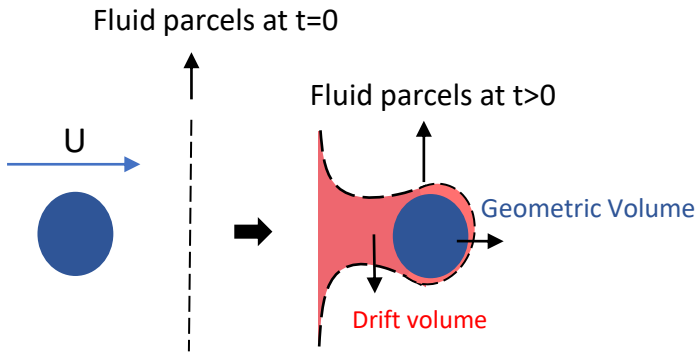

Figure 2.10: Drift volume, V_D due to Lagrangian displacement of fluid parcels with respect to their initial position caused by moving geometric volume V_B. Self-made figure, but inspired from experimental results of [65]

However, for a growing vortex, the surrounding fluid is entrained (converted from irrotational to rotational) and so this effect was taken into account using

$$C_x = \frac{V_D(t) - V_E(t)}{V_{B_0} + V_E(t)} \tag{2.33}$$

as entrained volume V_E is the change from initial volume, $V_B(t) - V_{B_0}$, with V_{B_0} as the initial volume of the body. Based on this idea, C_x has been estimated for a propulsive vortex ring with $Re = 1400$, $R_v/R_c = 1.37$ to be 0.72 (applicable even for a growing vortex as both V_D & V_B are function of time) [65]. Interestingly, this was found to be precisely equivalent to potential flow added mass coefficient of an equivalent boundary geometry (ellipsoid in this case) [65]. It has to be noted that this study uses a constant entrainment rate for a formed vortex ring. As an extension of the aforementioned study, it has been proposed that the total locomotive force acting on a self propelling animal with a vortex ring volume V_{vortex} can be written as[66],

$$F_{total} = \rho \frac{d}{dt}[V_{vortex} u_{vortex}(1 + C_x)] \tag{2.34}$$

Vortex boundary estimated using Finite Time Lyapunov Exponents [66] or stream function [65] is used to extract the geometry of vortex rings and their corresponding added mass based forces. Another study using Elliptic LCS (discussed later) quantified that the added mass coefficient of a propulsive circular vortex ring is higher early in formation and reaches a steady value when formed [67] (same value as reported in [65]). This could be thought of as large entrainment of irrotational region to a core at the beginning, however for subsequent vortices the shear layer is already present to roll up.

Entrainment ratio

The method of circulatory and non-circulatory force decomposition assumes that the forces are superposable and follows a perfect self-similarity. However, it has been reported that the vortex involved acceleration is inherently non-self similar and cannot be superposed[64]. Using the above arguments and entrainment contribution, the idea of energized mass that we discussed before was developed, agreeing well with the experimental force measurements[64]. Another study looked at the entrainment ratio of a turbulent starting circular plate using 4D PTV, enstrophy and FTLE (discussed later). They found that entrainment ratio (Entrained mass to enstrophy based mass) was increasing with time in turbulent cases compared to laminar cases (almost constant). The compilation of entrainment ratio is shown in Figure 2.11[68]. If we use this conclusion over the definition of added mass coefficient (Equation 2.33), we can safely assume that the added mass coefficient is constant with time for laminar vortex rings. Although the entrainment ratio does not change in time, it has been reported that added mass increases with increase in acceleration for laminar vortex rings where vortices roll-up to form a vortex ring[69].

Study	L/D	Re (10^2)	η	s/D	Line
Dabiri and Gharib (2004)	4.0	40	0.28 ~ 0.32	4 ~ 15	
Shadden et al (2007)	4.0	40	0.15 ~ 0.20	1 ~ 6	
Dabiri and Gharib (2004)	2.0	20	0.32 ~ 0.40	4 ~ 15	
Shadden et al (2007)	2.0	20	0.20 ~ 0.30	1 ~ 6	
Olcay and Krueger (2008)	2.0	20	0.24	~ 2.5	N/A
Shadden et al (2007)	1.0	10	0.30 ~ 0.50	1 ~ 6	
Olcay and Krueger (2008)	1.0	10	0.33	~ 2.5	N/A
Shadden et al (2007)	0.5	5	0.45 ~ 0.65	1 ~ 6	
Olcay and Krueger (2008)	0.5	5	0.43	~ 2.5	N/A
Rival et al(2018)*	N/A	90 ~ 430	0.36 ~ 0.50	0.1 ~ 0.3	

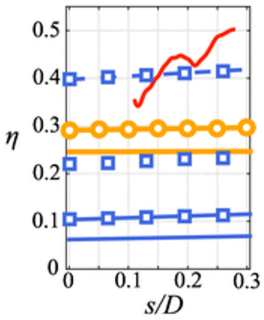

Figure 2.11: Entrainment ratio η for a circular vortex ring taken from * [68]. Here, L/D is stroke length, and s/D is T^*. For $Re \leq 40 \times 10^2$, η is constant unlike highly turbulent cases of $Re > 90 \times 10^2$, so we can assume constant C_x for laminar regime

2.5. Non-Newtonian fluids

So far, we discussed the vortex dynamics in a simple Newtonian fluid, that follows Newton's law of viscosity. By Newton's law of viscosity, the strain rate experienced by the fluid is proportional to the applied shear stress and this proportionality constant is defined as viscosity. However, Non-Newtonian fluids that do not obey this law are also found in biological and industrial systems, ranging from blood to paint. They can be classified depending on change in their viscosity for an applied stress as time dependent and shear dependent fluids. The **time dependent** Non-Newtonian fluids can be further classified into Rheopectic and Thixotropic. In Rheopectic fluids, the viscosity increases as a function of applied stress duration, whereas viscosity decreases with applied stress duration in Thixotropic fluids. A few examples of Thixotropic fluid are yogurt, peanut butter, xanthan gum; Rheopectic fluids include printer ink, synovial fluid, etc. Similarly, the **shear dependent** effects can be classified based on the existence of a yield stress, which is a minimum stress required for the fluid to start flowing. If yield stress exists, as in toothpaste, mayonnaise and chocolate, then the fluid is called Bingham plastic. On the other hand, if a shear dependent Non-Newtonian fluid starts immediately flowing, then it can be classified further into shear thinning (pseudoplastic) and shear thickening fluid (dilatant). A few examples of shear thinning fluids are paint, polymer solutions and blood, whereas shear thickening fluids include quick sand and thick starch solutions [70, 71]. The time dependent and shear dependent characteristics of the above discussed fluids are illustrated in Figures 2.12a and 2.12b respectively. Apart from viscosity based differences, some Non-Newtonian fluids possess elasticity like a solid along with viscous effect and these are called **viscoelastic** fluids. They are characterized by their ability to store energy temporarily as elastic stresses, eventually losing it due to viscous action. In other words, they exhibit a decaying elastic memory.

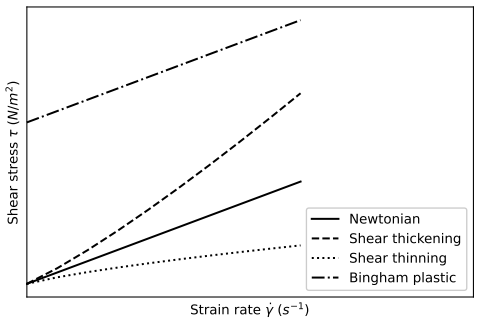

(a) Time independent Non-Newtonian fluids : Newtonian fluid has a constant viscosity, Shear thinning fluid has viscosity decreasing with strain rate, shear thickening fluid has increasing viscosity with strain rate and Bingham plastic has to reach yield stress before it flows

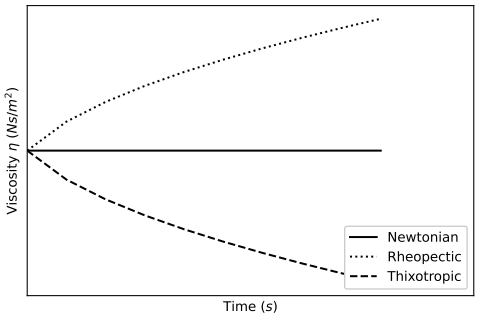

(b) Time dependent Non-Newtonian fluids: Rheopectic fluids have increasing viscosity with applied stress duration, Thixotropic fluids have decreasing viscosity with applied stress duration

Figure 2.12: Classification of fluids based on viscosity: The proportionality constant (slope) between applied shear stress and shear strain is called viscosity. These figures are self-made

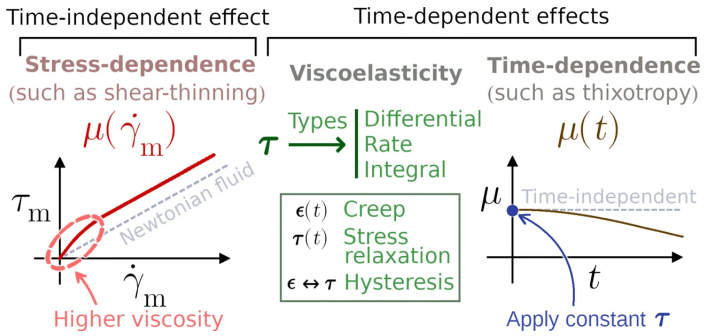

Figure 2.13: A naturally occurring Non-Newtonian fluid can have a combination of viscoelastic effects, stress dependent and time dependent viscosity, but not often viscoelastic with constant viscosity. This figure is taken from [81]

2.5.1. Viscoelasticity

Non-Newtonian fluids depend on both time and stress, along with viscoelastic effects. An example of Non-Newtonian fluid is represented in Figure 2.13, where the fluid exhibits *stress dependent* shear thinning and *time dependent* thixotropy along with *viscoelastic* effects. Such Non-Newtonian viscoelastic fluids can be seen all around us, both naturally occurring and man made. They are often found in different forms such as paints, ciliary motion of mucus, toothpaste, wheat flour dough, cheese, etc [72–75]. However, in this study the focus is solely on viscoelastic effects independent of other Non-Newtonian effects. To realize this, a constant viscosity viscoelastic fluid will be used, and they will be further discussed in section.2.9. The viscoelasticity is usually characterized by creep, stress relaxation and hysteresis. A typical Newtonian viscous material continue to deform when a stress is applied. On the other hand, purely elastic materials store energy once a stress is applied. When applied stress is removed in an elastic material, they return to the equilibrium position by using stored energy. Both of these properties can be found in the viscoelastic fluids, where viscosity is associated with loss of energy due to diffusion and elasticity is associated with storage of energy due to bond stretching. Thus, viscoelastic materials do not store 100% of the energy, but dissipate some of its energy, and it is called hysteresis. Another interesting characteristic called stress relaxation occurs when the stress reaches a peak and decreases over time, after a constant strain is applied over the fluid. Similarly, when a constant step stress is applied to the fluid, it's strain increases with time. This phenomenon is called creep [75–78].Furthermore, these fluids are usually accompanied by shear thinning (or thickening of viscosity), extensional thickening of viscosity and normal stresses in strain[74]. Because of these normal stresses, peculiar effects are observed such as rod climbing/ Weissenberg effect, die swell during extrusion, vortex enhancement (due to high extensional viscosity[79]) and elastic instabilities[80]. Thus, the normal elastic stress due to viscoelasticity can have unique effects over the flow field, and consequently they obey unique constitutive models. Hence, standard constitutive equations of Newtonian fluids will be discussed followed by viscoleastic models in the following section.

2.6. Constitutive equations

The basic constitutive equation for any fluid flow begins with mass conservation, which is given by the continuity equation.

$$\frac{\partial \rho}{\partial t} + \underline{\nabla} \cdot (\rho \underline{u}) = 0 \tag{2.35}$$

where t is the time,ρ is the fluid density and $\underline{u}$ is the velocity vector.For an incompressible fluid, this equation reduces to $\underline{\nabla} \cdot \underline{u} = 0$, whereas the momentum conservation is given by Navier-stokes equation,

$$\rho \frac{\partial \underline{u}}{\partial t} + \rho \underline{u} \cdot \underline{\nabla} \underline{u} = \underline{\nabla} \cdot \underline{\underline{\sigma}} + \rho \underline{g} \tag{2.36}$$

which includes local acceleration, convection of momentum, total stress tensor ($\underline{\underline{\sigma}}$) and body force respectively. Now the total stress can be written as the summation of isotropic and deviatoric stress tensors, in which p is the pressure.

$$\underline{\underline{\sigma}} = -p\underline{\underline{I}} + \underline{\underline{\tau}} \tag{2.37}$$

For a Newtonian fluid, the shear stress $\underline{\underline{\tau}}$ is given by,

$$\underline{\underline{\tau}} = \eta\underline{\underline{\dot{\gamma}}}, \qquad \underline{\underline{\dot{\gamma}}} = \underline{\nabla u} + (\underline{\nabla u})^T \tag{2.38}$$

where viscosity η is constant. However, when it comes to viscoelastic fluids, the Newtonian shear stress relation does not work and so specific constitutive models are required.

2.7. Viscoelastic models

Various models are available to describe viscoelasticity, and the effective viscoelasticity of a fluid that simultaneously loses and stores energy, can be characterized by a timescale called relaxation time λ. Viscoelasticity is often due to the presence of polymers in a base solution, and they have a spectrum of multiple relaxation time periods characterizing relaxation to an equilibrium state when a stress is applied. However, it is customary to approximate them with the dominant or largest relaxation time for simpler representation. Furthermore, a fluid flow can be classified based on the applied stress into shear flow and extensional flow, having their own relaxation timescales and viscosities. In order to account for both viscous and elastic effects, continuum models based on dashpots and springs are used, accounting viscous and elastic effects respectively. The most prevalently used models are Maxwell, Oldroyd-B, Giesekus, FENE-P models and higher order non-linear models with multiple relaxation times as viscoelasticity is characterized by a spectrum of relaxation times. When it comes to extensional viscosity, a single relaxation model like Maxwell fails with large errors. Oldryod-B is the simplest of these to use, however the validity is limited to an extensional strain rate of, $\dot{\epsilon} \leq (2\lambda)^{-1}$ as predicted stresses may grow unbound at larger strain rates. Although limited, it is argued that such high rates are rarely reached in industrial flows[82–87]. A single-mode Oldroyd-B model is found to be inadequate in accurately predicting transient flows of Boger fluids (constant viscosity viscoelastic fluids) at low Deborah number De (discussed later) and low Reynolds number Re for a falling sphere in Boger fluid. Though it has marginal error at higher De, the qualitative behavior is relatable[88]. When it comes to Boger fluid flow through contractions, the Oldroyd B model has failed to predict the significant increases observed experimentally in the pressure drop[89]. Although, Oldroyd-B is not the most accurate model for predictions, most of the numerical studies even involving turbulence have been done due to its simplicity and marginally low error in most cases[90]. Hence, Oldryod-B model will be used to characterize the fluid in this study. Let's first discuss Maxwell model as it is the simplest fundamental model on which other models are built upon and then Oldryod-B model shall be discussed.

2.7.1. Maxwell model

In the Maxwell model, a spring and a dashpot are added in series, experiencing the same stress σ as in Figure 2.14. This stress σ will be represented as τ, E is the elastic modulus of the spring and γ is the strain in the following,

$$\gamma_1 = \frac{\tau}{E}, \quad \dot{\gamma_2} = \frac{\tau}{\eta} \quad , \gamma = \gamma_1 + \gamma_2 \tag{2.39}$$

differentiating the strain equation with respect to time and and replacing η/E with a characteristic relaxation timescale λ, we get

$$\tau + \lambda\dot{\tau} = \eta\dot{\gamma} \tag{2.40}$$

This λ based on Maxwell model is represented by λ_m. The Maxwell model predicts creep, but not the decreasing strain-rate. There is no anelastic recovery, but there is the elastic response and a permanent strain.

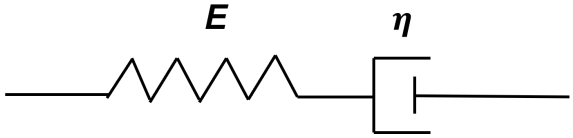

Figure 2.14: Maxwell model—a dashpot with viscosity η and a spring with elastic modulus E in series experiencing a stress τ on both ends. This Figure is self-made, but inspired from[91]

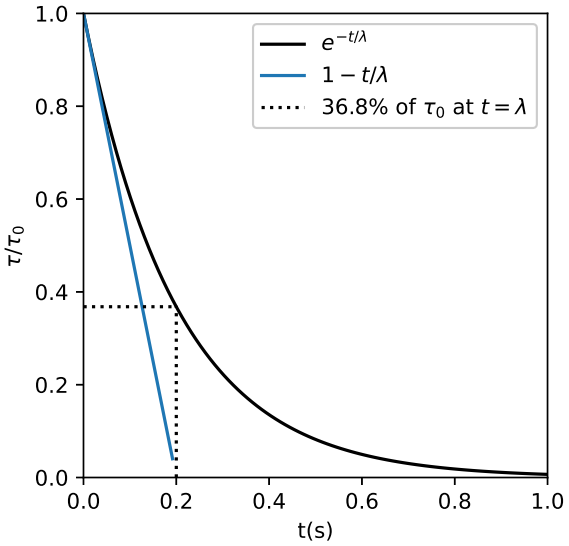

Figure 2.15: Stress relaxation behaviour of Maxwell fluid (continuous line), relaxation behaviour following the initial relaxation rate (blue line), 36.8% of initial value at relaxation time λ(dotted line). This Figure is self-made

Relaxation time

To understand λ clearly, let's take an ideal fluid that follows the Maxwell model with single relaxation time, defined as the ratio of viscosity to elastic modulus. The stress response of such a fluid is given by,

$$\tau/\tau_0 = e^{-t/\lambda} \tag{2.41}$$

The relaxation time is when the initial stress approaches zero with the initial relaxation rate at t=0 (see dashed line in Figure. 2.15)[92]. The stress response following the initial relaxation rate is given by

$$\tau/\tau_0 = 1 - t/\lambda \tag{2.42}$$

In other words, relaxation time is defined as the time required for the initial stress to decay to 36.8% of its magnitude following stress response of a Maxwell fluid defined in equation 2.41. It is notable that this idea is analogous to the penetration depth of diffusion. An example behaviour of such a fluid with relaxation time of 0.2s is shown in Figure.2.15.

2.7.2. Upper convective time derivative

Although the Maxwell model works well for an 1D case, it does not obey the objectivity rule for constitutive relations for higher dimensions. Here, the objectivity rule refers that the material properties should be invariant of deformations and rotations with respect to observer's view. In order to solve that, let's take the well known material (A) derivative that connects the Lagrangian change in material to Eulerian frame through first order Taylor approximation and rewriting it for local derivative,

$$\underbrace{\frac{\partial A}{\partial t}}_{\overset{\triangledown}{A}} = \frac{DA}{Dt} - \underline{u} \cdot \underline{\nabla} A \tag{2.43}$$

Now, substituting second order tensor $\underline{\underline{\tau}}$ for A and rewriting[93], the rate of change of stress tensor in a rotating and stretching frame of reference is represented by an Upper-convected time derivative[4, 93],

$$\overset{\triangledown}{\underline{\underline{\tau}}} = \frac{D}{Dt}\underline{\underline{\tau}} - (\underline{\nabla} \underline{u})^T \cdot \underline{\underline{\tau}} - \underline{\underline{\tau}} \cdot (\underline{\nabla} \underline{u}) \tag{2.44}$$

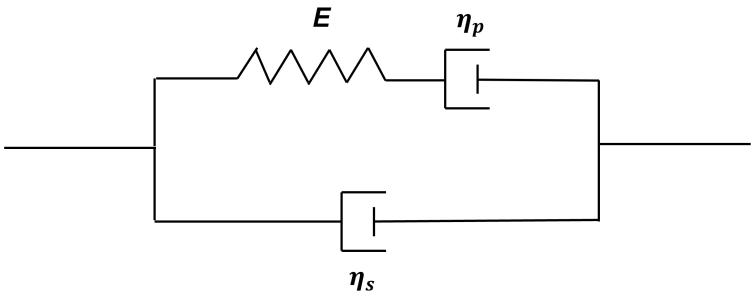

Figure 2.16: Oldroyd-B model with a series of dashpot for polymer viscous contribution η_p and a spring for elastic contribution E, in parallel to a dashpot for solvent viscous contribution η_s. This Figure is self-made, but inspired from [95]

Rewriting the time derivatives with upper convected time derivative in tensor form, we get upper convected maxwell model that obeys objectivity,

$$\underline{\underline{\tau}} + \lambda \overset{\triangledown}{\underline{\underline{\tau}}} = \eta \overset{\triangledown}{\underline{\underline{\dot{\gamma}}}} \tag{2.45}$$

2.7.3. Oldryod-B model

Let's start with Jeffry's model, which looks the same as Oldroyd-B model in 1D. It consists of a dashpot parallel to a series of spring and a dashpot. Here, the dashpot in parallel corresponds to the solvent contribution whereas, series dashpot corresponds to polymer contribution as in Figure.2.16. The objects in series experience the equal stress, whereas it is equal strain for parallel. Beginning with objects in series, which is derived the same as maxwell model.

$$\tau_1 + \frac{\eta_p}{E}\dot{\tau}_1 = \eta_p \dot{\gamma} \tag{2.46}$$

where η_p is the viscosity contribution due to polymer. The total zero shear viscosity is given by $\eta_0 = \eta_p + \eta_s$, in which η_s is solvent viscosity. Now, this object and the solvent dashpot are in parallel, where both experiences the same strain, but different stresses. Solving the mechanical system with , relaxation time $\lambda = \frac{\eta_p}{E}$ and retardation time $\lambda_r = \lambda \frac{\eta_s}{\eta_0}$, we get

$$\tau + \lambda \dot{\tau} = \eta_0 (\lambda_r \ddot{\gamma} + \dot{\gamma}) \tag{2.47}$$

Now, writing in tensor form with the upper convected time derivative we get Oldryod-B model,

$$\underline{\underline{\tau}} + \lambda \overset{\triangledown}{\underline{\underline{\tau}}} = \eta_0 (\lambda_r \overset{\triangledown}{\underline{\underline{\dot{\gamma}}}} + \underline{\underline{\dot{\gamma}}}) \tag{2.48}$$

In this model, a relaxation time $\lambda\ (= \lambda_o)$ due to polymer contribution and a retardation time λ_r due to viscous solvent are both used to characterize the fluid unlike maxwell model, which uses one relaxation time (λ_m) for the whole solution.The retardation time λ_r defines the time delay in expression of elastic behaviour where the strain is still accumulating[78]. This model can predict both creep and stress relaxation behaviours of viscoelastic fluids, with some limitations[4]. Furthermore, it is useful in splitting the viscous and elastic stress contribution in the Navier-Stokes equation for CFD studies (neglecting the body force),

$$\rho \frac{\partial \underline{u}}{\partial t} + \rho \underline{u} \cdot \underline{\nabla} \underline{u} = -\underline{\nabla} p + \underline{\nabla} \cdot (\underline{\underline{\tau_e}} + \underline{\underline{\tau_v}}) \tag{2.49}$$

$$\underline{\underline{\tau_v}} = \eta_0 \underline{\underline{\dot{\gamma}}} \tag{2.50}$$

where,$\underline{\underline{\tau_v}}$ is the viscous stress tensor and $\underline{\underline{\tau_e}}$ is the elastic stress tensor. Now, $\underline{\underline{\tau_v}}$ is subtracted from total stress $\underline{\underline{\tau}}$ in equation 2.48. The elastic stress can be written as [94]

$$\underline{\underline{\tau_e}} + \lambda \overset{\triangledown}{\underline{\underline{\tau_e}}} = \eta_0 (\lambda - \lambda_r) \overset{\triangledown}{\underline{\underline{\dot{\gamma}}}} \tag{2.51}$$

2.8. Rheology

From the above discussion, we can interpret that, the constitutive equations are primarily predicting the stress relaxation behaviour of viscoelastic fluids using the relaxation time λ. One important point to understand at this juncture is that the viscoelastic fluids also have normal stresses induced perpendicular to the shearing direction. This is a result of polymer relaxation, as shown in Figure.2.17. However, their relaxation behaviour in a shear flow and extensional flow is quite different. In shear flow, fluid components shear past one another, while in extensional flow, fluid component flows away or towards from one other. Therefore, relaxation time for shear and extensional flow have to be measured separately.

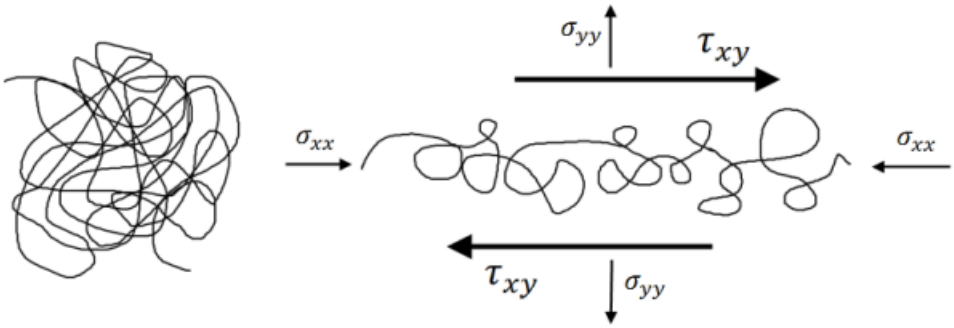

Figure 2.17: Polymer shearing due to shear stress τ_{xy} causes the stretching of polymer chains, and they exert the normal stresses σ_{yy} , σ_{xx} in vertical and horizontal directions respectively. This Figure is taken from [96]

2.8.1. Shear flow

In a typical shear flow, the fluid is placed between two plates and one of them moves, causing a shear strain. The behaviour of viscoelastic materials in such a flow is studied using shear rheology. The main characteristics of sheared viscoelastic materials such as creep, stress relaxation and hysteresis are usually used as test methods to characterize the viscoelastic aspect of the fluid [97].

Hysteresis
Unlike purely elastic materials, viscoelastic materials do not store all the energy, but dissipate some of it. This dissipation can be observed as hysteresis in a cyclic test, that involves repeated stress loading-unloading over the fluid.

Stress relaxation
One more notable characteristic test for a viscoelastic fluid is the stress relaxation test. In a stress relaxation test, a constant strain is applied, resulting in a peak stress that decreases over time.

Creep test
But when stress is held constant in a creep test, strain increases till an asymptotic level, and on removal of stress, strain drops suddenly, followed by an anelastic recovery (recovery over time). [77, 78].

Shear rheometers
The aforementioned characteristics are generally measured using a rheometer, which is a device that measures the response of a fluid to an applied perturbation. This perturbation consists of a predetermined stress or strain, in either shear or extensional directions, and can be either steady or unsteady in nature. In shear rheometers, stress controlled rheometer which measures strain has better torque sensitivity, whereas strain controlled rheometer which measures applied stress can reach higher frequencies. The mechanisms are completely different for both rheometers.For example, in case of strain controlled rheometers both plates are movable, but stress controlled rheometer uses a static plate[98]. An example of stress controlled rheometer is shown in Figure.2.18

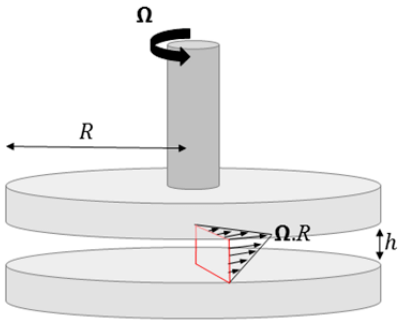

Figure 2.18: A shear controlled rheometer with Plate-Plate geometry with fixed bottom-plate and movable top-plate. The fluid is placed in-between and shear perturbations are applied through the rotation of the top-plate. This Figure is taken from[99]

Types of shear rheometers

As we discussed so far, the shear perturbations are applied to characterize a fluid's response, when placed in-between two parallel plates. The shear perturbations are applied to the fluid using the relative displacement of the plates, as shown in Figure.2.18. Apart from parallel Plate-plate setup, Cone-plate, Couette cell are the other usual geometrical configurations used in a shear rheometer.The Couette geometry has more accuracy compared to others for low viscosity fluids, but then it cannot be used for Small Amplitude Oscillatory Shear (SAOS) tests that measures unsteady moduli of the fluid. Cone-plate has uniform strain rate, unlike Plate-plate, where strain rate depends on radial distance and height. Plate-plate is preferred for change in temperature measurements. Also, the normal stress can be measured better with Cone-plate configuration[4, 96].

Steady viscosity

The steady shear viscosity is the foremost important characteristic of defining a fluid. It is measured by applying a controlled stress or strain-rate and looking at the response of the fluid. The viscous resistance of this proportionality is given by,

$$\eta = \frac{\tau}{\dot{\gamma}} \tag{2.52}$$

where η is the steady shear viscosity. This is the most important test to characterize both Newtonian and viscoelastic fluids.

Linear viscoelasticity

Unlike Newtonian fluids, unequal and non-zero normal stresses are induced along principal directions of viscoelastic fluids as a result of polymer relaxation.To account for these normal stresses in viscoelastic fluids, extra parameters like N_1, N_2 and Ψ_1 are introduced. The first normal stress difference, N_1 is the normal stress in the flow direction τ_{xx} minus that in the gradient direction τ_{yy}. The second normal stress difference, N_2 is the difference between the normal stress in the gradient direction and that in the neutral direction [100]. The first normal stress difference coefficient Ψ_1 can be measured from N_1,

$$N_1 = \tau_{xx} - \tau_{yy} = \Psi_1 \dot{\gamma}^2 \tag{2.53}$$

Because of the aforementioned normal stresses, a viscoelastic material can be classified as linearly viscoelastic (stress is proportional to strain history) and non-linearly viscoelastic. In this study, the focus is on linear viscoelastic material, as they are widely prevalent and less complex. At this instance, it is important to note that the previously discussed Maxwell and Olryod-B models work only for linear viscoelastic fluids. Therefore, we need to limit ourselves within Linear Viscoelastic region.

Oscillatory test

Unlike steady shear measurements for viscosity, characterizing viscoelasticity requires a time dependent Small Amplitude Oscillatory Shear (SAOS) test. In a parallel plate measuring system, SAOS is performed by loading sample between the plates at a known gap and the top-plate oscillated sinusoidally for increasing frequencies. If a very low viscosity sample (water) is to be measured at low

shear rates, a large surface area is used to maximize the torque response from the applied shear rate. The gap is chosen such the instabilities are avoided. SAOS provides the dynamic moduli of a material, that enables Amplitude sweep and frequency sweep to characterize a viscoelastic fluid. An amplitude sweep looks at the dynamic moduli of a viscoelastic fluid for a sinusoidal perturbation that has constant frequency and varying amplitude. On the other hand, frequency sweeps looks at the dynamic moduli by varying frequency at constant amplitude.

Amplitude sweep

As we discussed so far, a linear viscoelastic model can determine the elastic stress relaxation timescale λ using a frequency sweep (discussed in the next section). Therefore, the frequency sweep should be done within a linear response region of a viscoelastic fluid. First, amplitude sweep is done to identify an amplitude within linear viscoelastic (LVE) limit that can be used in frequency sweep. For amplitude sweeps, the strain amplitude is increased step-wise from one measuring point to the next while keeping the frequency at a constant value. The fluid response to applied stress or strain is characterized using a complex modulus G^*, which can be split into storage modulus G' and loss modulus, G'' as in Equation 2.54. The higher boundary of this LVE region can be detected as the point at which the elastic or loss moduli is no longer a horizontal line on a log-log plot of G', G'' vs strain, as in Figure 2.19. If $G' > G''$, then the sample refers a viscoelastic solid material, whereas if $G'' > G'$, the sample refers a viscoelastic liquid as represented in the same figure [101].

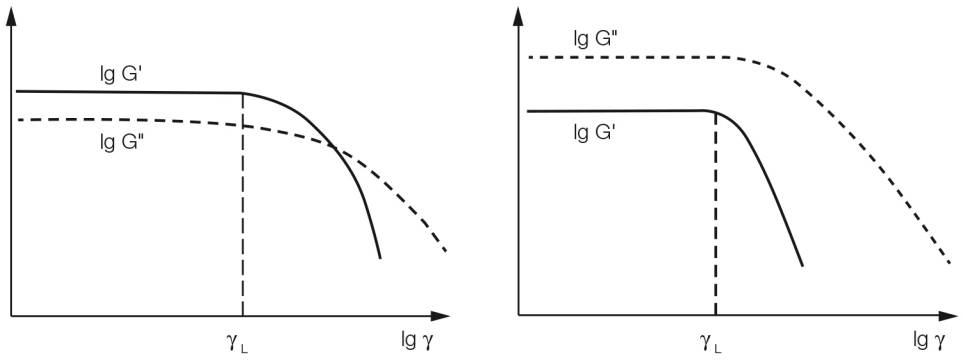

Figure 2.19: LVE region: The boundary of Linear Viscoelastic region is indicated by γ_L. Left-hand side refers to viscoelastic solid material, right-hand side refers to viscoelastic liquid. This Figure is taken from [101]

Frequency sweep

A frequency sweep is important to characterize the relaxation time of a viscoelastic fluid. This test is important to determine the characteristic relaxation time of the fluid, where relaxation time is defined as the time it takes to relax back to an equilibrium position for a shear stretched polymer, as in Figure 2.17 [96, 102]. First, a sinusoidal strain with a strain amplitude γ_0 and an angular frequency ω is applied

$$\gamma(t) = \gamma_0 sin(\omega t)$$

The resulting stress is also sinusoidal with the same frequency, but leads the strain by phase angle δ. An elastic material is said to be in phase, while for viscous material the lag is 90°. For viscoelastic cases, it's between 0 to 90°, where 45° marks the domination of solid like to liquid like properties

$$\tau(t) = \tau_0 sin(\omega t + \delta)$$

The complex shear modulus G^* is the ratio of applied stress to detected strain, which in turn means the stiffness of the material. It is important to split this complex shear modulus into storage modulus G' corresponding to the elastic nature of the material and loss modulus G'' indicating the viscous nature of the material. This is vital in predicting the type of material and its flow behaviour.

$$G^* = G' + iG'', \quad |G^*| = \tau_0/\gamma_0 \tag{2.54}$$

$$G' = G^* cos\delta, \quad G'' = G^* sin\delta$$

The degree of energy dissipation is denoted by $tan\delta$ and it can be derived from the two moduli as ,

$$G''/G' = tan\delta$$

Based on Maxwell's model, the elastic stress decays exponentially with time ($G(t) = G_0 e^{-t/\lambda}$), therefore,

$$G' = \omega \int_0^\infty G(t) sin(\omega t) dt = G_0(\omega\lambda)^2/(1+(\omega\lambda)^2) \tag{2.55}$$

$$G'' = \omega \int_0^\infty G(t) cos(\omega t) dt = G_0(\omega\lambda)/(1+(\omega\lambda)^2) \tag{2.56}$$

Thus when $G' = G''$ at the crossover as in Figure 2.20, $\lambda = \lambda_m = 1/\omega$, where λ_m refers to the relaxation time based on Maxwell model [103, 104]. The different notations of relaxation time such as λ_o (referring to Oldryod-B model) are used in order to indicate the model with which it is based on. This is very important, because not every model can represent the fluid behavior in a single dominant relaxation time like the Maxwell model. Furthermore, λ_s and λ_e are used to distinguish the relaxation time based on the shear flow and extensional flow, respectively.

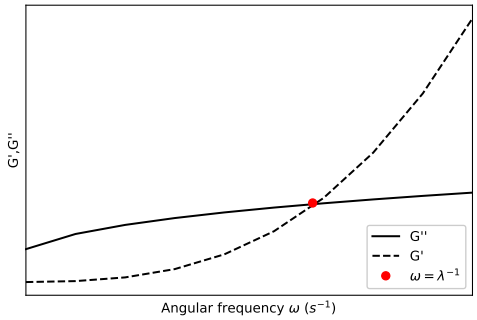

Figure 2.20: Frequency sweep : when the storage modulus G' is equal to loss modulus G'', the maxwell relaxation time can be found as $\omega = \lambda^{-1}$. This figure is self-made

2.8.2. Time-temperature superposition principle

Most shear rheometers have limited frequency of operation highly sensitive to viscosity, thereby limiting the experimental window. This would make the identification of relaxation time difficult. However, this can be solved by using the time-temperature superposition principle. In linear viscoelastic fluids, when the temperature is increased, the viscosity and elastic moduli decreases, but the shape of the curve remains the same. It is based on the idea that at higher temperature (higher energy), the amount of energy required to cross an Arrhenius like energy barrier gets smaller, resulting in faster curve[105]. In other words, the moduli curve at short times of a relatively higher temperature state would exhibit the response same as the longer time response of a lower temperature state shifted by a factor a_T. By using this concept, shift factors are often used to make curves at different temperatures to be overlaped for a master curve in frequency spectrum. The shift factor a_T is given by[106, 107]

$$a_T = e^{-\frac{E_a}{2.303R}(\frac{1}{T} - \frac{1}{T_{ref}})} \approx \frac{\eta(T)}{\eta(T_{ref})} \tag{2.57}$$

Now applying this to frequency-moduli plot along with an empirical vertical shift factor b_T would result in a master curve. This principle can be extended to different moduli and compliance. Furthermore, the factors obtained from viscosity measurements can be verified by fitting it with William-Landel-Ferry (WLF) model, to see if the coefficients are positive. The WFL model is given by[108],

$$log(a_T) = \frac{-C_1(T - T_{ref})}{C_2 + (T - T_{ref})} \tag{2.58}$$

An example of this principle applied to frequency-moduli plot is shown in Figure 2.21 [107].

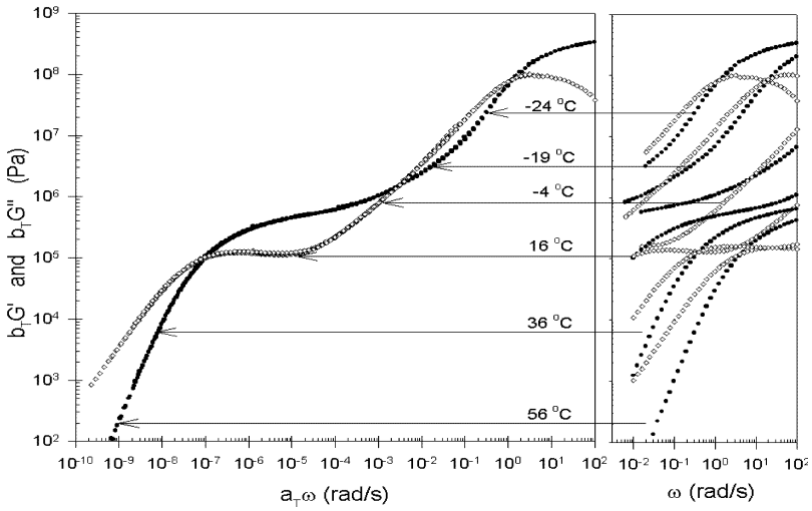

Figure 2.21: Time-temperature superposition principle applied to frequency sweep data of different temperatures This Figure is taken from[107]

2.8.3. Extensional flow

When a fluid element is stretched away from one another in the same axis, it is termed as extensional flow. This is often employed by retracting two circular plates to study the extensional flow behavior of the fluid, which is quite different from shear flow. This is more relevant to this study as it has been argued that, the flow in case of steady cylinder's wake can be considered much like an extensional flow, as the fluid is accelerated from zero to the undisturbed velocity, whereas shear flow is relevant to flow separation[4]. Let's take a case of uniaxial tension in a cylindrical material extended in the x direction, while new material is supplied from the other two directions. The extensional viscosity for such a cylindrical filament can be written as $\eta_e(\dot{\epsilon}) = \frac{N_1}{\dot{\epsilon}}$. The relationship with shear viscosity is given by the Trouton ratio which is the ratio of the transient extensional viscosity and the zero shear rate viscosity, $Tr = \eta_e(\dot{\epsilon})/\eta$. For Newtonian fluids and for extremely slow flows, the ratio is exactly 3, while it can be significantly greater for elastic fluids and are strain-rate dependent. Time and rate-dependence, is often due to strain-hardening and tension-thickening respectively[4, 109]. Depending on the shear viscosity and relaxation time of the fluid, the extensional rheometer can be chosen for characterization as in Figure 2.22 [110]. CaBER corresponds to Capillary breakup extensional rheometer; FiSER to Filament stretching extensional rheometer; EVF the Extensional viscosity fixture; SER to Sentmanat extensional rheometer. In this study, the focus of extensional rheology is limited to characterization of extensional relaxation time λ_e

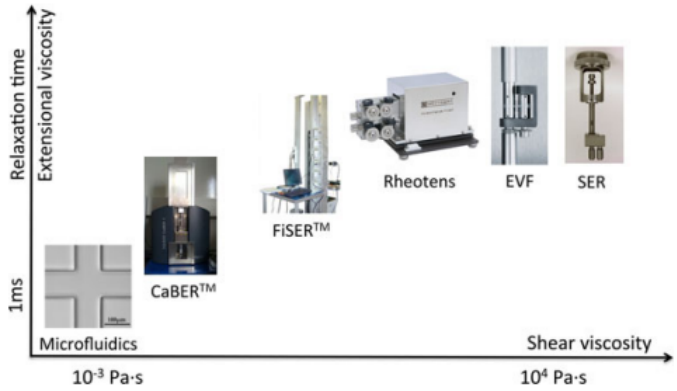

Figure 2.22: Optimal choice of extensional rheometers based on shear viscosity and relaxation time. This Figure is taken from[110]

Solvent	c (PAM)	M_w (PAM)	NaCl (wt%)	$\eta\ (mPas)$	$\lambda_s\ (s)$	$\lambda_e\ (s)$
Deionised water[106]	50	18 x 10^6	0	-	-	0.01
	125		0	-	-	0.059
	250		0	-	-	0.098
	400		0	-	-	0.105
	50		1	1	-	0.004
	125		1	1.05	-	0.01
	250		1	1.43	-	0.018
	400		1	4.5	-	0.029
60% Glycerol[117]	2000	5-6x10^6	0	36 (η_0)	0.0367(λ_m)	-
85% Glycerol[114]	200	-	1	160	0.13 (λ_o)	0.0867
	400	-	1	180	0.197 (λ_o)	0.0977
88% Glycerol[118]	350	15x10^6	0	220 (η_0)	-	0.19
90% Glycerol[115]	100	-	1.5	487	1.947(λ_o)	-
	300	-	1.5	735	1.952(λ_o)	-

Table 2.1: PAM Boger fluids based on glycerol-water mixture, where λ_e is the extensional relaxation time and λ_s is the shear relaxation time represented either using λ_m, the Maxwell relaxation time or λ_o, the Oldryod-B relaxation time

2.9. Boger fluids

A general Non-Newtonian fluid exhibits stress dependent and time dependent viscosity along with viscoelasticity, as discussed earlier in section 3.3. We want to isolate viscoelasticity from other effects, therefore we need a fluid which has minimal to no stress and time dependent effects other than viscoelasticity. In Non-Newtonian theory, viscoelastic and shear thinning fluids can be classified based on a simple shear experiment as[111],

- A viscoelastic fluid that exhibits shear thinning properties as well as elastic properties. In this type, the viscosity decreases with shear rate and normal stress effects are detectable by normal stress differences N_1 and N_2
- A shear thinning fluid, which exhibits shear thinning properties but hardly any normal stress effects
- A fluid which exhibits elastic behaviour but maintains a steady shear viscosity independent of shear rate. Such a fluid is called Boger fluid

To understand the effects of viscoelastic effects independently, Boger fluids can be used. A Boger fluid is defined as "highly viscous (constant, or slight shear thinning masked by high viscosity) and highly elastic fluid which exhibits a nearly constant viscosity and which can be processed at room temperature"[87].

2.9.1. Types of Boger fluids

The original Boger fluid was reported to have 0.08% of polyacrylamide (PAM), in a concentrated aqueous corn syrup[84]. Later on, various other Boger fluids have been developed. Boger fluids can be classified broadly into three different categories based on their ingredients as PAM based Boger fluids, Polyisobutylene based Boger fluids and Polystyrene based Boger fluids[112, 113]. Among these, PAM based Boger fluids are much easier to prepare, economic and also Boger fluids of PAM-glycerol- water mixture is used in relevant studies such as flow past a cylinder[4, 114], so PAM based fluids will be preferred in this study. Solvents such as maltose syrup, glucose syrup, corn syrup and glycerol have been used in the past for PAM based Boger fluids, however glycerol-water mixture is predominantly used in the recent, and it also offers more flexibility for tuning the fluid viscosity and relaxation time compared to others[4, 84, 115, 116]. Studies associated with PAM Boger fluid based on glycerol-water mixture are tabulated with important parameters in Table.2.1.

2.9.2. Additions to Boger fluid

Sometimes, when PAM Boger fluids with water based mixture are prepared, repulsive forces increase due to increased negative charges in the polymer (PAM) chain. The repulsive forces lead to chain

stretching and increased hydrodynamic radii of PAM molecules. This causes shear thinning behaviour with high values of viscosity and relaxation time. However, these effects can be reduced by addition of NaCl (Sodium Chloride) as sodium cations neutralize the negative charges, thus reducing the repulsive forces and hydrodynamic radii of stretched case[106]. Therefore, adding NaCl gives the desirable Boger fluids as they can provide nearly constant viscosity response, but with reduced relaxation times. To avoid bacteriological degradation of the solutions, a biocide can also be added (Example:Kathon), whereas for avoiding mechanical degradation, magnetic stirrers should be used at low speeds and kept in a refrigerator prior to their use [115]. However, in this study, we will not add any biocide, but keep the solution in a safe and clean container.The extension of the chains in a flow causes elastic effects, but their net effectiveness depends on how the viscous effects balance them. This net effect can be characterized by a relaxation timescale λ.

2.10. How to measure relaxation time?

It is often the case that it is difficult to obtain relaxation time directly with a simple frequency sweep (refer section 2.8.1) in case of a shear flow and, on the other hand, extensional rheometers are not commonly available. Therefore, other methods of finding relaxation time discussed here will be used to characterize λ.

2.10.1. Shear relaxation time

Carreau-Yasuda

The non-Newtonian fluids, that have both shear thinning and viscoelastic properties, reach a constant viscosity η_∞ at high shear rates. In such fluids, Carreau-Yasuda model can be used to predict the relaxation time λ. The Carreau-Yasuda model is given by,

$$\eta = \eta_\infty + (\eta_0 - \eta_\infty)[1 + (\lambda\dot{\gamma})^a]^{\frac{n-1}{a}} \tag{2.59}$$

However, the applicability is limited to the experimental values of shear thinning and thickening fluids. Here, a is the transition parameter from Newtonian to power law, n is the power law exponent (slope control) and λ is the relaxation time of the fluid that controls curve bending [4, 119].

Zimm's formula

At extremely low concentrations, Zimm's formula is used as a theoretical prediction of relaxation time, given by

$$\lambda_Z = \frac{K\eta_p M_w \eta_s}{R_g T} \quad \text{or} \quad \frac{\eta_s (N^{3/5} z)^3}{K_b T} \tag{2.60}$$

where K is a parameter depending on solvent quality, K_b is Boltzmann constant, N is the number of repeating monomers and z is the length of a single monomer.However, this constant value λ_Z is applicable only for $c/c^* < 0.04$, where c^* is the overlap concentration at which the polymers start to interact and entangle with adjacent chains [120, 121]. The overlap concentration for any solution can be predicted with a viscosity vs concentration curve as in Figure 2.23. Although, we will limit ourselves within c^*, we will be far from Zimm's equation limit to obtain reasonable elastic stresses.

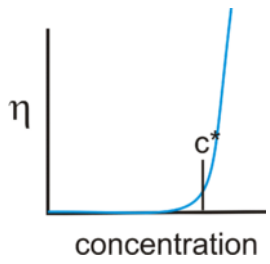

Figure 2.23: Overlap concentration: c^* can be detected where the shear viscosity increases at a significantly higher rate, with increasing concentration, than the lower concentrations[122]

Multimodal (linear) model fit

The general approach used for Boger fluids is to model fit the G' and G'' curves from frequency sweep with multimodal Maxwell or Oldroyd-B models similar to Equations 2.55 and 2.56. The following equations are used to find the relaxation time based on Oldryod-B model λ_o, using G', G" values of frequency sweep[4, 115],

$$G' = \sum_{i=1}^{k} G_i(\omega\lambda_i)^2/(1+(\omega\lambda_i)^2) \tag{2.61}$$

$$G'' = \sum_{i=1}^{k} \eta_i\omega + G_i(\omega\lambda_i)/(1+(\omega\lambda_i)^2) \tag{2.62}$$

Since it gives a spectrum of relaxation times, the mean Oldroyd-B relaxation time can be written as,

$$\lambda_o = \frac{\sum_{i=1}^{k}\eta_i\lambda_i}{\sum_{i=1}^{k}\eta_i} \tag{2.63}$$

The Maxwell relaxation time λ_m can also be calculated by fitting the G' and G'' data from frequency sweep or if the first normal stress difference is known, since $N_1 = 2\eta_p\lambda_m\dot{\gamma}^2$ [87]. In this study, shear relaxation time λ_s will be characterized using λ_o. Overall, a clear difference in λ_m or λ_o values are observed with the above approach and extensional λ_e (see Table.2.1), due to different flow behaviours. Therefore, extensional relaxation time has to be measured separately.

2.10.2. Extensional relaxation time

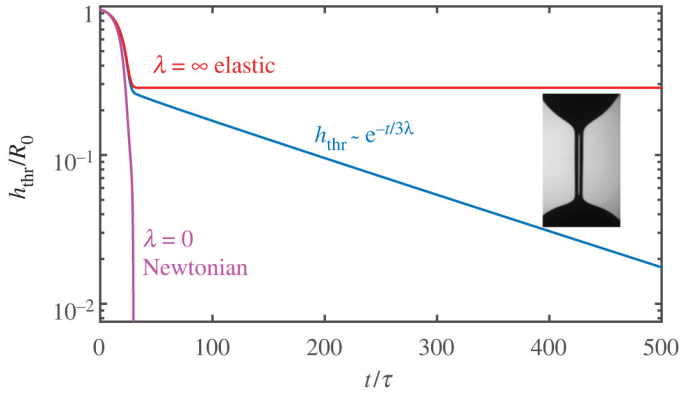

Figure 2.24: Thinning dynamics of a viscoelastic thread is represented by diameter of thinning filament h_{thr}, which falls exponentially unlike elastic and Newtonian materials. This can be used to extract λ_e [95]

Vortex formation and pinch off is a combination of shear and extensional flows[114]. So extensional timescale might be important to characterize the fluid. However, when extensional rheometer is not available, we need an alternative approach. Since filament stretching or extensional thinning is the basis of extensional rheometers, it can also be reproduced with a pendant droplet experiment, where the filament between the droplet and needle thins over time unlike a Newtonian fluid (linear thinning[123]). The initial regime is dominated by inertial and capillary forces, followed by a regime where elasto-capillary forces dominate, in which exponential thinning is observed. The viscous forces during thinning are negligible for fluids with $\eta < 70mPa.s$[124]. For exponential thinning, Oldroyd-B model can be used to predict the longest extensional relaxation time $\lambda = \lambda_e$, provided the model is valid for the fluid (usually for dilute solutions, $c < c^*$) as shown in Figure 2.24. [125, 126].

$$\frac{D_{min}(t)}{D_0} = e^{-t/3\lambda_e} \tag{2.64}$$

where $D_{min}(t)$ is the minimum radius of the filament at time t, and D_0 is the filament diameter at t=0 (needle radius).Furthermore, Oldroyd-B model has been reported to be in agreement with experimental data for dilute viscoelastic fluids in predicting λ_e [125]. One might wonder about the absence of surface

tension in this equation, since the regime is dominated by both elastic and capillary forces. The earlier equation for thinning also included a third power of prefactor called Elasto-capillary number $E_c = \frac{\eta_p D(t)}{2\lambda_e \sigma_t}$. However, it was reported that the polymer selects a constant extension rate just enough to cross the entropic relaxation of the longest mode, when capillary forces are balanced by the viscous solvent and the longest polymeric mode. Based on this, it has been extensively studied that for a constant viscosity solution, exponential thinning can be predicted just by equation.2.64[123]. This was further confirmed by other studies, even with infinite relaxation time λ in an Oldryod-B fluid, equation.2.64 is applicable without accounting for instantaneous E_c [127]. Consequently, the extensional viscosity of an Oldryod-B model η_{ex} is given by[128],

$$\eta_{ex} = \eta_s + \eta_p/(1 - 4Wi_e^2) \tag{2.65}$$

where extensional Wi_e is given by extensional strain rate and relaxation time $\dot{\epsilon}\lambda_e$ and this explains that larger the polymer added viscosity η_p , larger the extensional viscosity. In real fluids, the extensional viscosity has been reported to be a clear function of Hencky strain (Strain rate integrated over time)[129].

2.11. Effect of viscoelasticity in flow field

So far, we discussed the Newtonian flow fields with vortices and viscoelastic theory. Now, let's try to understand how a flow field is affected by the presence of viscoelasticity.In the past few decades, it has been found that adding long-chain viscoelastic polymers into a flow can reduce turbulent friction losses significantly and studied in detail. It is mainly because of the reduction in wall friction, leading to redistribution of shear in the boundary layer[121]. However, when it comes to a steady flow past a bluff body, most of the studies are theoretical or numerical, and aimed at very low Re regime in cylinder(s) and sphere. In general, viscoelastic flows are characterized by Weissenberg number Wi, Polymer viscosity ratio $\beta_r = \eta_p/\eta$, Reynolds number Re and Elasticity number El as shown in Figure.2.25

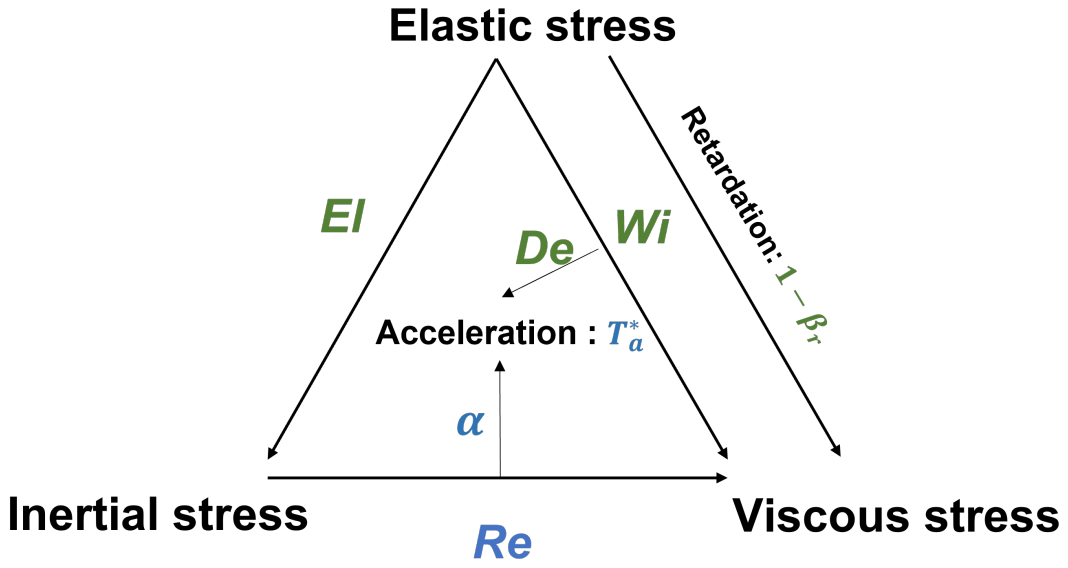

Figure 2.25: Non-dimensional numbers in an accelerating dilute polymeric solution: **Re**ynolds number, **Wei**ssenberg number, **El**asticity number, Polymer viscosity ratio β_r and Dimensionless acceleration α

Non-dimensional numbers

The effect of acceleration a in balancing viscous and inertial stresses is captured by using the non-dimensional acceleration,

$$\alpha = aL_c^3/\nu^2 = Re^2/2T^* \tag{2.66}$$

The Weissenberg number indicates the degree of anisotropy or orientation generated by the deformation[90, 130],

$$Wi = \frac{\text{Elastic stress}}{\text{Viscous stress}} = \frac{\tau_{xx} - \tau_{yy}}{\tau_{xy}} = \lambda\dot{\gamma} \approx \lambda\frac{U}{L_c} \tag{2.67}$$

The Deborah number indicates how solid the material is; the greater the Deborah number, the more solid the material; the smaller the Deborah number, the more fluid it is.

$$De = \frac{\lambda}{t_d} \tag{2.68}$$

where t_d is the characteristic time for deformation. Ideally De is used for flows with clear timescales, such as flagella beating frequency in algae, while Wi is used in cases with simple shear. Although not shown for every case, De for acceleration time as t_d can be derived from target Wi_t and dimensionless acceleration distance T_a^*,

$$De = \frac{2Wi_t}{T_a^*} = \frac{4El\alpha}{Re_t} \tag{2.69}$$

The elasticity number is useful in the regimes where both inertial and elastic forces dominate.

$$El = \frac{Wi}{Re} = \frac{\text{Elastic stress}}{\text{Inertial stress}} = \frac{\lambda\eta}{\rho L_c^2} \tag{2.70}$$

The characteristic relaxation time λ in the above numbers should represent the fluid behavior in a single relaxation time. The Oldryod-B relaxation time represents only the polymer contribution, but not the retardation caused when polymer contribution to viscosity is smaller. Therefore, the shear relaxation time λ_s and the extensional relaxation time λ_e should be used along with the polymer viscosity ratio β_r to define a flow of interest. Out of all the non-dimensional numbers, we will use instantaneous $Wi(t)$ and $\boldsymbol{\beta_r}$ to characterize the elastic nature of fluid, as we may need to understand both steady and unsteady regimes. For inertial and unsteady part, $Re(t)$ and T_a^* respectively will be primarily used throughout, however other parameters will be defined whenever necessary.

2.11.1. Viscoelastic effect on drag forces

In our study, the viscoelastic fluids will be limited to Boger fluids, because the elastic effects are easier to understand. For the laminar range, in an unbounded cylinder, C_D decreases with Re and increases with polymer concentration. The streamlines around the cylinder are displaced (attributed to the presence of normal forces) compared to the Newtonian case[131]. For a Boger fluid in creeping flows for an unbounded cylinder, the drag is not affected by elasticity when $Wi < 0.1$, reduces when $0.1 < Wi < 1$, a plateau appears to exist in $1 < Wi < 2$, and then the drag increases with Wi. The streamlines around the sphere are slightly shifted downstream at small Wi but shifted upstream at higher Wi with some exemptions. Elasticity can affect the wall effects if the blockage ratio is high. In such cases, the drag coefficient decreases in the viscoelastic fluid. If the blockage ratio is small, the drag coefficient increases due to elasticity[132]. An extensive computational study based on the Oldryod-B model helps us to understand the effect of Wi and the polymer viscosity ratio $\beta = \frac{\eta_p}{\eta}$ at a $BR = 0.5$. When Wi is low, the drag of the cylinder is unaffected, but as the Wi increases, the pattern of variation in the cylinder drag depends on the Re. For flows with a low Re, the drag increases as the Wi increases, whereas for flows with vortex shedding, the Newtonian drag dominates till a $Wi = Wi_1$, where Wi_1 is a function of Re. For Wi beyond Wi_1, drag initially decreases and then increases at higher $Wi = Wi_2$, which is also a function of Re. In the same study, the polymer viscosity ratio (polymer contribution to the total viscosity) was found to play a significant role in the drag force changes at both low Re and low Wi numbers, but its effect was negligible for flows with high Reynolds numbers.It has been found that drag reduction and enhancement properties of viscoelasticity are dictated by the critical Wi_1 and Wi_2.The phenomena of drag alteration as a function of Wi and Re is illustrated in Figure 2.26 that represents viscosity ratio of 0.01[133].

2.11.2. Viscoelastic flow characteristics

An increase in cylinder aspect ratio and fluid elasticity reduced the various critical Reynolds numbers that alters the flow regimes in a cylinder (discussed earlier with Newtonian flows). The extension of

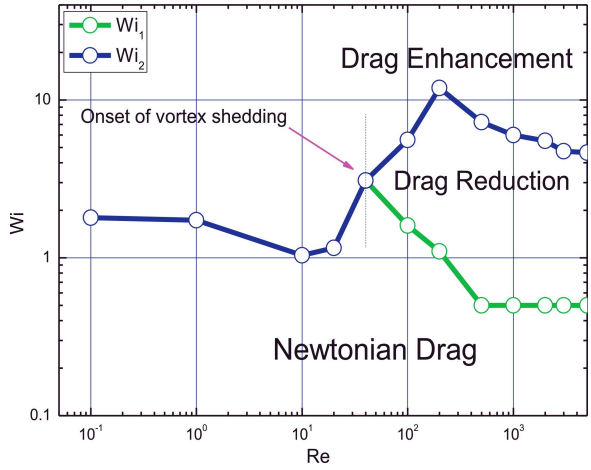

Figure 2.26: This graph provides an example of drag modification with respect to Newtonian in $Wi - Re$ space for flow past cylinder and $\beta_r = 0.01$. Wi_1 indicates the onset of drag reduction compared to Newtonian drag, and Wi_2 ($> Wi_1$) indicates the onset of drag force enhancement from Newtonian. This graph is taken from [133]

the wake transition regime was reduced by fluid elasticity significantly depending on concentration of polymers, for instance 0.4% carboxymethyl cellulose at higher aspect ratios ended at Re=208, which is 2000 in Newtonian case. It is also concluded that El is a better way to characterize the flow[134]. The vortex shedding frequency and the vorticity of the shed vortices were reduced for increasing polymer concentration. The wake was stabilized by polymer additives and the critical Re increased linearly with polymer concentration for constant viscosity solutions[135]. The stoke's flow behavior is altered if $Wi > 6$, as vortices behind the cylinder are stretched gradually. For Re =100, the vortex shedding is gradually suppressed with increasing Wi and totally stops around $Wi = 6$[133]. In the flow past the cylinder, the maximum streamwise normal stresses in the wake increase as De^3 and De^5 for low and high Deborah numbers, respectively. It has been demonstrated that the vortex shedding frequency was much lower for the viscoelastic fluid than for water.[136].

2.11.3. Viscoelastic instabilities

Due to the presence of elastic effects, the instabilities (the physical characteristics that alters the flow behaviour at critical non-dimensional numbers) that can possibly happen in a flow can either be fully due to elastic effects at low Re or Inertial and elastic effects at high Re. For the cylinder, the streamwise velocity indicated no change with increasing Wi in upstream of the cylinder, whereas the downstream wake extended with increasing Wi. Beyond a critical Wi, a flow instability is observed which can be characterized as a transition from steady, 2D flow to a 3D, spatially periodic cellular structure[137]. The curvature of the cylinder provides a perturbation to the fluid streamlines that can initiate viscoelastic instabilities above a critical condition. The onset of elastic instability is found to be scaling with characteristic curvature of the flow and stress along the streamlines called Pakdel-McKinley scaling[90],

$$\frac{\lambda u N_1}{R|\tau|} >= M^2 \tag{2.71}$$

where M is the viscoelastic Mach number. In order to take the speed of viscoelastic shear waves into account c_s, M is defined as

$$M = \frac{u}{c_s} = (ReWi)^{1/2} \tag{2.72}$$

Flows above high viscoelastic Mach number result in a change of type in the underlying constitutive equations, from parabolic (similar to a diffusion equation) to hyperbolic (similar to a wave equation), and give rise to many anomalous phenomena in the inertio-elastic flow of complex fluid. The disturbance of the elastic instability propagates far upstream in the form of an elastic wave, yet remains relatively isolated from the flow in the cylinder wake. The elastic wave speed is found to increase with increasing Wi[90]. The peculiar phenomena of negative wakes has been found to have multiple regimes if they onset with conditions favoring them. They are classified into the creeping flow type front wake ($Wi < 2$),

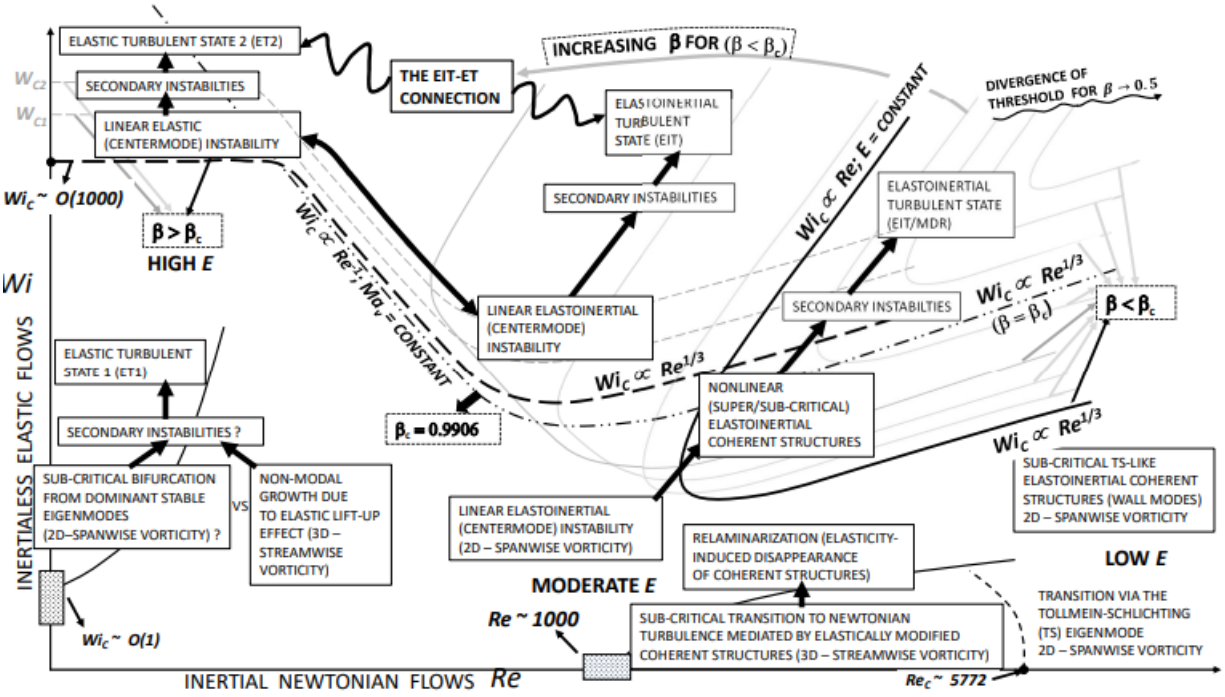

Figure 2.27: Instabilities in a viscoelastic planar poiseuille flow[90]

$Wi >= 2$ with two steady vortices , $Wi >= 4$ representing vortices fluctuating weakly in time, Wi>9 representing vortices fluctuatingly generate and degenerate with time. These front vortices are formed by suppression of back vortices, these are found to be formed for minimization of the flow extension due to high fluid extensional viscosity, by providing a long entrance path reducing extension rate[138]. Unlike the extensive literature for cylinders and spheres, viscoelastic flow past a normal flat plate is quite limited to few early studies long before the Boger fluids were developed. It was concluded that the effects of elasticity are well observed near the leading edge of the plate as the shear rates are high around there, furthermore the history of deformation was not seem to affect the flow in far wake[139].

2.11.4. Unsteady kinematics in viscoelastic flow

In unsteady kinematics involving viscoelastic fluids, the literature is found to be very scarce with some exceptions like unsteady motion of sphere falling in gravity and few other cases in numerical studies with cylinder. Even in these cases, the fluids are shear dependent, hence the elastic effects of flow past unsteady bluff bodies is largely unknown. However, in order to distinguish the free stream instabilities from the effects of the bluff body, we need to know the critical numbers Re_c, De_c, β_c and M associated with a planar viscoelastic poiseuille flow which are represented in Figure 2.27. From this figure it is noticeable that the elastic instabilities are bound to happen for Wi of order greater than one. Similarly, inertial-elastic instabilities are found to occur at high Re around a thousand of order. In this study, we are interested in the elastic effects on vortex shedding, which means we need to be away from poiseuille flow viscoelastic instabilities. Therefore, we will be looking at orders of $Wi < 1$ and $Re < 1000$ to avoid the interplay of elastic and inertial forces. This region will be the focus of this study and termed throughout as weakly elastic, inertial regime. [88, 140].

2.12. Flow visualisation

In order to quantify the effects of elastic stresses in vortex shedding and their scaling, experimental measurements have to be done for these flows. Early flow visualisation techniques based on particles developed by the likes of Friedrich Ahlborn were mostly qualitative, and promoted by prominent

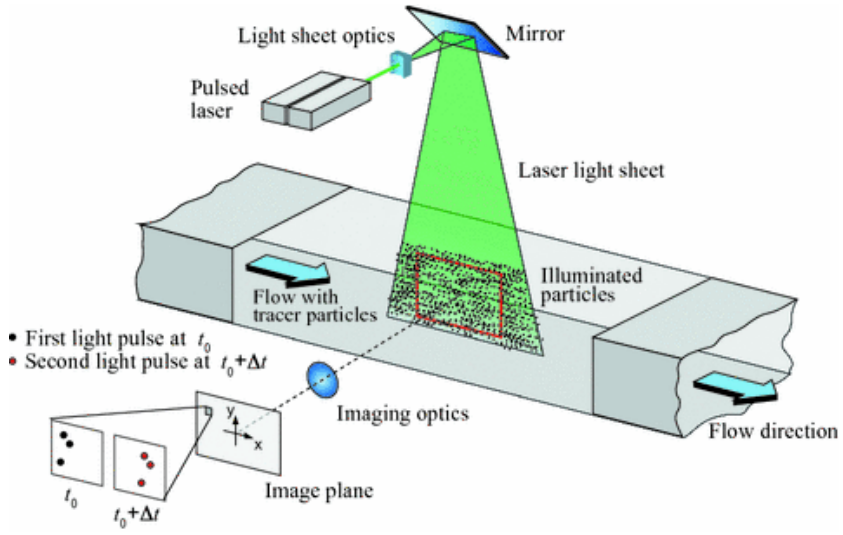

Figure 2.28: A typical 2D-2C PIV setup to extract the flow field data[142]

people like Ludwig Prandtl. Development of better lasers and sophisticated data processing methods have led to quantitative flow visualisation. In order to determine flow velocity, various indirect intrusive methods like pressure probes, hot wire, hydrogen bubbles exist. However, direct optical methods such as Laser Doppler Velocimetry (LDV), Laser Two Focus and Particle Image Velocimetry (PIV) provide non-intrusive velocity measurements. Measurements based on particles can be classified based on the increasing density of tracer particles as Particle Tracking Velocimetry , Particle Image Velocimetry, Laser speckle Velocimetry, whereas in this study we focus on Particle Image Velocimetry as it has become a nearly standard way of measurements.

2.12.1. Particle Image Velocimetry

In PIV, the fluid is seeded with particles which closely follow the flow dynamics. The velocity is calculated from the motion of these seeding particles by taking two images with a short time gap Δt and the distance is calculated based on the displacement of the seeding particles between the two images. In the design of PIV experiment, the prioritized goals are high spatial and temporal resolution of field, good enough to capture the dynamics of the flow field of interest and its velocity fluctuations. PIV can be implemented as Double exposure/single frame and Single exposure/ double frame, however single exposure/double frame is preferable as double exposure/single frame processes with auto correlation which has inherent limitations. Therefore we will focus on single exposure/double frame which uses cross correlation[141].

Spatial configurations

Depending on the spatial configuration, PIV can be classified into planar (2D-2C) with one camera, stereoscopic (2D-3C) with two cameras, and volumetric (3D-3C) with multiple cameras, where D refers to Dimension and C to Component. However, in this study we stick to planar (2D-2C) setup that looks as in Figure.2.28. Initially, the particles are seeded with tracer particles followed by two frame snapshot recordings of the flow illuminated by synchronized laser sheet separated with a time Δt. Thereafter, the scattered light intensity due to particles as an ensemble is correlated to find the displacement and velocity vectors[142]. The typical subsystems of PIV are Seeding, Illumination, Recording, Calibration, Evaluation, Post Processing. The typical planar 2D-2C PIV based on these subsystems are explained below.

- **Seeding:** The particles are added to the fluid such that they closely follow the flow. The smaller particles follow the flow better whereas larger particles are better with scattering light.To reduce velocity lags, smaller particles are preferred,while they should be large enough for the camera sensitivity. The size of the particles should be of the same density as the fluid to make sure that

they are neutrally buoyant, which can be verified when the stokes number $Stk < 0.1$,

$$Stk = \frac{t_p}{t_c}, \quad t_p = d_p^2 \frac{\rho_p}{18\eta} \tag{2.73}$$

Where t_c is the characteristic time scale of the flow and ρ_p is the particle density. Usually particles of mean diameter d_p = 10-100 μm is used in liquid flows.

- **Illumination:** A laser pulse is used to illuminate the seeded particles for recording. The duration of the light pulse should be low enough to freeze the motion of particles, whereas the time delay between two pulses should be long enough to see displacement of particles between images, and short enough not to see too many particles with out of field components leaving the light sheet. The light sheet (to freeze the flow) is produced by pulsed lasers typically Neodymium-doped Yttrium Aluminum Garnet crystal (Nd-YAG) laser.
- **Recording** The recording usually is done using a CCD (Charge coupled device) or CMOS (Complementary metal oxide sensor) based high speed camera. Usually a frequency of 10-20Hz is employed (CCD based), but can also be 1-100kHz (CMOS based) depending on time scale of flow phenomena. A synchroniser is used in order to match the pulses of laser and the exposure time in the camera.
- **Calibration:** An optical setup with cylindrical or spherical lens is used in order to focus the laser into a thin plane of light sheet. However, the recording is done only after a calibration of grid to pixels is done as a means of understanding spatial resolutions in image resolutions and the spatial resolution should be good enough to capture the velocity gradients in the field [142, 143].
- **Evaluation:** Since the particle density is high, the evaluation is done with ensembles of images, not with individual particles. This ensembles of images stacked together is called an interrogation window, and each interrogation window determines one velocity vector by correlation methods.
  - **Interrogation window:** The interrogation windows should be big enough for several particle images ensuring a high valid detection probability of the velocity vector. In case of constant gradients, very less bias error is detected, whereas for varying gradients like boundary layer, the interrogation-window size and the optical magnification should be resolve according to the scales of interest to reduce errors[144].
  - **Cross-correlation:** Once the image ensembles are available, cross-correlation of intensities is used for the interrogation windows with a gap Δt. The peak value of the cross correlation is used to predict the average displacement of particles in an interrogation area and velocity can be calculated given Δt. Often, Fast Fourier Transforms are used to perform cross correlations to reduce computational cost[145].
  - **Uncertainty:** Similar to any other experimental method, PIV also has errors and uncertainty associated with it. The major sources of systematic error are tracer particle response, hardware synchronization, Interrogation window size and algorithm, etc. These uncertainties can be quantified by various direct and indirect approaches such as Uncertainty surface, Cross-correlation signal-to-noise ratio metrics, Correlation statistics and particle disparity[146].

2.12.2. Does viscoelasticity affect PIV measurements?

PIV experiments are predominantly done in simple Newtonian fluids. Although, a few studies have used PIV on viscoelastic fluids[115, 135], one might wonder whether viscoelasticity affects the tracer particles in following streamlines without interacting with each other. One study showed, that particles in *shear thinning polymeric* fluids even in low volumetric concentrations can sometimes interact, causing particle chain or string formation. However, it was further studied and concluded that even in shear thinning viscoelastic fluids, PIV measurements are completely unaffected[147]. Sometimes, the behaviour of neutrally buoyant stokes flow particles in viscoelastic fluids, might be confused with generalization of particle migration in microchannel flows. It has to be noted that such behaviours scale with both Deborah number De and square of blockage ratio, whereas a vortex shedding study like our case would have minimal blockage ratio[148]. Furthermore, such migration behavior of particles is due to competing effects of fluid shear thinning and elasticity. But in this study, we will use a boger fluid with almost no shear thinning[148]. Hence, PIV measurements in this study can be safely assumed to not be affected by viscoelasticity .

2.13. Feature extraction

Once we have the PIV data, we will be looking for interpretable patterns and features of the flow. However, it is hard to recognize such patterns and the wake behaviour with raw velocity data, and so we need a feature extraction process that can convert velocity to easily recognizable visualizations for the flow features. In this study, we will focus on Q-criterion and Lagrangian Coherent Structures (LCS), to understand the vortex dynamics.

2.13.1. Q-criterion

The strain rate tensor (velocity gradient) can be decomposed into shear rate $\dot{\gamma} = \frac{1}{2}(\nabla u + \nabla u^T)$ and rotation rate , $R = \frac{1}{2}(\nabla u - \nabla u^T)$. A vortex is a region of high rotation rate as it is a concentrated region of vorticity. Therefore a rotationally dominant region can be identified using $Q > 0$, where Q is defined as

$$Q = \frac{1}{2}(|R|^2 - |\dot{\gamma}|^2) \tag{2.74}$$

Formally, when we perform eigen value decomposition of the velocity gradient, we end up with a characteristic equation,

$$\lambda^3 + P\lambda^2 + Q\lambda + M = 0 \tag{2.75}$$

where P,Q,M are the invariants and λ is the eigen value. Thus Q is defined as the second invariant of velocity gradient[149].

2.13.2. Lagrangian Coherent Structures

The coherent structures that we are interested in this study are the vortices and derivatives formed due to flow around the geometry. When we try to track these structures in Lagrangian fluid motion, they are inherently unstable due to their sensitivity to initial conditions. These dynamically distinct regions of space (coherent structures) can be separated by invariant manifolds called separatrices, which often change with time in unsteady systems. LCS as complimentary approach has an edge over eulerian coherent structures (like Q-criterion, λ_2 criterion) by separating these structures into dynamically distinct regions of space with less ambiguity and more objectivity[150]. Let's consider a hyperbolic point as in Figure.2.29. The points either side of stable manifold (vertical axis) diverge when integrated forward in time, whereas points on either side of the unstable manifold (horizontal axis) diverge when integrated backward in time [151]. Since separatrices divide these regions, the coherent structures can be defined based on maximum divergence or stretching. FTLE provides a simpler way of evaluating the divergence between trajectories. Therefore, ridges of Finite Time Lyapunov Exponents (FTLE) are used as a diagnostic approach to extract the approximate Lagrangian Coherent Structures (LCS) in unsteady cases.

FTLE based approach

In FTLE based diagnostic approach, first a flow map $\mathbf{\Phi}_0^T(x_0)$ is made from points arranged in a Cartesian grid, which changes its skeleton to a different structure after some time T_n. To understand where the fluid comes from (or entrainment), it can be integrated backward in time, referring to the stable manifold(Negative-FTLE). On the other hand, to understand how it separates forward, it has to be integrated forward in time(Positive-FTLE). This corresponds to unstable manifold called repelling surfaces.

$$x(t) = x_0 + \int_0^{T_n} (u(x(t), t)dt = \mathbf{\Phi}_0^{T_n}(x_0) \tag{2.76}$$

Then, for each material element of these points, the deformation and rotation has to be calculated by making a Jacobian of the flow map, for which the determinant should be approximately one for incompressible flows.

$$D\mathbf{\Phi}_0^{T_n} \approx \begin{bmatrix} \frac{\Delta x(T_n)}{\Delta x(0)} & \frac{\Delta x(T_n)}{\Delta y(0)} \\ \frac{\Delta y(T_n)}{\Delta x(0)} & \frac{\Delta y(T_n)}{\Delta y(0)} \end{bmatrix} \tag{2.77}$$

The maximum singular value $\boldsymbol{\lambda}_{max}$ of the Cauchy-Green deformation tensor, $\Delta = (D\mathbf{\Phi}_0^{T_n})^T(D\mathbf{\Phi}_0^{T_n})$ indicates the direction in which the growth of the stretching or perturbation is maximum. Now, the

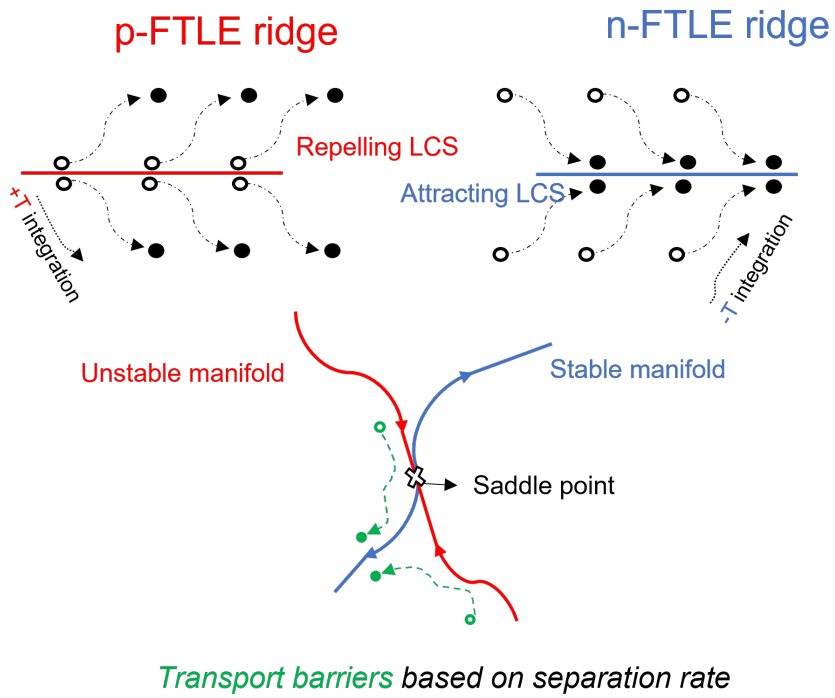

Figure 2.29: Normally attracting (or stable manifold) surface marked by red (integrated forward in time) and normally repelling (or unstable manifold) surface marked by blue (integrated backward in time). The fluid parcels do not pass through FTLE ridges or separatrices making them transport barriers. This figure is self-made, but inspired from [151, 152].

FTLE field is calculated as

$$\sigma(\Phi_0; x_0) = \frac{1}{|T_n|} \log \sqrt{\lambda_{max}(\Delta(x_0))} \tag{2.78}$$

This FTLE field has to be done for every time step in order to understand the entire dynamics of the coherent structures, which are basically invariant manifolds that acts as a boundary for the points to stay in or out according to this theory[150, 153]. The topological Lagrangian saddle points are found to be at intersections of the positive and negative finite-time Lyapunov exponent ridges. Furthermore, the unsteady vortex shedding around a cylinder has been widely studied using this method, an example of negative-time FTLE field for flow around cylinder is presented in Figure 2.30.In case of cylinder, the saddle points are found to be useful in understanding flow separation, vortex formation time and its shedding. When the vortex begins to form behind the wake, the saddle point slowly moves downstream until the vortex sheds. Then, the saddle point accelerates until reaching the advection speed of the vortex [154].

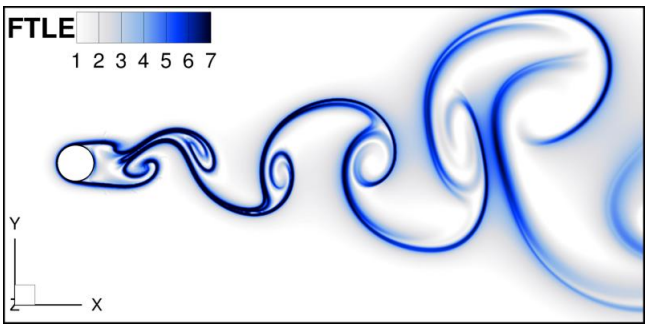

Figure 2.30: Negative-time FTLE field representing unsteady vortices in flow past a cylinder[155]

Although it is widely used, the FTLE based LCS approach suffers from several issues [156],

- FTLE ridges not only highlight hyperbolic LCS (attracting and repelling material surfaces), but also high shear surfaces
- There are other types of LCS such as parabolic and elliptic LCS other than hyperbolic LCS
- Ridges of FTLE are not necessarily LCS and material surfaces

To solve for inconsistencies in LCS based on FTLE, variational theory was proposed based on the idea that the material surfaces acting as centers of patterns (with zero flux across the boundary), identify themselves by attracting or repelling nearby trajectories at the highest rate locally[156]. The hyperbolic LCS gives an invariant manifold, elliptic LCS gives the boundary of vortices and parabolic LCS gives the cores of jet flows. A clear implementation of the hyperbolic LCS algorithm can be found in [157]. However, FTLE fields are much more physically interpretable and less complex. Therefore, we will use FTLE fields to understand the wake and vortex dynamics in this study.

Rotational coherence based Elliptic LCS

Elliptic LCS are closed material surfaces that act as building blocks of lagrangian equivalents of vortices. So what are these coherent vortices? Although there is no universal definition, the widely accepted criteria are concentrated regions of vorticity and evolving invariant material regions[158]. In 2D it can be calculated using different approaches such as polar rotation angle (PRA), Lagrangian averaged vorticity deviation (LAVD), and variational theory[156]. Among these, we limit ourselves to LAVD based on relative rotation tensor as it is dynamically consistent, applicable to 3D flows and simpler to compute. The relative rotation tensor has been proven to be dynamically consistent and therefore the total angle swept by this tensor around its own axis is consistent[158]. Using this idea, the intrinsic rotation angle is defined as in Figure.2.31 and it can be calculated as

$$\psi_0^{T_n} = \frac{1}{2} LAVD \tag{2.79}$$

LAVD can be used to identify lagrangian coherent vortices experiencing same rotation compared to mean rigid body rotation of the flow field. For a 2D planar flow, LAVD is calculated by

$$LAVD_0^{T_n}(x_0) = \int_0^{T_n} |\omega_z(x(s;x_0),s) - \overline{\omega_z}(s)| ds \tag{2.80}$$

where the mean vorticity is given by

$$\overline{\omega_z}(t) = \frac{\int \omega(x,t) dV}{vol(U(t))} \tag{2.81}$$

The initial positions of the vortex centers are found to be the points where LAVD has local maxima that act as attractors for debris and positively buoyant particles, finally the vortex boundaries are chosen with criteria as in [158]. In this study, we will use LAVD to identify the vortex boundaries and advect them separately to understand the dynamics of fluid parcels in a lagrangian frame.

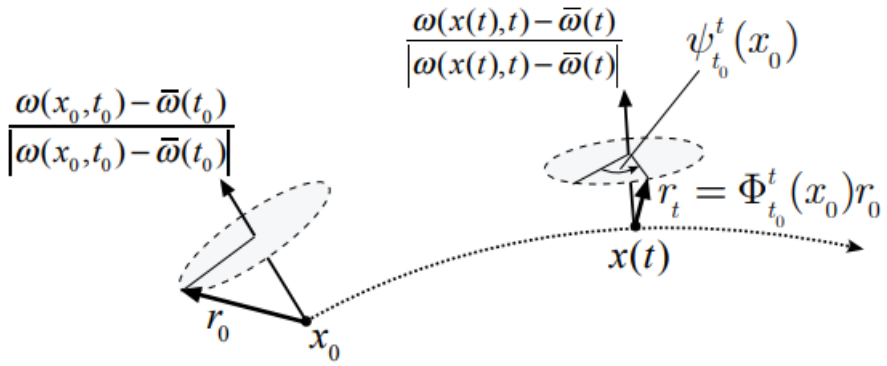

Figure 2.31: Intrinsic rotation angle $\psi_0^{T_n}$ in a deforming material trajectory[158]

2.14. Research objectives

In summary, the vortex shedding due to flow past the cylinder and a flat plate (facing 90°to the flow) has been extensively studied in the past for both steady and unsteady translations in the case of Newtonian fluids. The forces and instabilities have also been quantified well in such cases. Similarly, the vortex shedding due to viscoelastic flow past a steady cylinder has been studied well in both experimental and numerical studies. However, the dynamics of unsteady translations in viscoelastic fluids is very much limited to a few studies in spheres and cylinders with stress-dependent fluids. The dynamics of viscoelastic flow past an accelerating normal flat plate is largely unknown, despite the geometry being rich in information about the flow separation. Furthermore, the effect of elastic forces in accelerating flows has not been reported so far. To improve the focus of the study and to understand the shedding effects clearly, the Wi and Re numbers will be limited to the laminar—weakly elastic vortex shedding regime ($Wi < 0.6$,$50 < Re < 250$) without elastic free stream instabilities as shown in Figure 2.27. Taking into account the statements above, the objectives of this study will be

- To understand the effect of viscoelasticity in wake/vortex ring dynamics in a starting normal flat plate
- To investigate the changes in unsteady forces due to the presence of elastic forces and acceleration.

How?

To achieve the aforementioned objectives,

- Initially ***shear rheological*** experiments on viscosity, amplitude sweep and frequency sweep, followed by extensional ***pendant droplet experiments*** were conducted to identify the Boger fluids with a constant viscosity, shear and extensional relaxation times that allow working in laminar-weakly elastic - vortex shedding regime.
- Then an ***experimental setup*** was designed and fabricated considering the effects of Re,Wi, AR.
- The investigations were carried out, using linear acceleration of flat normal plates in the identified viscoelastic fluid. For this, Particle Image Velocimetry was used to get 2D-2C velocity field data, and a force transducer was used to measure the forces exerted on the flat plate.
- Finally, relevant ***data processing*** techniques were used to extract the features of the flow. They are analyzed along with PIV and force data to understand the phenomena and the scalings involved.

3

Methodology

3.1. Shear Rheology

In order to characterize the fluids for their viscosity and relaxation time, shear rheological experiments were conducted using an *Anton-Paar 302* shear rheometer, as shown in Figure.3.1. In order to be consistent with the measurement technique for both viscosity and oscillatory tests, we are limited to cone-plate and plate-plate configurations. For both cases, the stress σ (based on the torque) depends on the diameter as $\sigma \alpha d^{-3}$, thus larger the diameter, smaller the stress possible. The viscosity of a typical fluid that we are interested in this study should be low enough to reach a maximum of $Re \approx 250$, using a simple stepper motor based linear traverse and a small plate. For such low viscosities (a few times more than water), larger plate diameters (40-60 mm) are needed in order to have sufficient sensitivity[159]. Unfortunately, cone-plate of such large diameters were not available. Therefore, a plate-plate configuration with 50 mm diameter is used throughout the measurements. For a plate-plate configuration, the shear rate (based on angular velocity) scales inversely with gap height between the two plates. However, this gap height should be large enough to avoid the surface roughness effect; but small enough to avoid any instabilities with enough capillary forces to keep the fluid intact. It has been recommended to use a gap of $0.5 - 1mm$ for a plate-plate configuration with a diameter of this range [159].Therefore, a gap of $0.5mm$ will be used throughout the study. The fluid sample has to be prepared before characterizing them; hence, preparation procedure is discussed in the following section.

3.1.1. Fluid preparation

Looking at the Table.2.1 shear relaxation time is a weak function of viscosity, however pure water viscosity is not enough despite high molecular weight and concentration of PAM to a have a reasonable relaxation time with constant viscosity. Also considering the Re requirement into consideration, a glycerol-water mixture between around $50 : 50Wt\%$ will be used as a base solution in the prepara-

Figure 3.1: Shear Rheometer used for fluid characterization

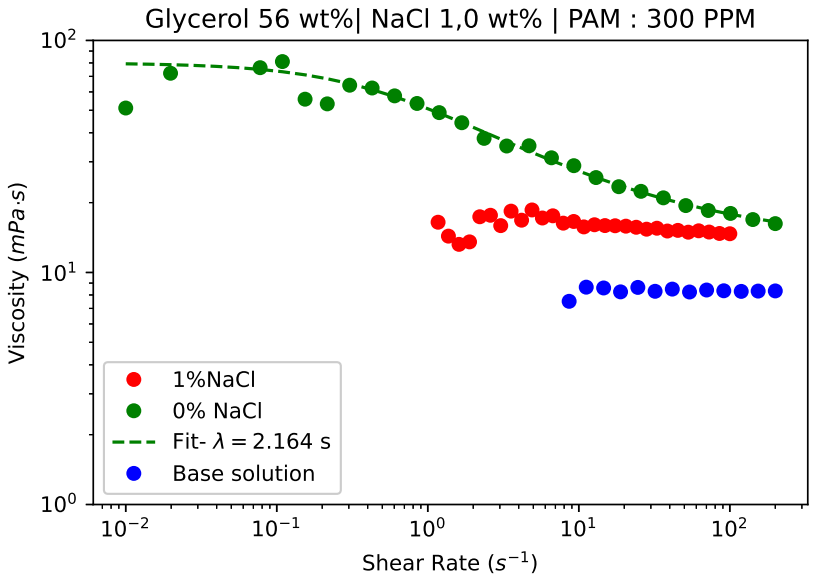

Figure 3.2: Suppression of shear thinning at $20°$ by adding $NaCl$ to Glycerol-Water-PAM solution, λ : Carreau-Yasuda

tion of a viscoelastic fluid. As the relaxation time is a strong function of molecular weight and $NaCl$ reduces it, we will use Polyacrylamide(PAM) with a molecular weight of $18 \times 10^6 g/mol$ based on Table.2.1. $0.5 - 1Wt\%$ NaCl will be used to neutralize some charges in the polymer thereby reducing the shear thinning but with some relaxation behaviour (based on [106]), an example of this behaviour can be seen in Figure.3.2. Initially, glycerol is measured for its viscosity and corresponding purity is estimated. The base solution is then prepared by adding $\approx 56Wt\%$ glycerol with the rest of the deionized water in a closed container. Unfortunately, the zero shear viscosity measurement was not in the sensitivity limit of the Rheometer to measure overlap concentration. However, looking at Table.2.1, the typical dilute concentrations used were 100-400 ppm in both pure water and Glycerol in the presence of NaCl. PAM of desired concentration with $0.5 - 1Wt\%$ of NaCl are added to the base solution. They are allowed to mix using magnetic stirrers at room temperature for approximately 6-12 hours, on the basis of visual inspection for the presence of any inhomogeneous blobs of polymers.

3.1.2. Fluid characterization

To characterize the prepared solution, let's list the procedure in steps as follows,

(A) The viscosity of prepared fluid is measured at temperatures $10 - 40°C$ with intervals of $10°C$
(B) The shift factor a_T is estimated using equation 2.57 with 20 ° as reference (lab temperature).
(C) By fixing an angular frequency of 10 rad/s (assuming an order of $\lambda = 0.1$ s based on Table.2.1), an amplitude sweep is performed to identify the strain limit for the linear behavior of the fluid at different temperatures.
(D) With an amplitude (typically 0.1 strain) less than the identified limit, the frequency sweep is performed to find the curves of G' and G" versus the angular frequency.
(E) Using the Time-Temperature superposition principle as discussed in section 2.8.2, we use a_T as shift factor for angular frequency and an empirical factor b_T for the moduli to make the master curve.
(F) Finally, the Oldryod-B model with 3 modes is fitted to the master curve and relaxation time is calculated as discussed in section 2.10.1

3.1.3. Preliminary experiments

In order to identify and characterize the fluid for the vortex shedding experiments, a set of preliminary rheological experiments were performed in the aforementioned manner. The results are discussed in the following sections

(A-B) Viscosity measurements

As a first step, the base solution was prepared by mixing 56Wt% (50 volume %) of Glycerol and the rest with water. Then, splitting into separate batches, PAM of concentrations 100,300,400 ppm were prepared. The weight of the solutions was measured and 1 $Wt\%NaCl$ was added to each batch. By measuring viscosity at different temperatures, the shift factor is calculated and cross-checked by looking for positive constants C_1, C_2 in William-Landel-Ferry model as shown in Figure.3.3. For this, mean viscosity for shear rate>20s^{-1} is used, avoiding the noisy measurements.

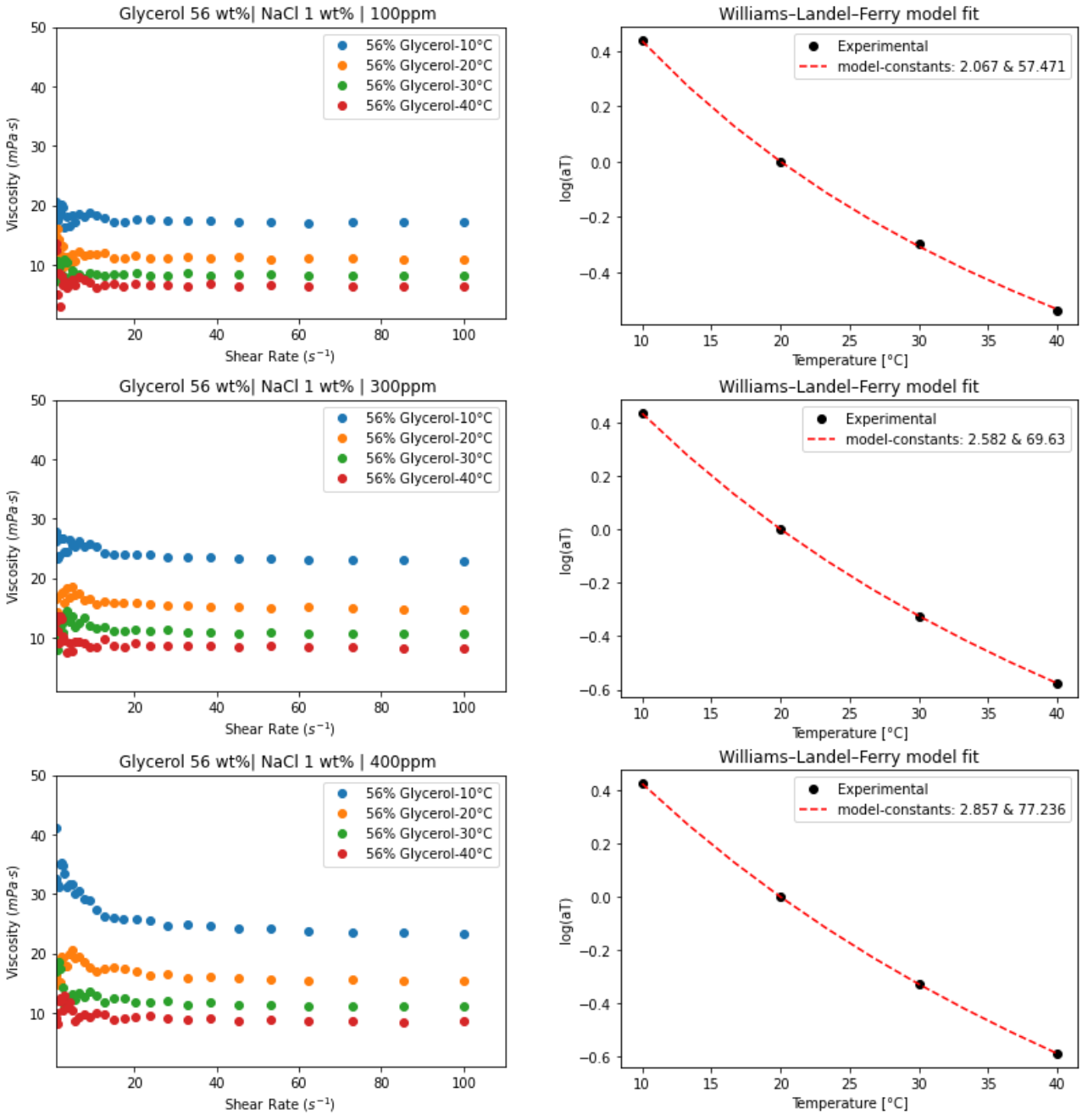

Figure 3.3: Viscosity measurement and shift factor estimation

(C) Amplitude sweep

The amplitude sweep, with a constant angular frequency of 10 rad/s, was conducted in the same way as the viscosity measurements, for the corresponding PAM concentrations. It has been found that the fluids were behaving in the linear viscoelastic range for shear strain < 1, in all the concentrations measured. Unfortunately, the measurements for 100 ppm is noisy at high temperatures mainly because of the sensitivity limit of measurement device. Therefore, 100 ppm is not pursued further. The results of the amplitude sweep is shown in Figure.3.4

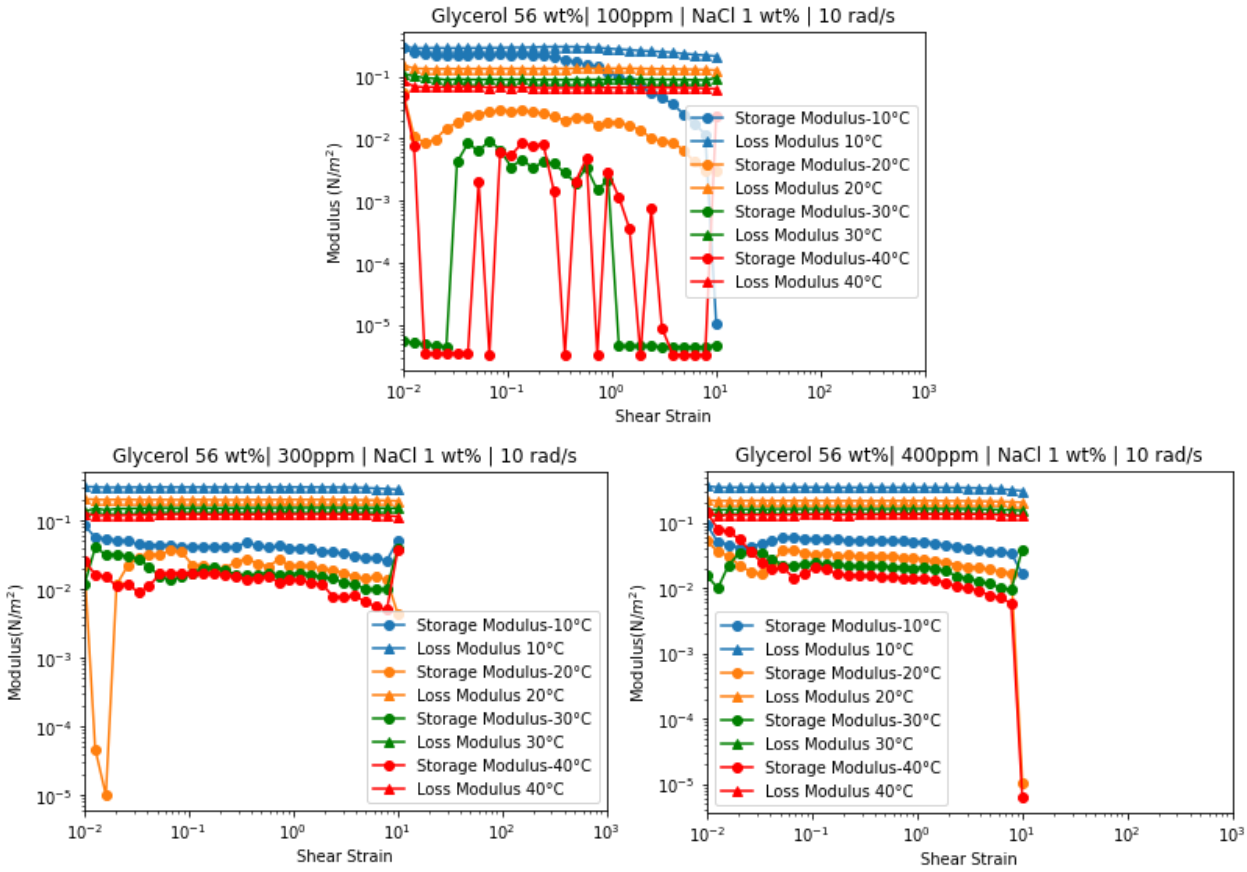

Figure 3.4: Amplitude sweep of the prepared fluids

(D-F) Frequency sweep

Once, the strain amplitude limit was found by amplitude sweep, frequency sweep was carried out with a shear strain amplitude of 0.1. Then the previously estimated shift factor a_T is applied to the angular frequency and an empirical factor b_T was applied to the moduli to make the master curve. Thereafter, equations 2.62 and 2.61 were fitted to the master curve and the relaxation times were estimated as model constants. The fitting was done with Levenberg-Marquardt algorithm for minimization of the least squares using SciPy.optimize.curve_fit. For 300ppm, data at $40°C$ was not used in fitting as the data for storage modulus was off from the curve, mainly because of noisy measurement due to low modulus at high temperature. The results are shown in Figure 3.5.

3.1.4. Shear Relaxation time

All the above procedures were repeated for a lower Glycerol concentration of, $42Wt\%$ and the relaxation time was estimated. However, due to the space constrain, we report the final relaxation time without each graph in steps. The Oldroyd-B shear relaxation (λ_s) time was found to be a very weak function of Glycerol concentration and a strong function of PAM concentration. The identified relaxation times are reported in Figure 3.6

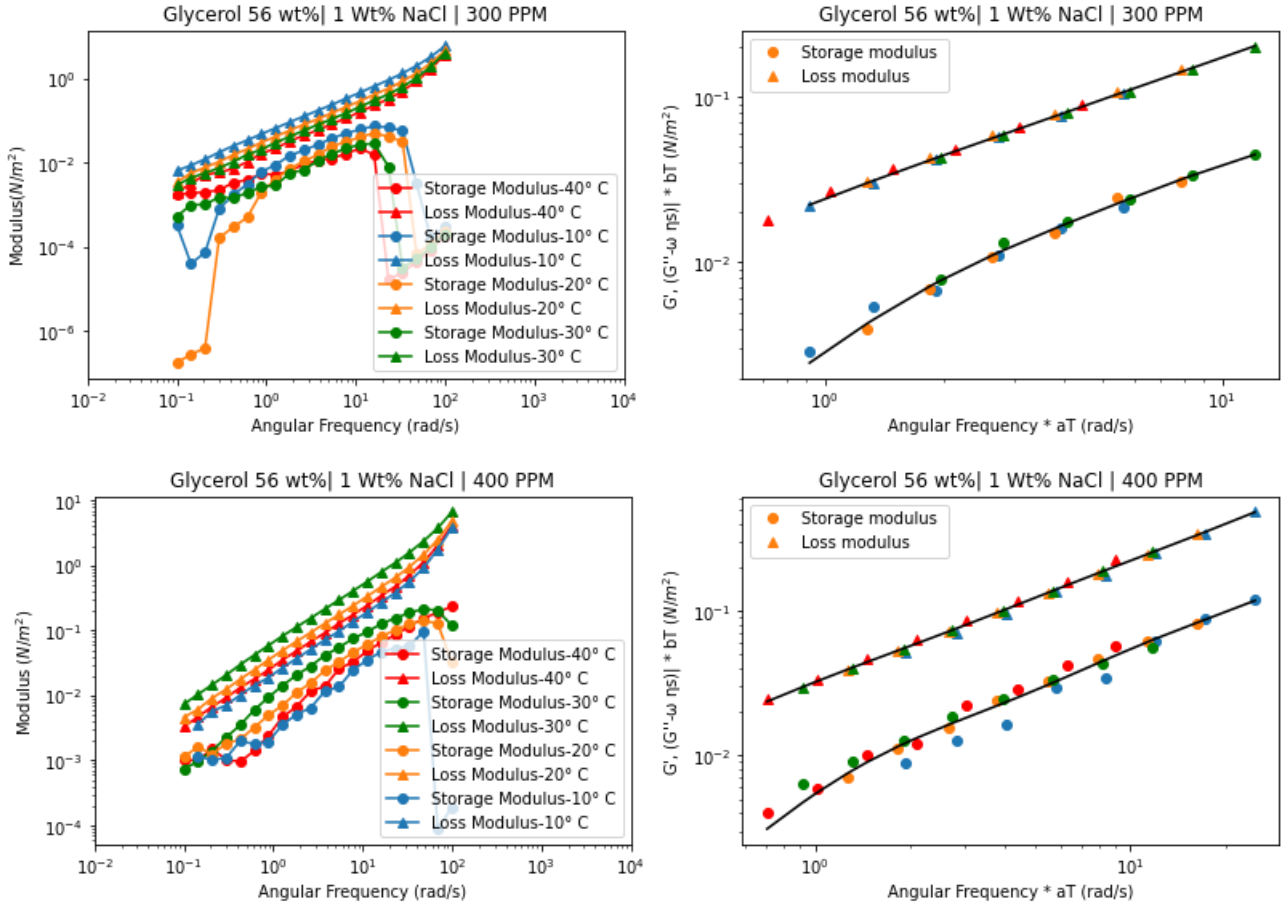

Figure 3.5: Frequency sweep, Oldroyd-B fit after applying Time-Temperature superposition principle

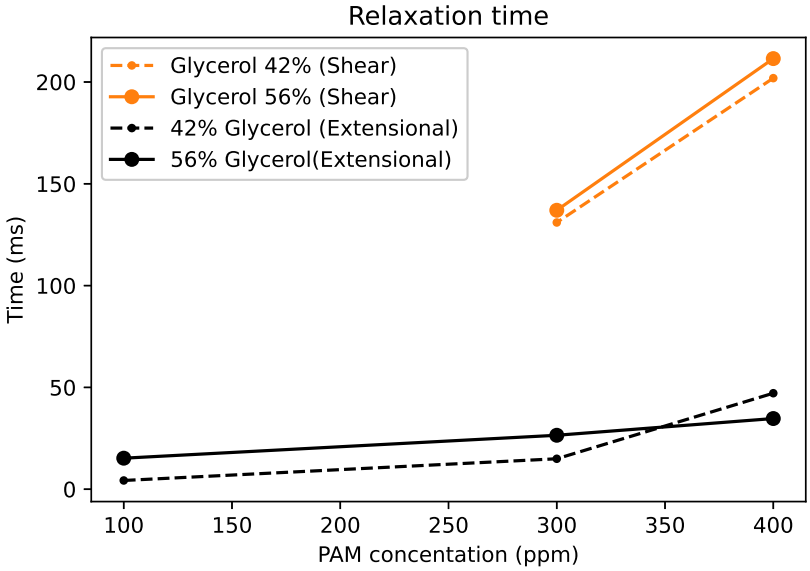

Figure 3.6: Shear and extensional relaxation time of Glycerol-Water-PAM solution with 1% NaCl at 20°C

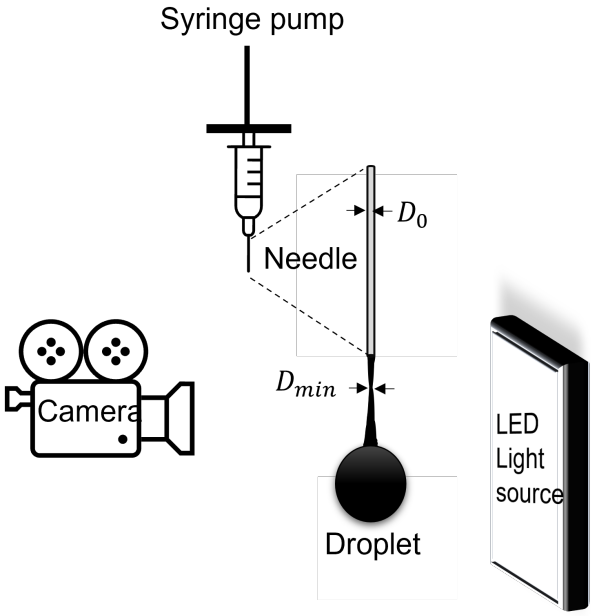

Figure 3.7: Experimental setup for pendant droplet - filament thinning experiment

3.2. Extensional Rheology

As we discussed previously, vortex shedding involves both shear and extensional relaxation behaviour. To identify the extensional relaxation time, we use a pendant droplet setup and allow the droplet to fall, resulting in thinning of the filament between the falling droplet and the liquid in the needle. For this purpose, an optical goniometer (used for contact angle measurements in droplets) was modified with a high frequency camera and brighter light source as shown in Figure3.7. The syringe pump was controlled using SCA-20 software, an LED light source was kept against the droplet and a *Photron-Nova-s12* camera (CMOS sensor) with a long-distance microscope (Navitar 2x - telecentric zoom system) was used to record images at 1000 Hz. The camera was controlled with PFV4 software and the calibration was carried out using the needle diameter ($\approx$ 0.51 mm, Magnification : 0.0096 mm/pixel), assuming no optical aberrations. The recorded images were further processed using a subpixel edge detection algorithm based on the partial area effect [160]. The evolution of filament thinning due to the falling droplet is shown in Figure3.8. The minimum diameter of the filament found using edge detection was fitted to equation 2.64 and extensional relaxation time was estimated.

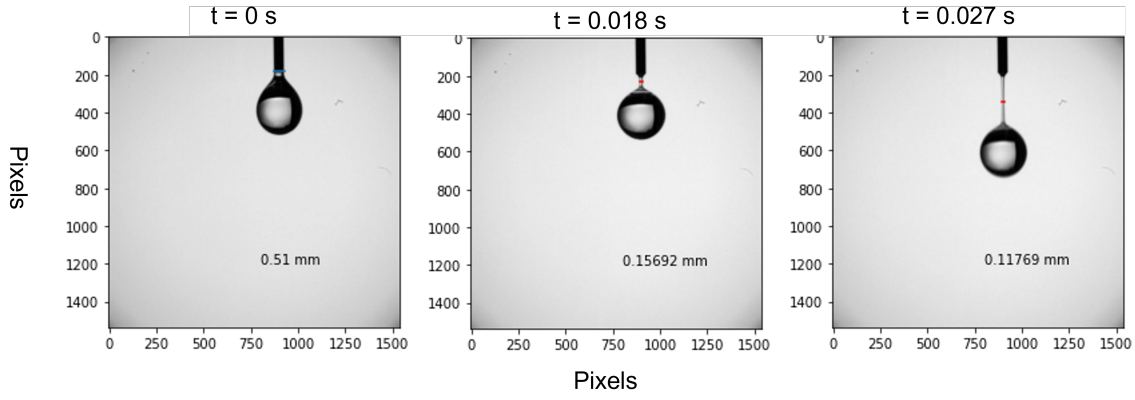

Figure 3.8: Evolution of filament thinning due to a falling droplet (56Wt% Glycerol, 300ppm PAM, 1% NaCl)

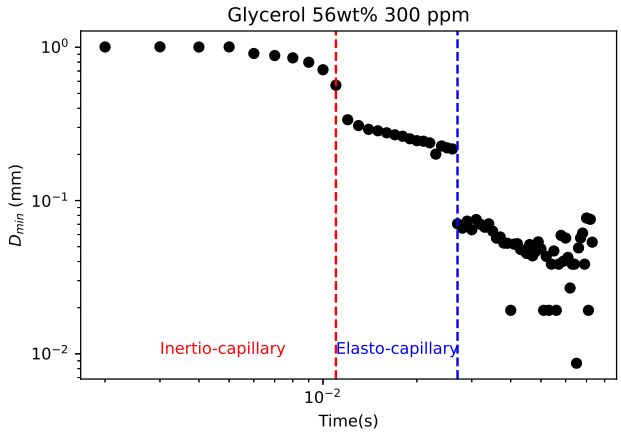

Figure 3.9: Filament thinning behaviour of 56Wt% Glycerol, 300ppm PAM, 1% NaCl

3.2.1. Extensional relaxation time

Initially, filament thinning is dominated by gravity-driven inertial force and capillary forces($Bo = \frac{\rho g R_{mid}^2}{\sigma_t} \leq 0.16$). Then, exists a region of exponential thinning dominated by elastic and capillary forces (with a polymer-chosen constant strain rate of $2/3\lambda$). The viscous forces are negligible, as discussed in Section 2.10.2. An example of a filament thinning graph is shown in Figure.3.9. The extensional relaxation time λ_e is determined with Oldryod-B model for extensional thinning in elasto-capillary regime and this procedure is repeated for other batches as in Figure.3.10. The extensional relaxation time λ_e for different PAM concentrations and Glycerol concentrations can be found in the Figure. 3.6. Now, compared to the shear relaxations in the same figure, it is notable that the extensional relaxation time scales are smaller than the shear relaxation time scales.This trend agrees with the data tabulated in the literature.

3.2.2. Choice of concentration

Ideally, we would choose a concentration within the overlap limit using simple equations as a function of polymer added viscosity, however in the presence of NaCl, such relations become invalid. Furthermore, our rheometer cannot measure zero shear viscosity due to high noise, preventing us from quantifying it. Therefore, based on the results of shear and extensional rheology, we empirically choose a PAM concentration of 300ppm (for experiments). We assume this is dilute, as we need to have sufficient relaxation time in a constant viscosity solution and also does not result in entanglement behaviours. This assumption can be further cross-checked in extensional filament thinning experiments, based on whether the elasto-capillary slope can be captured simply by using a single dominant relaxation time[161].

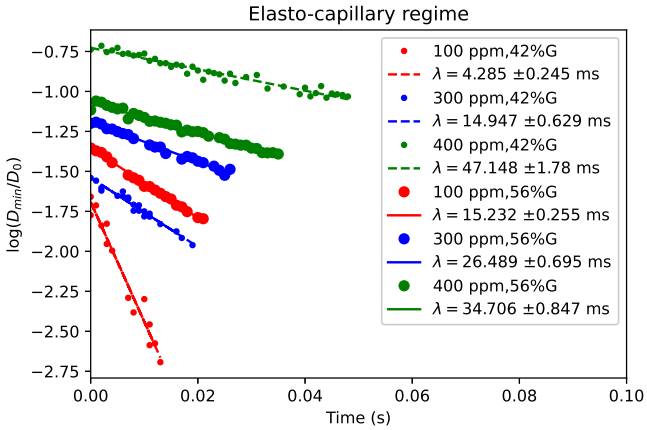

Figure 3.10: Oldroyd-B fit for filament thinning in elasto-capillary regime

3.3. Experimental setup

Since we are interested in an accelerating flat plate, we need an electro-mechanical system that provides translational motion and also controllable using a serial port. For this purpose, we use *IMS MDrive-17 plus* stepper motor with motion control driver with a resolution of 51200 steps/rev. This is attached to a linear traverse of 38 cm length, with a conversion factor of 2.54 mm/rev, resulting in a net resolution of approximately 4.9 μm/step. In this configuration, the maximum possible theoretical velocity is 0.177 m/s and an acceleration of 74.4 m/s^2. Once the traverse is ready for operation, we need the plate and tank that operate without any wall effects on fluid phenomena. Blockage ratio (BR) is a major parameter that affects the flow phenomena, and it can be defined as

$$BR = \frac{A_p}{A_t}$$

where A_p is the projected area of geometry and A_t is the cross-section area of test section.Theoretically blockage ratios anything above zero affect the flow in terms of pressure distribution, drag for any bluff body making it a confined flow. But in actual experiments that's not possible, so a blockage ratio < 6% is preferred[162]. Taking the lab space into account, we decided to use a normal flat plate with horizontal chord length of $30mm$, vertical span length of $60mm$ ($AR = 2$) and thickness of $3mm$; whereas the tank dimensions are $50cm(l) \times 13.5cm(b) \times 32cm(h)$. The fluid is filled to a height of $24cm$ leaving remaining height to avoid spilling of fluid, resulting in an effective $BR \approx 5.5\%$. The mid-span of plate was placed in the middle of the tank, with approximately equal heights from top and bottom interfaces. Furthermore, the initial position of the plate was placed $6cm$ from the wall to avoid wall effects, although the flow would not develop instantaneously. The structural element of the set-up was built using an X95 aluminum rail, while the plate and tank (thickness of 5 mm) were made using laser-cut acrylic sheets.

3.3.1. Force sensor

In order to measure forces, we use a YZC-131 1 kg load cell along with HX-711 amplifier controlled with Arduino Uno with an acquisition frequency of 80Hz (after lifting the ground connection of the RATE pin on HX-711 and connecting to the power input). A hollow stainless steel rod of length $25cm$, diameter $6mm$ and thickness $2.3mm$ was used to connect the flat plate to the force sensor, which was connected to traverse using a right-angled steel plate. After being connected to the plate, the force sensor was calibrated using four known weights, which were measured using a high-resolution weighing scale. The calibration graph of the force sensor is shown in Figure.3.11 and corresponding slope is 5.17×10^{-6} N per unit signal. Before the start of measurement, the force sensor was systematically given $20s$ to settle down the initial signal drift. Both the force measurements and PIV trigger were synced using the arduino digital output, while the linear traverse and arduino were both controlled using pySerial module of Python.

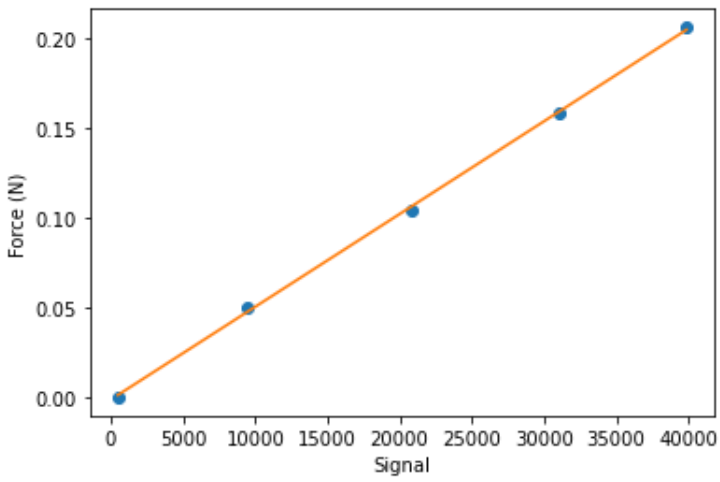

Figure 3.11: Force sensor calibration curve (dots: measured data, line: linear fit)

3.3.2. PIV setup

Once, the above steps were performed, PIV system was set up. Our PIV system consists of seeding particles, recording camera, $45°$ mirror, double pulsed Nd:YAG laser, Programmable Timing Unit (PTU) and DaVis 8.4 software as shown in Figure.3.13. The simplified setup schematic is shown in Figure.3.12b.

Field of View

We are interested in the vortex dynamics of the starting vortex at the mid-span, which would form by $T^* = 4$[23], however, to be safe with the design, we choose a field of length $T^* \approx 10$ corresponding to $30cm$. Assuming each side vortex reach a distance equal to one chord length from the plate tip eventually, we assume a Field of Width $3L_c \approx 9cm$. Thus, the choice for total Field of View is $30cm \times 9cm$

Camera

Although we are interested in large-scale vortex, we would look for a frequency of around $150Hz$ as a means of safely understanding the evolution of vortex by at least 100 frames within formation time, assuming a steady velocity (impulsively started) of 0.1 m/s. For this Field of View and frequency, we use LaVision Imager pro HS camera (CMOS sensor) with 2016 x 2016 pixels. Since, we are interested at the mid-span to avoid tip effects, our view should be from the bottom of the tank which means the lens should look upwards positioning the camera along vertical axis. However, this setup would be unsafe to camera due to potential spilling of liquid. Therefore, we use a $45°$ inclined mirror that projects the field of view to horizontally aligned camera. Now to achieve sufficient magnification, we chose Nikon-35mm lens by trial and error.

Seeding particles

It was estimated using literature [163] that the $50Wt\%$ Glycerol-water mixtures typically have a density of around $\rho \approx 1150kg/m^3$. Therefore, we use the available Sphericel 110-P8 hollow glass spheres as seeding particles due to a close density (to be nearly neutrally buoyant) of $\rho_p = 1100kg/m^3$ and mean diameter of $11.7\mu m$. The volume of particles was empirically chosen by slowly increasing the concentration and looking for sufficient particle concentration through DaVis window.

Illumination

The particles were illuminated using a Double-pulsed Nd-YAG laser (Quantronix, Darwin Duo) of wavelength $527nm$. When the trigger signal comes from PTU to Q-switch of the laser, the pulse is emitted and this is redirected to the mid-span axis by using two inclined mirrors (Thor labs). Once, the laser beam is in the proper axis, an optical setup of spherical lens (500mm) and cylindrical lens (-25mm) were used to convert the beam to laser sheet required for illuminating the Field of View. The camera and laser are connected to a PTU (LaVision), which is controlled using the computer through DaVis software. The signal for PTU comes from both DaVis and Python such that the camera, force sensor, linear traverse and laser are synced. A complete flow chart of the signal flow is illustrated in Figure3.12a.

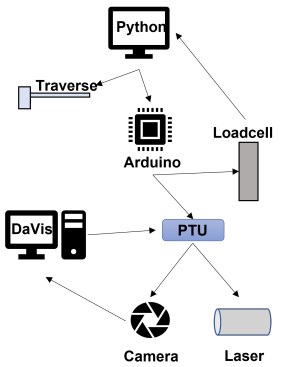

(a) Control configuration of PIV setup

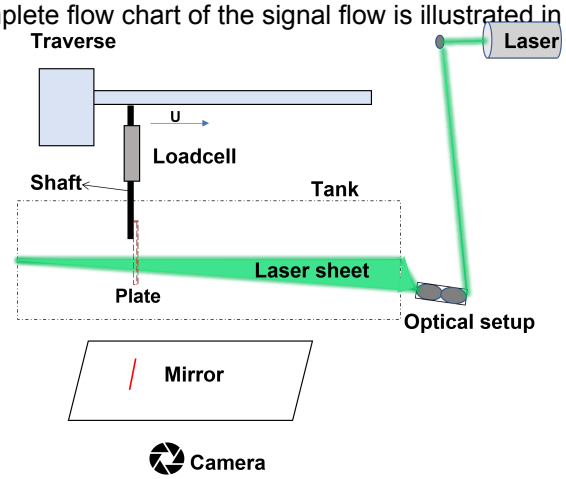

(b) A simplified diagram of the experimental setup

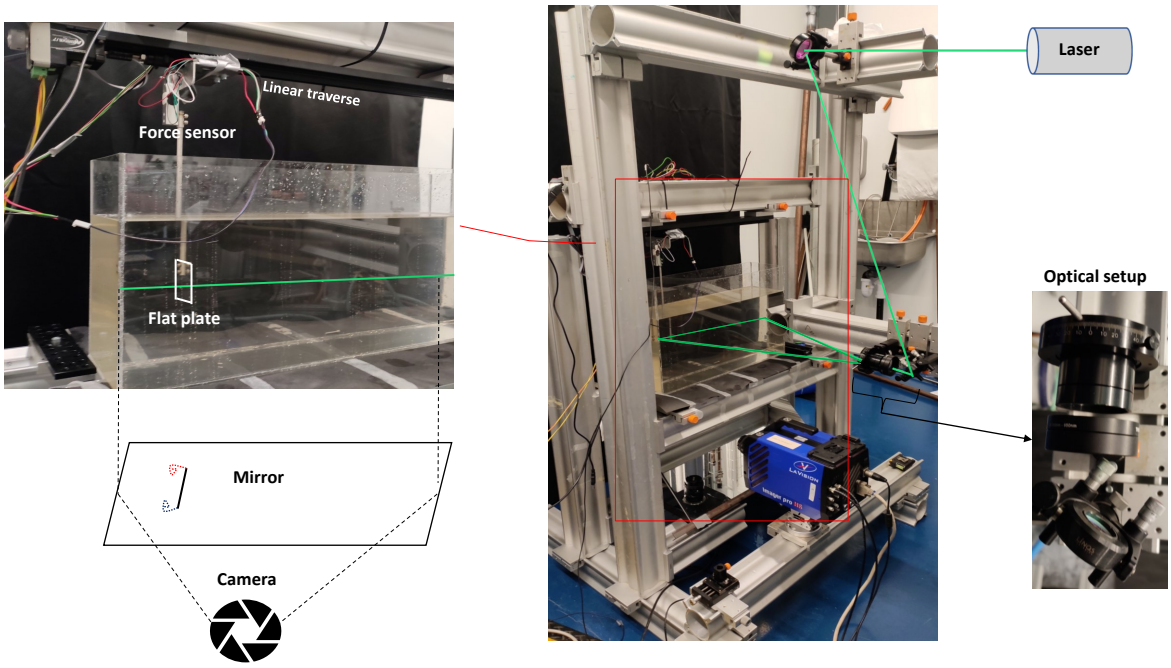

Figure 3.13: Experimental setup with PIV system

Calibration

When we record the images through camera, they are stored as pixels. In order to convert them to real world co-ordinates, calibration has to be done. For this purpose, we use dots of 3mm with 10mm from each other printed over a rectangular acrylic sheet ($47mm \times 10mm$). This is sheet is aligned in the Field of View , illuminated by a bright LED light source and the frames are captured. These images are processed in DaVis to make a 2D polynomial fit for converting pixel data to mm in the Field of View. The calibration target used for our experiments is shown in Figure.3.14.

Data acquisition settings

The recording parameters such as frame rate, exposure time and trigger control were specified using DaVis software. An external trigger was specified such that a digital signal from arduino would start the recording process, however 10 additional images before the trigger was included in order to account for any signal delay. The image frame rate was varied around 200-400Hz for different accelerations and terminal Reynolds numbers providing nearly 2000 images. These are further subsampled during post processing to provide approximately 300-400 frames for each experiment. The recordings were done in single frame-single exposure mode with an exposure time of 99 μs.

Processing

Once, we have the images, displacement vectors have to be found for estimating the velocity vectors. As a first step, we employ a geometric mask such that only the required Field of View is included for PIV processing. For estimating the displacement vector, we split the entire filed into small interrogation windows and look for how the particles of the same window have displaced between subsequent images. In each interrogation window, we look for high 2D cross correlation value between light intensity

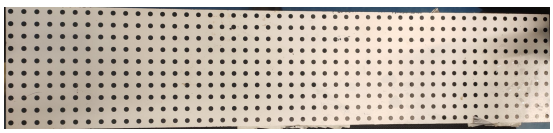

Figure 3.14: PIV calibration target

(scattered by particles) signals of subsequent frames, thereby estimating the directional displacement. The images were processed sequentially with 5 passes of cross-correlation , in which first 2 passes were of interrogation window 48×48 pixels and the last 3 passes were of 24×24 pixels with 50% overlap between adjacent interrogation windows. It is based on the idea that more passes would provide better accuracy and signal-noise ratio. Initially it applies the standard cross correlation to estimate the zeroth order displacement and using that vector, the interrogation window of second image is shifted/deformed to apply cross correlation again. Now, the first order displacement is estimated and by repeating this process, we can reach a higher orders of displacement at eventual iterations. Finally, total displacement is calculated as the sum of all orders of displacements in previous iterations . Pixel-locking is a major source of bias error in PIV as the size of pixels are sometimes smaller than or equal to particle image size resulting in correlation peak toward integer pixel values[164]. In this study, slight defocusing of objective lens to increase the particle image size was used as a mitigation strategy [165]. The size of particles were visually checked to be around 3-6 pixels to ensure that pixel-locking would not be a major source of error in our cases.

Vector-post processing

Once, the vectors are estimated, they are post processed in multiple steps such as deleting the vector if peak ratio is lesser than 1.1 (high noise), applying (3x) universal outlier detection based median filter (5x5 vectors) to remove vectors with residual (Velocity fluctuation normalized by, median of 8 neighbouring fluctuations lowest being 0.1pixel) greater than 2[166], choosing the second/third correlation peak if it agrees with median of neighbouring points and finally filling up the empty vectors by planar interpolation[164]. The increment in frames (net Δt) is chosen based on whether more than 95% vectors are of first choice with least frames,but resolved enough (1.95mm/vector) to capture vortex evolution.

3.4. Design of experiments

To understand the effect of viscoelasticity with respect to Newtonian, we need to perform experiments in both the identified viscoelastic fluid and viscosity-matched Newtonian fluid. Therefore, viscoelastic fluid of 56% Glycerol-water mixture, 300PAM and 0.5% NaCl of total volume $17.5L$ was prepared in the lab. Similarly, a viscosity matched fluid of 69% Glycerol-water mixture with same volume was also prepared for one-one comparison. It can be noticed that $0.5\%NaCl$ is used here, this is because we observed that the effect of more NaCl addition is negligible beyond a certain concentration. However, these fluids were prepared and characterized before the PIV experiments to measure viscosity ,density and relaxation time. The density of these fluids measured using Anton Paar DMA-5000 density meter were found to be $1146kg/m^3$ for viscoelastic solution and $1176kg/m^3$ for Newtonian solution. The mean viscosity (shear rates: 30-100 s^{-1}) and shear relaxation time were measured to be $\eta \approx 19.5mPa.s$ and $\lambda_s = 0.135s$ as discussed previously, the viscosity and frequency sweep plots are shown in Figure3.16. Since,the values are closer to the preliminary results, we will use the previously estimated extensional relaxation time for $1\%NaCl$, assuming similar flow behaviour.

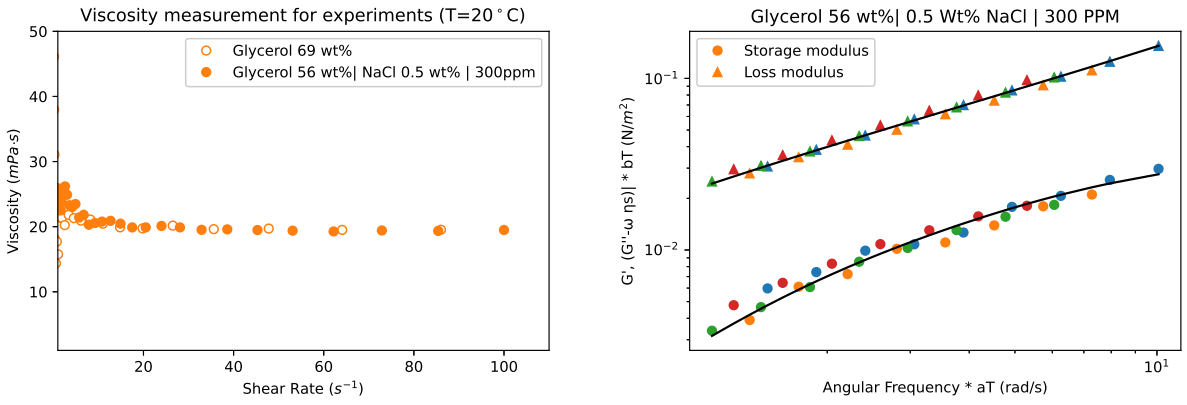

Figure 3.15: Viscosity measurement and Frequency sweep for fluids used in experiment

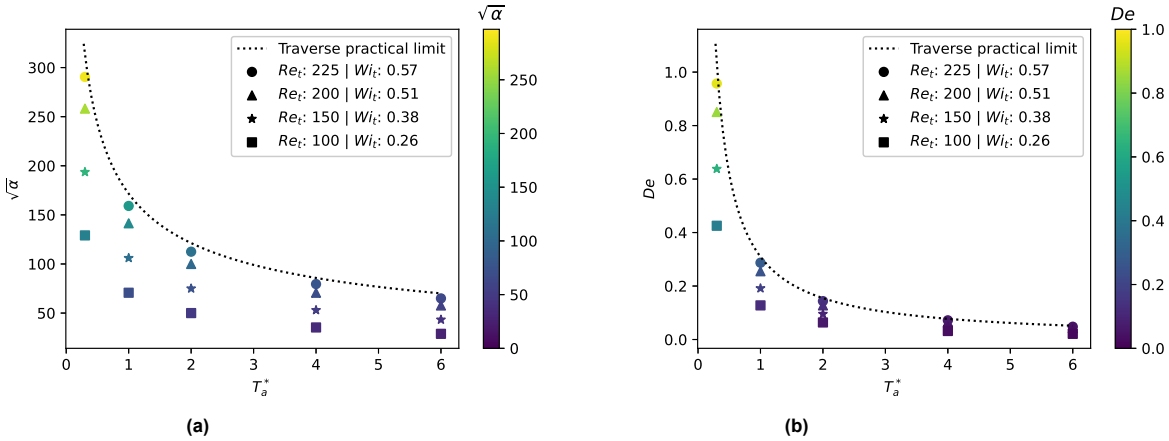

Figure 3.16: Design of experiments by changing Re_t and T_a^*, Wi_t applicable to viscoelastic cases

3.4.1. Parameter sweep

Once, the complete setup with the fluid was ready, the choice of parameters was decided. For these fluids, the maximum Re possible with our setup was found to be 225, although acceleration was not a limiting factor. Therefore, we vary the acceleration for a target terminal Reynolds number Re_t, by changing non-dimensional acceleration distance $T_a^* = S_a/L_c$ (S_a: Distance travelled), as acceleration is related to $Re(t)$ by $\sqrt{\alpha} = Re/\sqrt{2T^*}$. Then, each $\sqrt{\alpha}$ corresponds to an equivalent, De as shown in Figure.3.16b. The non-dimensional acceleration α, that we defined before, will be used with square root for ease of numerical representation. Viscosity ratio defined as $\beta_r = (\eta - \eta_{solvent})/\eta$ is another important parameter used to characterize a viscoelastic fluid apart from stress based non-dimensional numbers[90]. The Elasticity number, $\boldsymbol{El = 2.46 \times 10^{-3}}$ and viscosity ratio $\boldsymbol{\beta_r = 0.57}$ are kept constant in all our cases as the chord length and viscoelastic fluid were not changed.

Force measurements

Using T_a^* and Re, the experiments were designed as shown in Figure.3.16a and a Python notebook was prepared to automate the kinematics-Mcode conversion, Loadcell-Traverse-PIV communication, and data-storage such that the fluid choice, Re_t and T_a^* were the only inputs for each experiment. As we have previously mentioned, the plate is connected to the load cell using a hollow steel rod, which might contribute to both steady and unsteady forces. Therefore, a set of experiments were performed using a similar rod without the plate blinded section with respect to free stream (see Figure.3.17). The raw signals from the plateless case $F_{without\_plate}$, were subtracted from the flat plate case F_{with_plate}, to isolate the net forces acting on the flat plate F_{net_plate} . Finally, the force due to the remaining structural mass m_{rest} (plate+bolt+nut mass) was subtracted from the net plate force during acceleration $T^* = 0 - T_a^*$, to obtain the hydrodynamic forces (see Figure.3.17).The final results of the hydrodynamic forces acting on the plate will be used for further discussion.

$$
\begin{aligned}
F_{net\_plate} &= F_{with\_plate} - F_{without\_plate} \\
m_{rest} &= m_{with\_plate} - m_{without\_plate} \\
F_{hydrodynamic} &= F_{net\_plate}|_0^{T_a^*} - m_{rest}a
\end{aligned}
\tag{3.1}
$$

Figure 3.17: Rods with and without plate used for force measurements

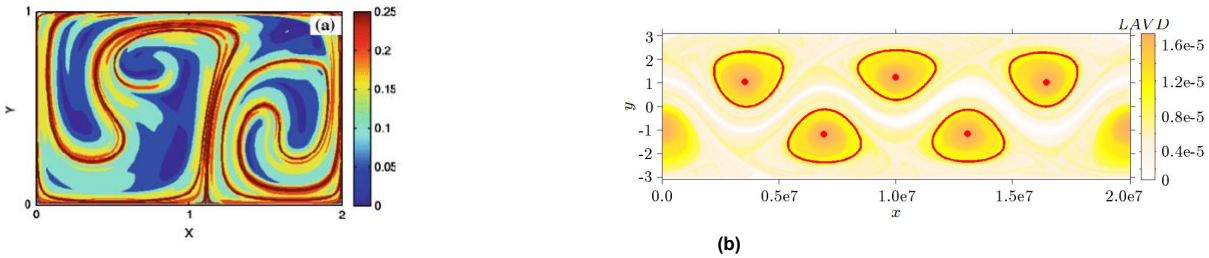

Figure 3.18: a)Positive FTLE field for double gyre at A=0.1,$\epsilon = 0.25$ taken from[169],b)LAVD field for bickley jet taken from [168]

3.5. Data analysis

After the experiments were done, velocity data has to be further processed in order to extract the coherent structures. For this purpose, we will be using FTLE fields, LAVD and Q-criterion. Therefore, it is first important to validate our codes for FTLE and LAVD with synthetic cases from literature. We use Double gyre [153] and Bickely jet [167] for FTLE and LAVD respectively, the functions can be found in the given references. These two are cases are used as a standard to compare different vortex detection methods throughout the literature [168].The standard results from literature are presented in Figure.3.18

3.5.1. Application of FTLE

The results from our FTLE code were qualitatively validated with literature (see Figure.3.18, Figure.3.19), whereas the choice of free parameters used for Double gyre are A=0.1, $\epsilon = 0.25$, step-size for numerical integration is 0.01s , 15s of integration length and 10s of advection period. The maxima normalized FTLE contour integrated in positive direction and the bidirectional ridges (defined here as highest quarter of FTLE values) are shown in Figure.3.19. In our experiments, we use minimum eigen values of hessian matrix and thresholding (typically >0.5-0.7 of extrema) to define these ridges. Sometimes, when the integration time is not enough to calculate thin ridges as in our cases, we end up with thick ridges. To resolve this issue , we use medial axis transform using Python's skeletonize algorithm (skimage package).

3.5.2. Application of LAVD

The Bickley jet parameters used were 62.44 m/s, L=1170km and r_0 as radius of earth (6371km) , whereas the center of the vortex cores were identified using maximum LAVD values and the boundary is defined as a closed contour boundary with maximum area. The boundary and centre of the vortices

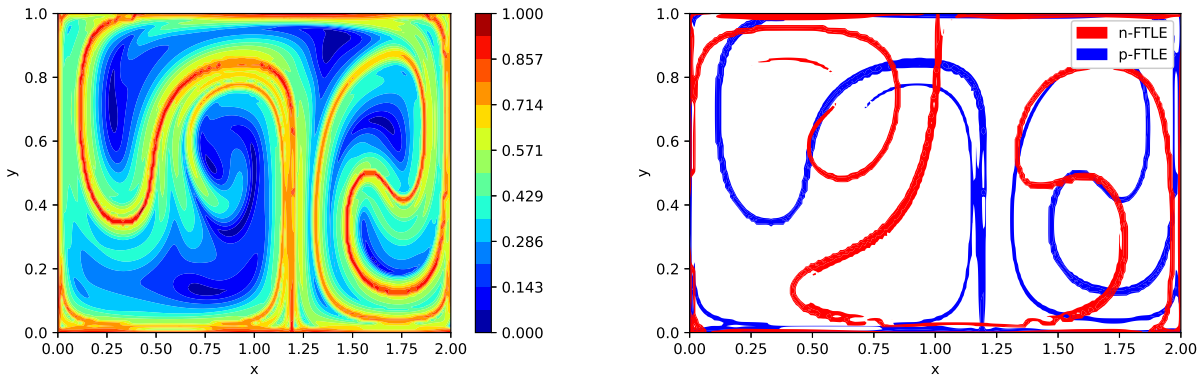

Figure 3.19: Maxima normalized positive FTLE field (left), positive and negative ridges defined by maxima normalized FTLE values of 0.75 (right)

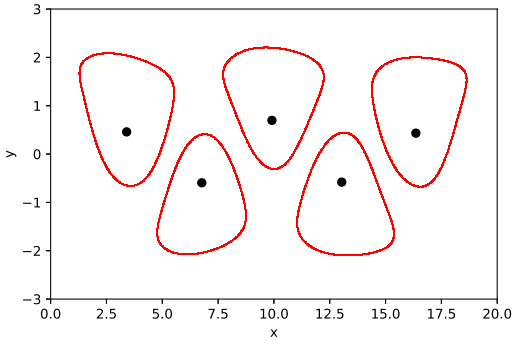

(a) Centre of vortices marked by dots and the red contour marks the boundary defined using LAVD

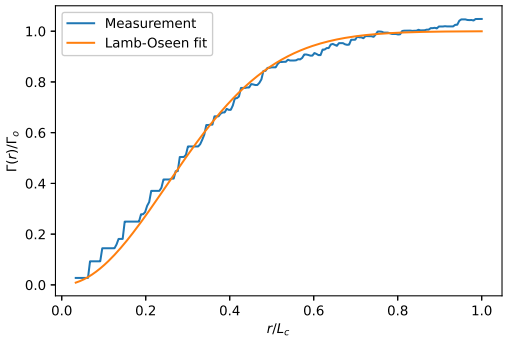

(b) An example Lamb-Oseen fit from $\sqrt{\alpha} = 290.47, Re_t = 225$; r is the radial distance, Γ_0 is total vortex circulation

Figure 3.20

identified using LAVD is shown in Figure.3.20a (compared to Figure.3.18). Although LAVD is widely used for vortex detection and tracking, it uses angular displacement over an integration time and this eventually gives a structure that was coherent throughout that period. Then LAVD maxima is chosen as the centre, and boundaries are detected based on convexity deficiency and closed contour with maximum area surrounding the centre. Convexity deficiency is the deviation from its convex hull, which is defined as the smallest convex polygon having all points inside or at boundary. This approach although provides a robust approach for material coherence, a starting vortex is entraining and detraining the mass over its formation [168] which we are interested in. Therefore, the direct application of LAVD in this study will be limited to detecting a formed vortex (defined based on FTLE-saddle point velocity) and advecting the fluid parcels inside to see how they evolve over time.

3.5.3. Frame transformation

As a first step before any analysis, we transform the laboratory frame into plate frame by subtracting the plate translational x-velocity u_p from x-component of fluid velocity u and tracking the plate with a fixed frame of $3.5L_c$ with plate centre as the origin.This simplifies the analysis as if it is a flow past a flat plate and this difference can be clearly seen in streamlines as it is frame dependent[17]. For a few initial frames, we use ghost cell padding of free stream velocity to achieve this. An example case of streamlines before and after transformation is shown in Figure.3.21. Note that all T^* values provided in the title are with respect to lab-frame and in the axis are with respect to plate-frame.

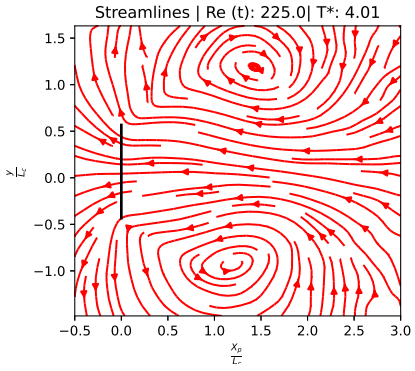

(a) Lab-frame

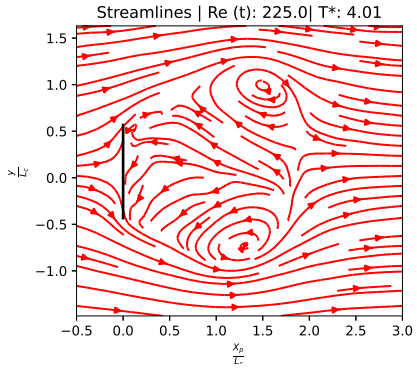

(b) Plate-frame

Figure 3.21: Frame dependent streamlines for $\sqrt{\alpha} = 290.47$, Re_t=225

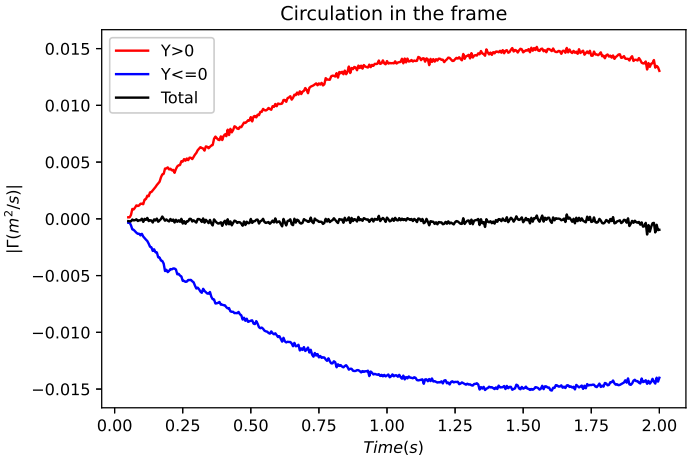

Figure 3.22: Circulation in frame for $\sqrt{\alpha} = 290.47$, Re_t=225

3.5.4. Analysis limit

Since, we are using a 2D-2C PIV data, we do not want out of plane flow features to be present. Therefore, to cross-check we invoke Kelvin's circulation theorem for inviscid fluid, assuming the viscous dissipation rate is small relative to inertial effects in a forming vortex. By conservation of circulation, the total circulation should remain zero for negligible viscous dissipation and without, out of plane flow features. So, we first split the domain into upper half and lower half to look at total positive and negative circulation in the domain. We also look at the net circulation to choose the frame limit of our analysis (Typically $T^* = 8$) *to make sure we do not have any third dimensional structure in the system*. An example of total circulation in domain is shown in Figure.3.22. In all our cases, circulation is calculated as a surface integral of vorticity. Although, the acceleration distances T_a^* can be much smaller, we analyse the whole evolution process of a starting vortex.

3.5.5. Vortex detection method-1

The first method that we tried was simply to use same conditions of vortex boundary detection in a LAVD field, but we use it over +Q criterion and centroid of this boundary is used to detect vortex location. This method suffers from a disadvantage that the convexity deficiency is given as a user input and it continuously varies for a forming vortex. Although, we extracted some results with this approach, they were found to be highly sensitive to the shape of the chosen boundary and convexity deficiency. Nevertheless, this method helps us in understanding the aspect ratio ($AR_v = x_{max}/y_{max}$) of the vortex to a reasonable extent as the boundary is defined, and these definitions does not seem to affect the aspect ratio. In this study, we will use this method only to define the aspect ratio.

3.5.6. Vortex detection method-2

The second method that we employed is to utilize the saddle point. The intersecting point of forward integrated FTLE and backward integrated FTLE is called a saddle point.It can be seen that the positive and negative FTLE ridges form a closed region around a vortex (see Figure.4.7c), signifying the dynamical distinction. Therefore, we utilize the saddle point location to detect the horizontal boundary of this distinct region and plate centre for the vertical boundary, since we have symmetrical vortices. Although this detected region is dynamically distinct, it does not mean a vortex, as it also includes a high shear region inside this region (see section 2.13.2). We cross verified this by applying the Q-criterion and observed that it had regions of both rotational and shear dominance. Therefore, we use the Q-criterion with Q>0 to isolate regions of rotational dominance to detect the vortex, and this approach is found to work well even for a filamented forming vortex. An example of aforementioned methods in plate frame of reference are shown in Figure.3.23. Note that in this study, we will analyse only the Y+ side vortex assuming symmetry.

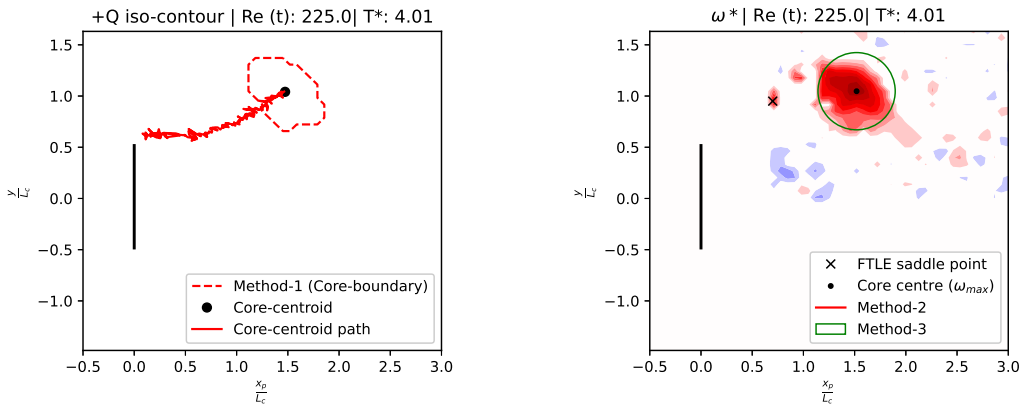

(a) Vortex detection method-1

(b) Vortex detection method-2,3

Figure 3.23: Vortex detection methods based on Q-criterion vortex boundary and saddle bounded Q-criterion for $\sqrt{\alpha} \approx 290.47$

3.5.7. Vortex detection method-3

Although vortex detection by using method-2 gives the circulation similar to method-3 (see Figure.3.24), it results in large noise when we calculate kinetic energy, for example. The reason behind this is that the vorticity is highly concentrated in the vortex core, and it is expected to be negligible outside the vortex core. Therefore, circulation calculation based on vorticity is less noisy, however this logic does not apply to kinetic energy, as regions outside the vortex core also has their own kinetic energy. To avoid this, we fit the Lamb-Oseen model (Equation.2.7) after applying method-2 to extract the equivalent ideal vortex diameter d_v, we use d_v and the aspect ratio from method-1 to further constrain the region to reduce the free stream noise. Note that we do not apply this for slowly accelerated cases, as the vortex forms much later and free stream noise using method-2 is negligible there. Thus, vortex region is separated without contours and an example of Lamb-Oseen fit is shown in Figure.3.20b.

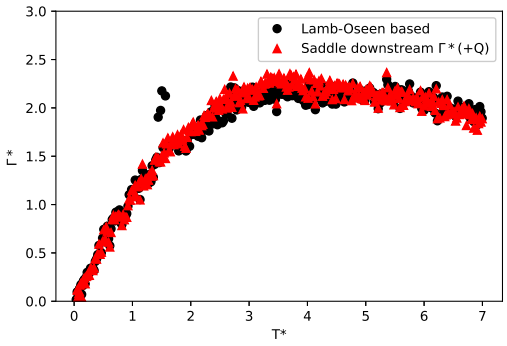

Figure 3.24: Comparison of circulation calculated by Method-3 and Lamb-oseen fit shows that circulation calculation is unaffected by remaining noise

4

Results & Discussion

Now that we have the experimental data, let's revisit our research questions.

- How does viscoelasticity and acceleration affect ***vortex dynamics*** in a starting plate?
- How are ***forces*** affected by the presence of elastic forces and acceleration?

Understanding vortex dynamics will eventually help us to understand the changes in forces, therefore first we look at the vortex dynamics from the PIV data, followed by force measurements.

4.1. Vortex dynamics

In order to understand the basic difference in vortex dynamics due to acceleration, we analyse the vorticity field in Newtonian fluid. Then we look for comparative (Newtonian vs Viscoelastic) details during the evolution of vortex ring using FTLE saddle points, LAVD, vortex core circulation, vortex ring energy, vortex ring/core size, and vortex velocity. Furthermore, to simplify, we will present results only $Re_t : 225, 150$ (refer Figure.3.16a) to also represent differences due to Wi_t or Re_t .

4.1.1. Vorticity field

High acceleration cases

Among the Newtonian cases, we choose two accelerations, representing higher acceleration $T_a^* = 0.3$ and lower acceleration $T_a^* = 4$ (refer Figure.3.16a). Since, the vortex has to be formed by $T^* = 4$ according to universal vortex formation distance, let's examine the vorticity field with $T^* = 4$. Note that we use non-dimensional vorticity, defined as $\omega^* = \omega L_c / U_p$ in the following figures. From Figure.4.1, it can be observed that as Re_t increases, the vortex core is more tightly pronounced in impulsively started cases ($T_a^* = 0.3$).Although the accelerations are different, we see Re_t as the affecting parameter of core size, since the acceleration distance/time is extremely small.At high accelerations, the vortex rolls up and eventually pinches off, after a certain point, as reported in literature.

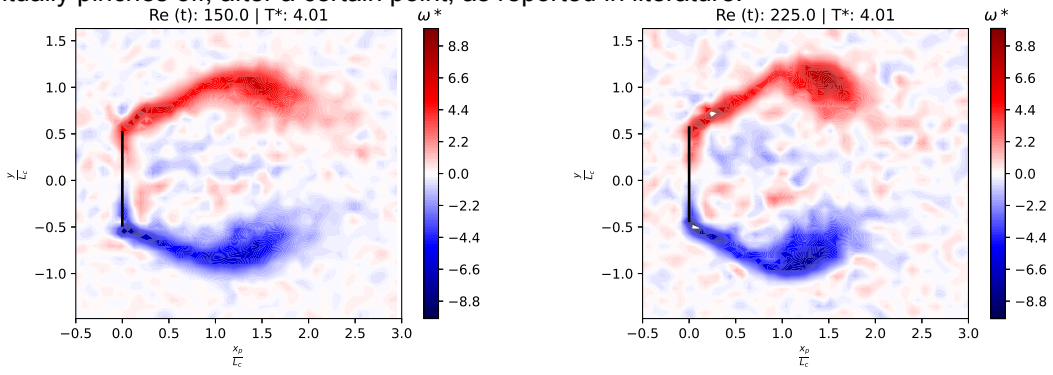

(a) $\sqrt{\alpha}$=193.65 **(b)** $\sqrt{\alpha}$=290.47

Figure 4.1: $Re_t = 150, 225$ at $T^* = 4$ representing impulsively started cases with $T_a^* = 0.3$

Low acceleration cases

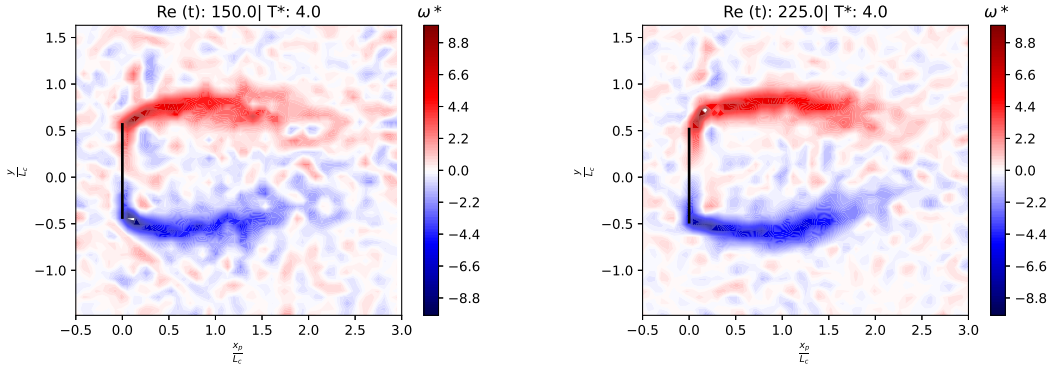

(a) $\sqrt{\alpha}$=53.03 **(b)** $\sqrt{\alpha}$=79.54

Figure 4.2: $Re_t = 150, 225$ at $T^* = 4$ representing slowly started cases with $T_a^* = 4$

On the otherhand, the lower acceleration cases in Figure.4.2 seems to be having a region of shear without rolling up, although the Re has reached the same as high acceleration cases. To cross verify this, let's take a closed contour of a completely formed structure using LAVD and advect those fluid parcels backwards to see the type of motion they experience. In Figure.4.3, we choose the fluid parcels (black dots) inside closed contour at $T^* > 6$, one representing high acceleration cases ($T_a^* = 0.3$) and another representing low acceleration cases ($T_a^* = 4$). The idea behind choosing $T^* > 6$ is to have a closely common dimensionless-timescale where coherent closed contours can be observed. Now, we advect the chosen fluid parcels (black dots) backward in time $T^* = 4$ (white dots) to see how they have evolved over time in a Lagrangian frame. It can be observed from Figure.4.3 that at high accelerations the separated fluid parcels undergoes a spiralling motion at a few chord lengths, but the slowly accelerated fluid parcel seem to extend downstream as a thick sheet which we can think of as an unrolled separated shear layer.

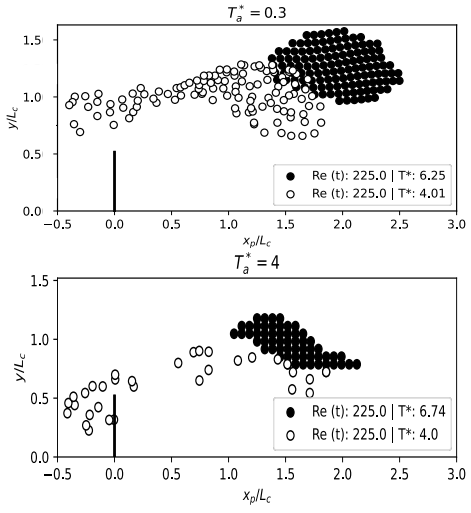

Figure 4.3: Comparing evolution of coherent fluid parcels using LAVD backward advection (Newtonian)

Unusual vortex formation

Do these slowly accelerated cases ever roll up? They do, but in an interestingly different manner. At a longer time, we observe a kink in this shear layer around one chord distance downstream the plate. The kink eventually breaks one side of the shear region, to rollup into a vortex, as shown in Figure.4.4. Now, to understand the reason behind this unusual rollup and overall effect of viscoelasticity in parameter space, let's distinguish the process of vortex shedding into boundary layer separation, shear layer roll-up, vortex formation and Pinch-off as discussed earlier [33].

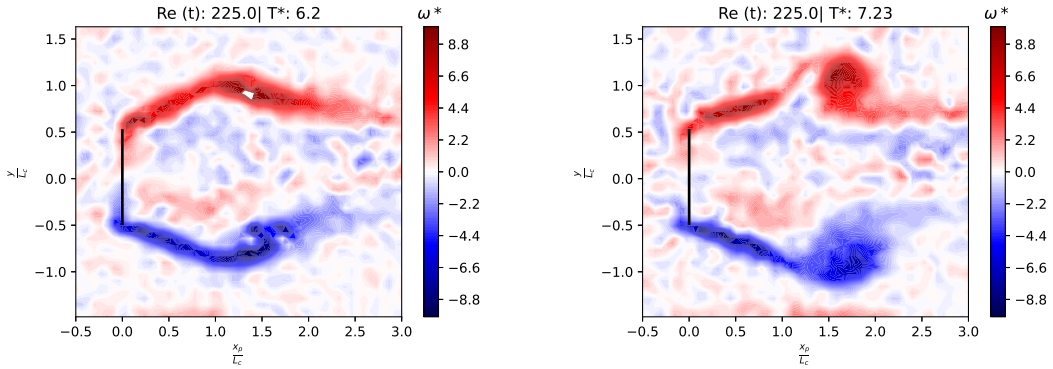

(a) $\sqrt{\alpha}$=79.54 **(b)** $\sqrt{\alpha}$=79.54

Figure 4.4: Vortex pinch-off for $Re_t = 225$ representing slowly started cases with $T_a^* = 4$

4.1.2. Boundary layer separation

As discussed in section 2.2.1, we use equation 2.12 to estimate the thickness of the boundary layer in the stagnation region before separation, as this eventually affects the strength of the shear layer formed after separation, further affecting the core formation at $T^* < 1$[24]. The boundary layer thickness in the stagnation region, assuming quasi-steadiness, is shown in Figure.4.5. It shows that the boundary layer thickness at such lower acceleration is much larger due to smaller instantaneous $Re(t)$, therefore we would expect a weaker shear layer due to smaller gradient in lower accelerations. We can also quantitatively verify this by looking at the instantaneous circulation of the vortex, as in the following section.

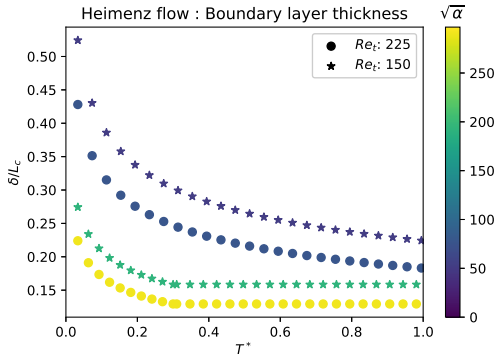

Figure 4.5: Analytical quasi-steady estimation of stagnation boundary layer thickness (δ)

4.1.3. Shear-layer rollup

By comparing the circulation (Method-2) based $Re_\Gamma = \Gamma/\nu$ [24] in the Figure.4.6, it can be noted that the lower acceleration cases ($T_a^* = 4$) have relatively smaller Re_Γ at $T^* < 1$ than impulsively accelerated cases ($T_a^* = 0.3$). It means that the low acceleration cases are much more dominated by viscous forces, unlike the impulsively accelerated cases. The circulation data was filtered using linear Savitzky-Golay filter (9 points average : empirical choice).

Induced motion

According Birkoff-Rott equation for a vortex sheet[18], fluid parcels in a shear layer (assuming it as a vortex sheet) would induce a motion on other parcels and the sheet itself to roll up. This induced velocity is proportional to strength of the vortex sheet , which is equal to circulation gradient along the sheet thickness[17]. We suspect that a weak (small circulation gradient due to viscous effects) separated shear layer is not able to roll up in such lower accelerations. An existing literature[170] has also reported that viscosity was found to weaken the vortex sheet rollup process. Though this provides

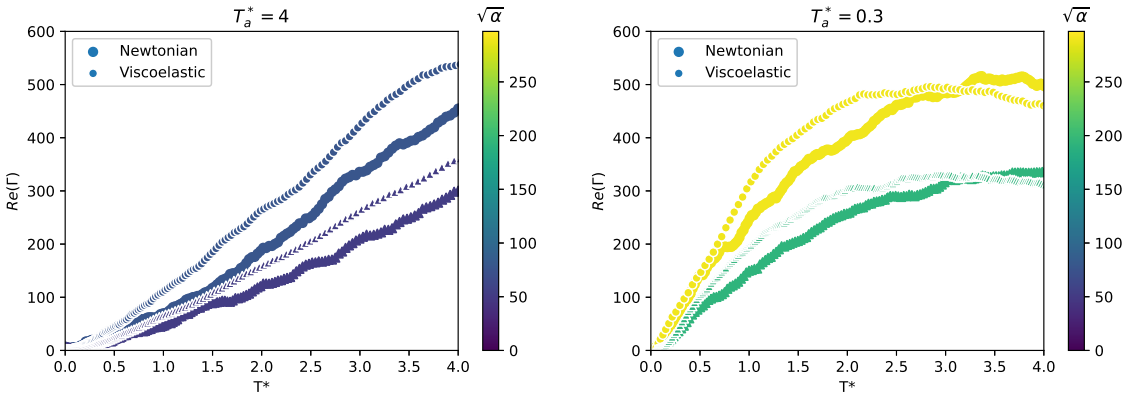

Figure 4.6: Comparing (upper) vortex Re(Γ), the viscoelastic cases have steeper slope than Newtonian case

some insight on why it has not rolled up at usual rollup distances, the rest of question remains, why don't these cases roll up even when Re_Γ reach large enough? We believe this could be an effect of growing shear layer. Although shear layer growth results in growth of circulation, it may not necessarily substantially increase the gradient of circulation as the shear layer size also grows over time.

Effect of viscoelasticity

Now comparing viscoelastic effects with respect to Newtonian in Figure.4.6, the Re_Γ seem to be larger in viscoelastic cases with more elastic stress (Wi) compared to their Newtonian counterparts. However, this difference is observed to be slightly larger in the lower acceleration cases. We hypothesize that this behaviour is because of the elastic nature of the polymers dissolved, as they tend to pull neighbouring fluid parcels along (similar to the filament between droplet and needle) when circulation is imparted to a fluid parcel during entrainment around the boundary of these coherent structures (shear layer/ vortex).

4.1.4. Vortex formation

FTLE saddle position

As we discussed earlier, FTLE saddle points can be used to detect the formation distance of a vortex core. However, in our case the integration time is unfortunately not enough for calculating thin ridges to extract those saddle points directly. Therefore, we apply medial axis transform to thin the ridges and identify the forward and backward FTLE intersection points. These points are tracked using a combination of nearest neighbour algorithm and visual inspection. An example of identified saddle point placed over the FTLE ridges is shown in Figure.4.7c and their change in saddle point position with respect to plate (x_p) is shown in Figure.4.7. In high acceleration cases ($T_a^* = 0.3, 1$: Figure. 4.7a) irrespective of Re, the saddle points start moving away from the plate around the same T^* (We define this as the FTLE based formation time T_f), whereas in slower acceleration cases ($T_a^* = 4$: Figure. 4.7b) the saddle point moves relatively much later, with a steep slope for rollup and inclined slope after formation. Furthermore, in Figure. 4.7a, we can also observe that the viscoelastic cases in high accelerations seem to have an equivalent slope (marked by black dotted line) to Newtonian cases, but with earlier saddle point inflection.

FTLE based formation time

We perform a linear fit for saddle point positions to properly measure the points of inflection, and the results are shown in Figure 4.7d. It was found that the mean formation distance in high acceleration Newtonian cases was $T_f = 2.7$ with a standard deviation of 0.13 and corresponding viscoelastic cases have $T_f = 2.3$ with a standard deviation of 0.06. This Newtonian formation time agrees closely with the experimental observations $T_f \approx 2.5$ of [25] with AR=2 but high Re. The only exception case where both were matching was T^a=1, Re_t:150 was found to be off from men values in viscoelastic case. The overall trend in both Newtonian and viscoelastic cases shows that, for cases with acceleration higher than a critical value, the formation distance is constant, as we would expect from the optimal vortex formation theory. We define this critical acceleration as the optimal vortex formation limit, as the cases below

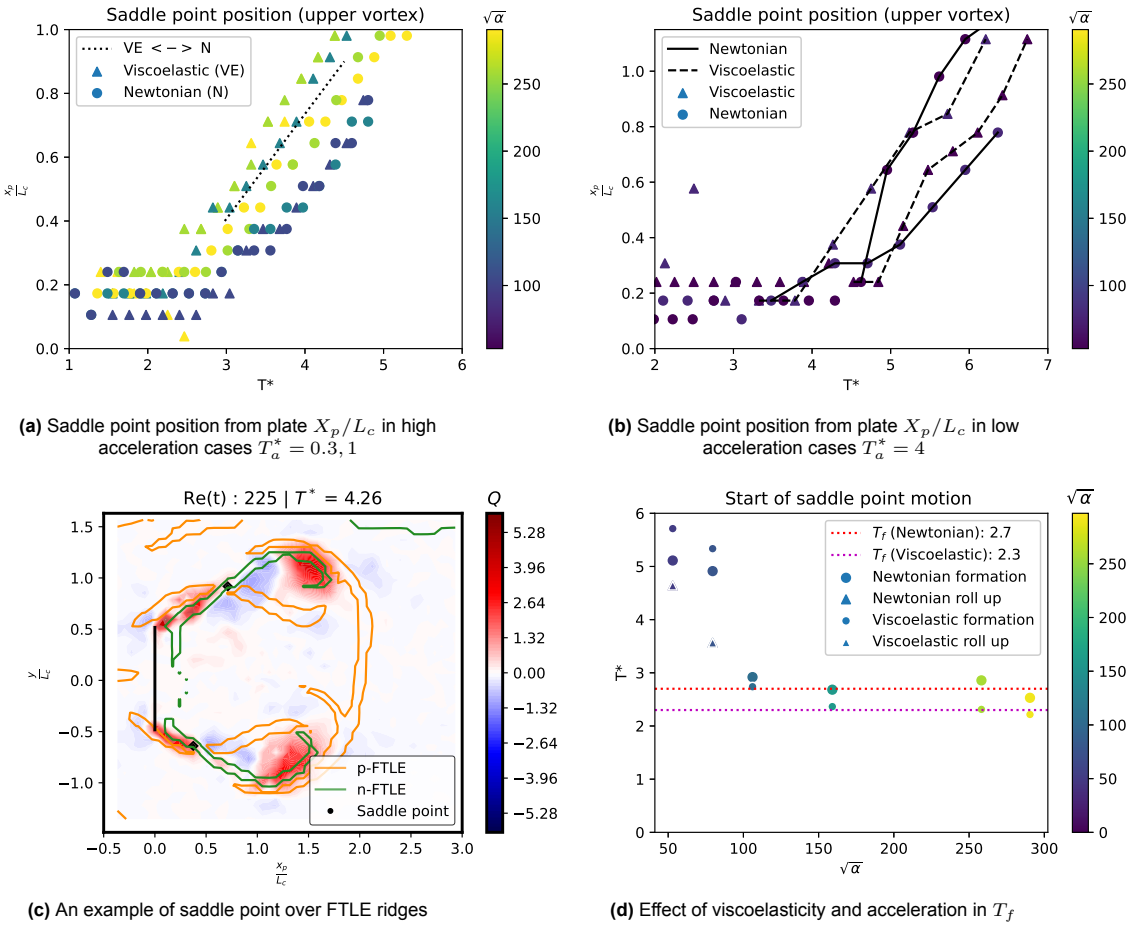

(a) Saddle point position from plate X_p/L_c in high acceleration cases $T_a^* = 0.3, 1$

(b) Saddle point position from plate X_p/L_c in low acceleration cases $T_a^* = 4$

(c) An example of saddle point over FTLE ridges

(d) Effect of viscoelasticity and acceleration in T_f

Figure 4.7

this acceleration has varying formation distances larger than the constant values for high acceleration cases. From Figure.4.7d, we can identify that the limit of optimal vortex formation is $\sqrt{\alpha} \approx 75 - 80$. These results for high acceleration cases can be explained by the Figure 4.6 as more the circulation in viscoelastic cases sooner the formation, whereas for lower accelerations, although the circulation is higher in viscoelastic cases, the roll up process from a shear layer seem to be delayed in the presence of viscoelasticity. It is also interesting to note that viscoelastic effects on formation does not seem too sensitive to Wi_t in our range $0.38 - 0.57$ as long as it is above the optimal vortex formation limit for acceleration (see Figure.4.7d, Figure.3.16a).

Non-dimensional energy E^*

Kelvin-Benjamin variational principle has been widely used to explain the vortex formation distances, as we discussed in section 2.2.2. According to Kelvin-Benjamin variational principle, "A state of steady vorticity distribution (interpreted in literature as vortex ring) maximizes the total kinetic energy, under the constraint: hydrodynamic impulse is constant with respect to disturbances that preserve the circulation of each fluid element[171, 172]". In other words, it has been explained that the vortex would no longer take in any more vorticity when $E_{vortex-ring} \geq E_{generator}$[26]. In the previous studies, a non-dimensional energy E^* is used to characterize this formation and $E^* \approx$ 0.27-0.34 has been found to be the limiting value for both propulsive and drag vortex to completely form [24, 37]. A smaller value of E^* represents a region of vorticity that is well distributed with large energy, whereas a larger E^* during roll-up would imply a smaller concentrated region of vorticity. Therefore, a fully formed vortex ring is expected to have the minima compared to earlier stages of formation. Note that in this section, Y-coordinate is represented as r as stream functions are calculated in radial co-ordinates with plate centre as the origin. The non-dimensional energy E^* represents the distribution of vorticity in a vortex core, and it

can be defined for an axisymmetric vortex ring as[24],

$$E^* = \frac{E_v}{\sqrt{\mathbf{I}\Gamma^3}} \tag{4.1}$$

$$E_v = \pi \iint_{core} \Psi\omega \; dxdr, \quad \mathbf{I} = \pi \iint_{core} \omega r^2 dxdr$$

where E_v is the vorticity based kinetic energy, I is the hydrodynamic impulse of the vortex, Γ is the circulation of the vortex, Ψ is the stream function. A statistical way of interpreting E^* as vorticity distribution was given by the relation [24], $2.3E^* + 0.5 = std(\omega_{core})/\overline{\omega_{core}}$; where $std(\omega_{core})$ is the standard deviation of core vorticity and $\overline{\omega_{core}}$ is mean of core vorticity. We perform the analysis of E^* to explain the formation process in our cases assuming an equivalent axisymmetric vortex ring, although in reality is an elliptical vortex ring. The Stokes stream function is calculated by solving[173],

$$(\frac{\partial^2}{\partial x^2} + \frac{\partial^2}{\partial r^2} - \frac{\partial}{r\partial r})\Psi = -r\omega \tag{4.2}$$

A central difference based sparse matrix solved by assuming the far field boundary condition of $\Psi_{boundary} = 0$ [174] and $\frac{1}{r} \ll \frac{\partial}{\partial r}$ far from origin. This formulation highly depends on ω as stream function is also calculated using ω as the source term. Thus, regions of high vorticity (core region) would dominate the energy calculation.

E^* based formation time

When applied to our high acceleration cases, we found that the E^* value was reaching a constant of $\approx 0.2 - 0.3$ only by about $T^* \approx 4$ in both Newtonian and Viscoelastic cases, as shown in Figure.4.8. However, in slower acceleration cases, it reaches ≈ 0.4 in both viscoelastic and Newtonian cases at $T^* \approx 4$ (see Figure.4.8), which is closer to the initial movement of saddle points indicating vortex rollup from a shear layer as shown in Figure.4.7d. Thus, we can say that rollup in lower acceleration cases is driven by its need to pinch-off as a consequence of Kelvin-Benjamin variational principle unlike high acceleration cases where the roll up is due to induced velocity, occurring much earlier $T^* < 1$ than pinch-off time. Furthermore, higher $E^* \approx 0.4$ in low acceleration cases compared to high acceleration shows that the rolling up filamented-vortex has vortex core less widely distributed than a fully formed vortex. In viscoelastic cases, minimum E^* is slightly smaller, indicating that vortex core is more distributed. On a larger picture, we can say that there is no significant difference between Newtonian and Viscoelastic cases on formation time of high acceleration cases. The plateau of, E^* after reaching the minima, shows that the vorticity distribution no longer changes in the vortex ring, indicating a steady vortex ring. Thus, we find that the E^* minima occurs around, $T^* \approx 4$ and this compares well with the universal vortex formation time reported in literature [37].

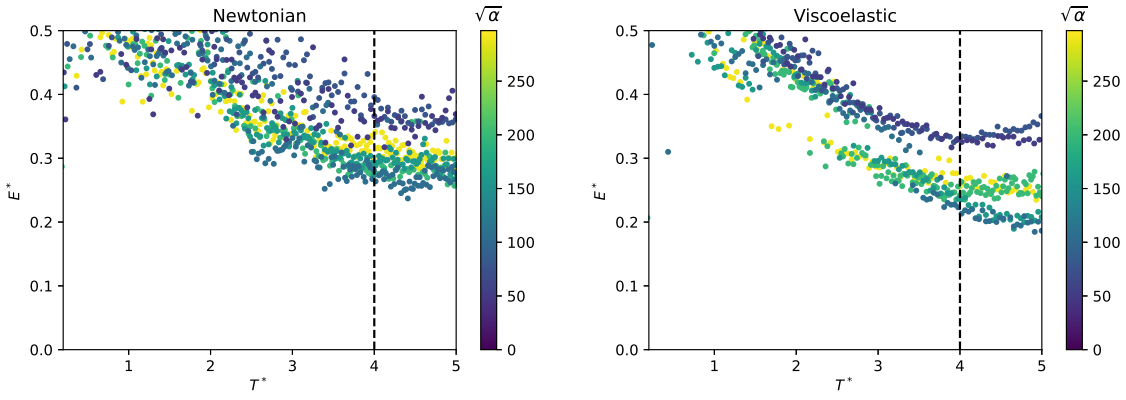

(a) Non-dimensional energy E^* vs T^* in Newtonian cases

(b) Non-dimensional energy E^* vs T^* in Viscoelastic cases

Figure 4.8

Kinetic Energy of vortex core

Although, E^*_{min} at $T^* \approx 4$ is inline with universal formation distance, it is unclear why FTLE saddle moves around $T^* \approx 2.3 - 2.7$.For this purpose, we use our vortex detection method (method-3 : high acceleration, method-2 low acceleration) to extract one core region. Now assuming zero third dimensional velocity component, we calculate the conventional kinetic energy per unit span defined as ,

$$E_{core} = \frac{1}{2}\rho \iint_{core} (u^2 + v^2) dA \tag{4.3}$$

We normalize E_{core} using energy per unit span supplied by the plate defined as[18],

$$E_{plate} = \frac{1}{2}\rho u^2_{plate}(\frac{\pi}{4}L_c^2) \tag{4.4}$$

Interestingly, we found that this ratio $2E_{core}/E_{plate}$, (factor 2 accounting for the two vortex cores) reaches ≈ 1 (see Figure.4.9a) around same T_f , as measured using FTLE saddle point (see Figure. 4.7d). However, in Figure. 4.7d, we note that viscoelastic cases with very low accelerations have higher peak values, which we think is due to noise around the vortex as method-3 could not be applied for an unrolled up case. In general, this formulation based on $E_{vortex-ring} \geq E_{generator}$[26] explains that the energy is no longer supplied from plate after T_f (from FTLE saddle points). Usually both of these energy formulations are considered equal and expected to provide same results, but interestingly they seem to capture different things of the same process.

Difference in two formulations

So, what is the difference between these two formulations? E_{core} can be written as a sum of E_v and a surface integral term that is assumed to be zero for unbounded flows[18]. Let's recall that E^* signifies the distribution of vorticity in a vortex core. Since the filamented structures outside the core were captured in method-2, we looked at the corresponding vorticity contour. We found that there was a filamented +Q tail, connecting vortex and -Q region when the FTLE saddle started moving at $T^* < 3$ and it completely rolls up to become a part of vortex at $T^* \approx 4$. So, the filament of vorticity rolling up to become a part of the vortex explains why the E^* minimum is seen at $T^* = 4$, even though the whole structure had reached its kinetic energy maximum at $T^* \approx 2.7$. Furthermore, looking at Γ as $Re(\Gamma)$ of $T^*_a = 0.3$ in Figure.4.10a, it is clear that the circulation has reached closer to its maximum at $T^* < 3$, although a slight increase is found later. This slight increase could be potentially due to filament rolling up. This tells us that the majority of vorticity addition to the vortex stops at $T^* < 3$, when the FTLE saddle starts moving and the vortex ring is completely circular without filamentation at $T^* = 4$ having maximum distribution.

Two time scales

Thus, in high acceleration cases, the vortex stops accepting vorticity and Kinetic energy first by T_f (based on FTLE saddle position) ; then forms a free vortex core by rolling the trailing filament into the

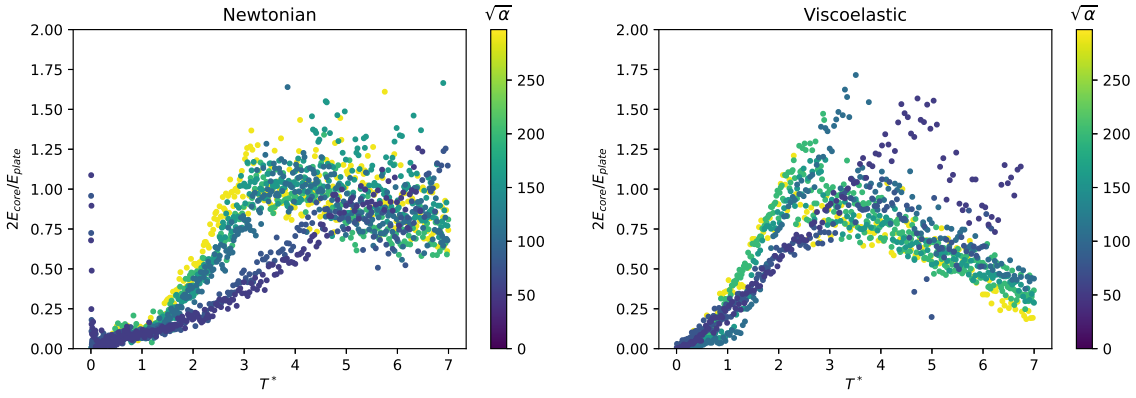

(a) Energy ratio $2E_{core}/E_{plate}$ vs T^* in Newtonian cases

(b) Energy ratio $2E_{core}/E_{plate}$ vs T^* in Viscoelastic cases

Figure 4.9

core around the universal vortex formation time (based on E^* reaching minima with increased vorticity distribution). This result extends the conclusion of [24], that the vortex pinch-off does not cause the E^* to converge to a minimum value. In this study, we add that the kinetic energy of the core reaching closer to the plate is indeed the reason for pinch-off according to Kelvin-Benjamin variational principle, however E^*_{min} does not represent that, but instead a filament-free fully rolled steady vortex at $T^* = 4$. On the contrary, in low acceleration cases the shear layer reaches maximum energy first, and because of that it rolls up to pinch-off. However, it should be noted that E^* of shear region at $T^* = 4$ already reaches the minimum.

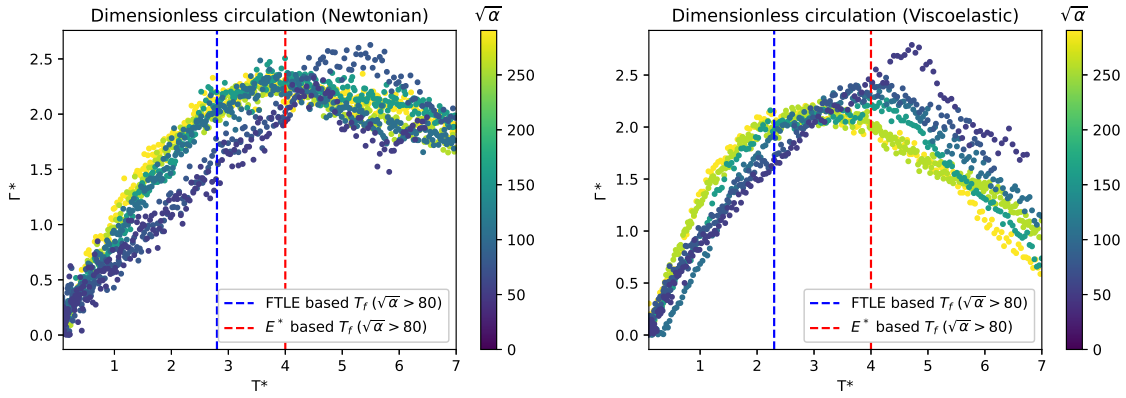

(a) Dimensionless circulation Γ^* in Newtonian cases

(b) Dimensionless circulation Γ^* in Viscoelastic cases

Figure 4.10

Circulation of vortex core

Now that we understand there are two timescales involved, one might wonder when does the vortex properties like circulation and core diameter reach the constant value as in a steady vortex ring. To begin with, let's look at non-dimensional circulation Γ^*. It is defined as the ratio of instantaneous circulation in the vortex core to instantaneous circulation produced by the plane of plate, $\Gamma^* = \Gamma / U_p L_c$, where U_p is the plate velocity. From Figure.4.10, we observe that the circulation growth rate during the formation process is proportional to acceleration in both Newtonian and viscoelastic cases, although the growth rate in viscoelastic cases is slightly higher. The maximum value of $\Gamma^* \approx 2.3$ is reached around FTLE based formation time with a very slight increase till $T^* = 4(E^*_{min})$ for high acceleration cases.Furthermore, $\Gamma^* \approx 2.3$ is surprisingly same as reported in [24] for a cone with much higher $Re_t = \mathcal{O}(10^4)$, make us wonder if this is universal for all drag vortices just as other quantities like E^*_{min}.

Effect of viscoelasticity in Kinetic energy decay

From Figure4.9 and Figure.4.10 it is notable that dE_{core}/dt and $d\Gamma_{core}/dt$ in the presence of viscoelasticity has a significant effect both during formation and after the formation. First, let's try to understand how the decay rates are affected by the presence of viscoelasticity (Note: Only using high acceleration cases). From Figure4.9, It is clear that the dissipation (loss of energy) rate is higher in viscoelastic cases than the Newtonian cases. In a Newtonian fluid, the Kinetic Energy corresponding to viscous stress term of Navier-Stokes equation can be written as[18],

$$\nu \iiint u \cdot \nabla^2 u \, dV = -\nu \iiint \omega^2 dV - \nu \iint \hat{n} \cdot u \times \omega \, dS \tag{4.5}$$

where the first term corresponds to dissipation rate and the second one to viscous transport by diffusion, comparing with turbulent mean kinetic energy equation in [17]. Since, energy dissipation rate and circulation decay rate (see equations 2.5, 2.4) are both strong functions of viscosity in Newtonian, we try to estimate the differences in the presence of viscoelasticity with respect to Newtonian. From Figure.4.11a energy decay rate increases with increase in Wi_t (after a drop in $Wi_t \approx 0.24$) almost linearly indicating higher percentage of elastic stress would cause a higher amount of total stress relaxation.

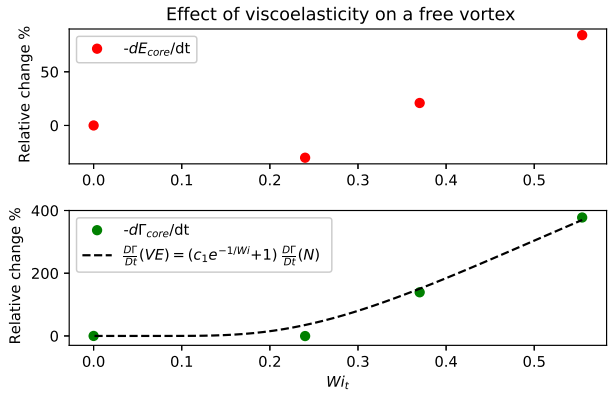

(a) Circulation and energy decay rate in viscoelastic fluids with respect to Newtonian decay rate

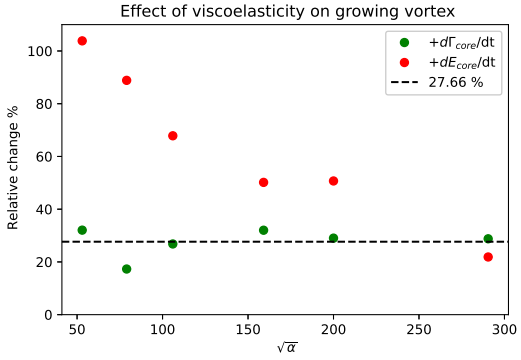

(b) Effect of viscoelasticity on a growth rate of vortex

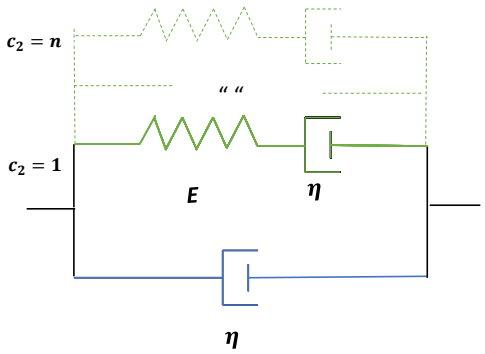

(c) Generalized Maxwell fluid model

Figure 4.11

Effect of viscoelasticity in circulation decay

The circulation decay rate is clearly much higher in viscoelastic cases similar to dissipation rate, and it is notable that the dissipation clearly starts only by $T^* = 4$, the universal vortex formation time when the vortex ring is completely filament free. We measured the decay rates for different cases using Savitzky-Golay filter (9 points average, linear) and linear fit. It was observed that the difference in viscoelastic decay rate is not a function of acceleration, but the Wi_t at which the vortex has pinched off. Based on equation.2.4, circulation decay rate is simply the action of viscous stress. Keeping that in mind, we may try to estimate the relation between Newtonian (viscous stress) and viscoelastic cases (viscous+elastic stress). According to the Maxwell model, the viscoelastic stress decays exponentially $e^{-t/\lambda}$ with respect to initial stress, and we rewrite this as $e^{-1/Wi}$ assuming $t = L_c/U_p$. If we write it as a differential of time to estimate decay rate, it would be $\frac{1}{\lambda}e^{-1/Wi}$. In real fluids, we would expect this decay rate to be reaching the same decay rate as in Newtonian when Wi goes to zero, and so we modify it as $1+\frac{1}{\lambda}e^{-1/Wi}$ assuming both had same initial stress as they have similar maximum circulation in both Newtonian and viscoelastic cases (see Figure 4.10). However, in reality, the total stress in a viscoelastic fluid would be larger than a Newtonian fluid. Because we apply the same instantaneous strain rate on a viscoelastic fluid as in Newtonian, but the proportionality is no longer just viscosity but also should account for elastic nature.In order to estimate the initial elastic stress with respect to the equivalent Newtonian, we use a constant $C_1 = C_2/\lambda$. We use this idea to fit the decay rate, and we found that the viscoelastic cases (VE) scale with Newtonian (N) as shown in Figure 4.11a,

$$\frac{D\Gamma}{Dt}(VE) = (1 + \frac{C_2}{\lambda}e^{-1/Wi})\frac{D\Gamma}{Dt}(N)\ , \quad C_2 = 3.03 \tag{4.6}$$

We can rewrite this in more simplified form of stresses as,

$$\sigma_{VE} = \sigma_{Viscous} + \sigma_{Maxwell} \tag{4.7}$$

This can be interpreted as generalized Maxwell-fluid model that is very similar to Oldryod-B[175], but using one equivalent relaxation time representing the spectrum as shown in Figure.4.11c. Regardless of Re_t , $\sqrt{\alpha}$ or Wi_t, the dimensionless circulation eventually reaches a constant value of $\Gamma^* \approx 2.3$ by the same T^* as estimated using FTLE saddle points, again reinforcing our argument the extra vorticity is no longer accepted into the vortex core after T_f.

Effect of viscoelasticity in circulation growth

Since, the instantaneous strain rate imposed in Newtonian and Viscoelastic cases are same, we can estimate how viscoelasticity may affect the vortex growth. Now to understand how the circulation growth rate is affected, we measured the change in circulation growth rate with respect to Newtonian as in Figure.4.11b. It shows that the circulation growth rate in our viscoelastic cases is consistently $\approx 28\%$ higher than Newtonian cases. This explains the faster pinch-off shown by FTLE T_f in viscoelastic case compared to Newtonian cases as vortex core threshold circulation is reached faster.

Effect of viscoelasticity in Kinetic energy growth

The circulation growth rate is not much affected by acceleration, one may ask how about the Kinetic energy? Figure.4.11b says that for a given viscoelastic fluid, the energy growth rate may depend on the acceleration and fluid but circulation growth rate depend only on the fluid. This increase in circulation and energy rate also explains why the FTLE saddle points move earlier compared to Newtonian cases at high $\sqrt{\alpha}$ as vortex growth thresholds are reached earlier. However, it is still intriguing why all the high acceleration cases have clear start of decay at $T^* = 4$, when the E^* values reach constant. This would reiterate our hypothesis that the circulation and kinetic energy reaches their maximum at $T^* = 2.3$ (VE) measured using FTLE saddle points and the vortex completely becomes freely steady at $T^* = 4$.

Vortex core diameter

The total stress acting on a free vortex act to diffuse and dissipate the energy according to equation.4.5. The net viscoelastic effect on the viscous stress is captured by circulation decay rate (see equation 2.4), whereas the viscoelastic effect on energy dissipation component of the viscous stress is discussed in energy decay rate for a vortex core. Now, the question is, how about the viscoelastic effect on diffusion in vortex core?

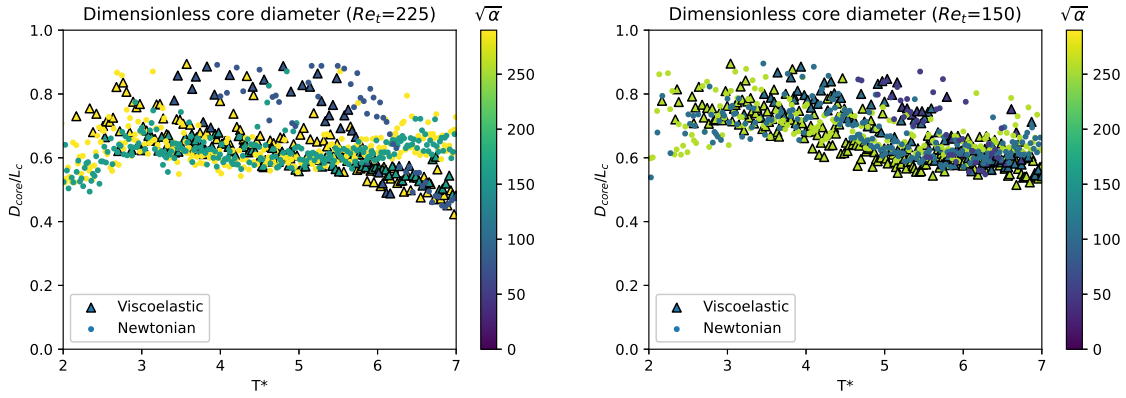

(a) Dimensionless vortex core diameter for $Re_t = 225$

(b) Dimensionless vortex core diameter for $Re_t = 150$

Figure 4.12

In order to see how much of the above discussed stress relaxation affects the diffusive properties of the vortex, we look at the vortex core diameter D_{core} found using Lamb-Oseen fit, as the diffusion would indicate spreading of the vortex core. One might wonder, how can Lamb-Oseen work for viscoelastic cases? Although it is no solution for viscoelastic, we assume that the core is distributed as Gaussian

and the diffusion timescale (core radius) is only affected because of viscoelasticity. Since, the vortex rolls up till $T^* < 1$ in high acceleration cases and $T^* < 5$ in low acceleration cases, we restrict this analysis only after the vortex is rolled up as we cannot measure the diameter for a shear layer. From Figure.4.12a and Figure.4.12b, it can be observed that for high acceleration cases at given Re_t, the core is consistently around $0.6L_c$ for $T^* > 4$ with highest $Wi_t = 0.55$ case alone slightly decays at higher rate. However, the effect of Re_t can be observed before the universal vortex formation time indicating the low $Re_t = 150$ is relatively more diffused with $D_{core}/L_c \approx 0.8$ whereas the $Re_t = 225$ has a tighter core during formation with $D_{core}/L_c \approx 0.6$. The overall trend is that during formation, the vortex core diameter is not much affected by the presence of viscoelasticity. The D_{core} was observed to have reached its maximum value by the same T_f as measured using FTLE saddle point, similar to circulation and kinetic energy. Now, looking at lower acceleration cases, the vortex diameter consistently rolls up into $0.8L_c$ and resulting in an immediate decay despite Re_t or Wi_t.

Decay dominated by dissipation

Since both circulation and diameter decays faster at high Wi, let's compare Figure.4.12a and Figure.4.10b, for the highest $Wi_t = 0.55$ and acceleration ($\sqrt{\alpha} \approx 290$), the circulation reaches closer to half it's maximum value by $T^* = 7$ similar to diameter. This tells us that both are caused by the same mechanism. If that mechanism is dominated by diffusion, we would expect an increase in diameter rather than a decrease. So, we can say that the effect of diffusion in a fully formed vortex is smaller than dissipation. Thus, viscoelasticity enhances the dissipation rate of a fully formed vortex ring, causing a faster decay of circulation and energy.

Vortex ring diameter

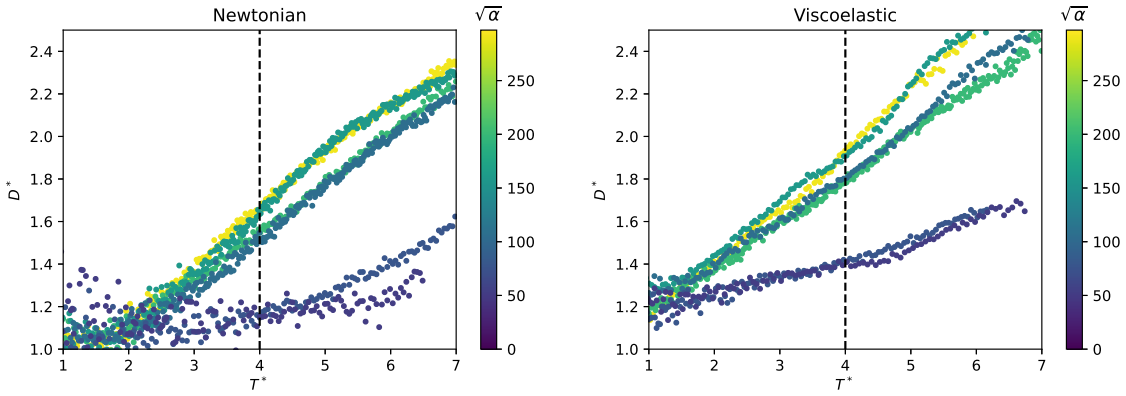

(a) Dimensionless vortex ring diameter (mid-span) $D^* = D_v/L_c$ in Newtonian cases

(b) Dimensionless vortex ring diameter (mid-span) $D^* = D_v/L_c$ in Viscoelastic cases

Figure 4.13

To define a vortex ring, vortex core diameter and the vortex ring diameter are both important. Although we core diameter was estimated, the ring diameter is not straightforward due to AR effects as our vortex ring eventually deforms in the perpendicular direction similar to Figure.2.9 having different diameters in different axis. So, in this analysis we limit ourselves to the mid-span and estimate the radial extent of the vortex ring using $D^* = \frac{D_v}{L_c}$, where D_v is calculated with Y co-ordinate as r axis and centre of chord as origin[24],

$$\frac{D_v^2}{4} = \frac{\iint \omega r^2 dr dx}{\iint \omega dr dx} \tag{4.8}$$

From Figure.4.13a,it can be observed that the diameter is dependent on Re_t and the effect of acceleration is seen only in low accelerations. The consistent rise in the diameter tells us that the vortex ring keeps deforming, with the major axis in the radial direction of the measurement plane. This effect is because of different induced velocities along chordwise and spanwise directions, as they have different lengths. The equivalent diameter of the vortex ring is estimated as D^* at $T^* = 4$ [25].Comparing the Newtonian and viscoelastic cases at $T^* = 4$, we can observe that the viscoelastic cases have larger

ring diameter. This can be interpreted as amplification of radial diffusion as the new factor in the Equation. 2.9 would scale up the equivalent of viscous timescale, similar to scaling of circulation decay rate in the presence of viscoelasticity.

Vortex core translation

So far we observed that E^*,$2E_{core}/E_{plate}$,Γ^*, D_{core}/L_c reaches a constant value indicating vortex formation, atleast in high acceleration cases. In [24], it has been reported that U_{vortex}/U_{plate} was also reaching a constant value in circular vortex ring cases, so it will be interesting for us to look for the same in our cases of elliptical vortex rings. Throughout the formation process of an elliptical vortex ring, we need to directly measure. We calculate the X co-ordinate of vortex core centre with respect to origin in mid-chord as[173],

$$X_v(\text{Plate-Core}) = \frac{\iint r^2 x\omega dr dx}{\iint r^2 \omega dr dx} \tag{4.9}$$

We observed that X_v (Plate-Core) has a slope till $1 < T^* < 3$ and another slope $3 < T^* < 5$ indicating two different mean velocities. Therefore, a linear fit is performed around $T^* = 3$ and $T^* = 4$ to calculate the mean translational velocities with respect to the plate. Then, we transform this to lab-frame to get the core translational velocity in Lab-frame. From Figure.4.14, it can be observed that the differences

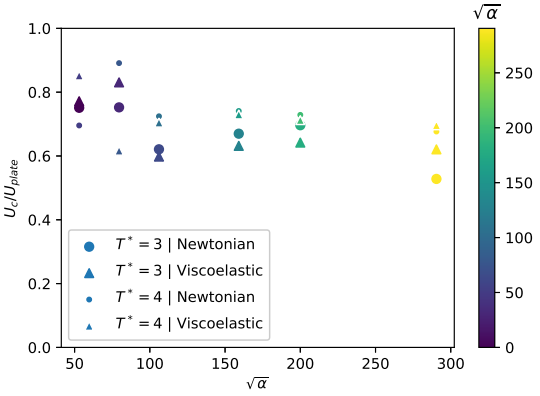

Figure 4.14: Dimensionless Translational velocity $U_c/Uplate$

between viscoelastic and Newtonian cases are negligible, however the velocity $T^* = 4$ is consistently higher as the vortex still follows the plate but no longer pushed away from the plate as an effect of formation or rolling up process. The vortex core translational velocities (Lab-frame) in high acceleration cases are found to be around $0.6U_{plate} - 0.8U_{plate}$, whereas the low acceleration cases have $U_c = 0.8U_{plate} - 0.9U_{plate}$. Overall, the vortex velocities do not change much over time within the formation process in both Newtonian and viscoelastic cases. Unfortunately, we cannot directly compare with results of [24] as the elliptic vortex ring undergoes axis-switching and the velocity of vortex ring cannot be estimated by average core velocity in our cases.

Self-induced velocity

The magnitude of self-induced velocity inside the vortex core can tell us something about the deformation of an elliptical vortex ring. Ideally, the Biot-savart's law has to be solved analytically to estimate self-induced velocity when the shape of elliptical vortex ring is known prior[29]. However, the core averaged velocity can also be used as the self-induced velocity for a given circulation and curvature of the vortex ring[24]. Here, core averaged velocity U_{cav}, is calculated by averaging the net velocity $\sqrt{(u^2 + v^2)}$ in the core as shown in Figure. 4.15. The overall trend in high acceleration Newtonian cases is that the steep increase in velocity stops around FTLE based formation time, $T_f \approx 2.7$ and then there is a slight increase till $T^* = 4$. This again reiterates the story that the plate provides the energy at a steep rate till the formation measured by FTLE based T_f and the filamented structure rolls up to increase the energy slightly by $T* = 4(E^*_{min})$. In the perspective of induced velocity, this would potentially indicate that the deformation effects on the vortex core does not vary much after $T* \approx 2.7 - 4$. The viscoelastic cases follows a similar trend, but the only difference is that the initial velocities are larger with smaller velocity increase .

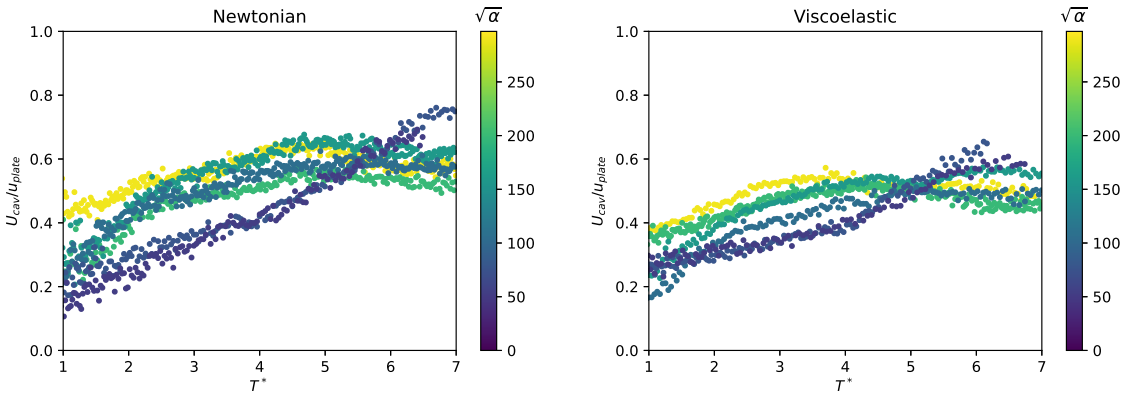

(a) U_{cav}/U_{plate} in Newtonian cases

(b) U_{cav}/U_{plate} in Viscoelastic cases

Figure 4.15

4.1.5. Elastic stress distribution

In order to understand which regions contribute to the increased growth rate of energy and circulation due to viscoelasticity, let's look at the local shear Wi_s and extensional Wi_e in the flow field in Figure.4.16 as they could tell us more about the elastic stress distribution. The extensional strain rate is calculated as $\frac{1}{2}(\frac{du}{dx} - \frac{dv}{dy})$ and shear strain is calculated as $\frac{du}{dy} + \frac{dv}{dx}$.It can be observed that both the shear and extensional elastic stresses are primarily in the shear layer behind the vortex indicating more elastic behaviour along those regions. It is also interesting to note that the shear based elastic stresses primarily dominate the flow ($Wi_s > Wi_e$) mainly because of larger relaxation time. The negative extensional elastic stresses are also mostly in the shear layer, simply working along with shear elastic stress. However, a region downstream of the vortex seem to have a streamwise extensional stress. For vortices that roll up after longer distance would have the fluid parcels that have experienced larger total strain. The larger the total strain, the larger is the extensional viscosity as the polymer tries to oppose the extensional pull with increasing strain. This explains the viscoelastic delay in formation at low accelerations (see Figure.4.7b). At high accelerations, the extensional stress (-ve direction) is acting to bring the fluid parcels closer, thus explaining faster rates of vortex formation.

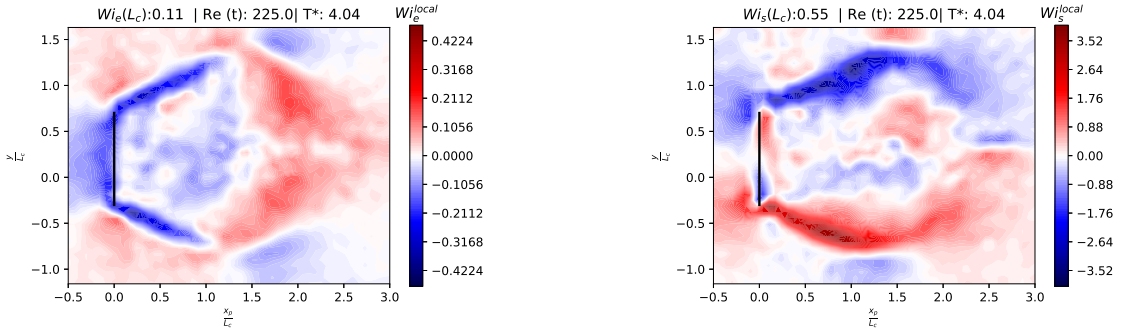

(a) Elastic extensional stress, represented by local Wi_s

(b) Elastic shear stress represented by local Wi_s

Figure 4.16: Elastic stress distribution in the flow field

4.2. Forces

So far, we have discussed the dynamics of vortex formation, comparing the effects of acceleration and viscoelasticity. In largely separated flows like our cases, the vortices contribute significantly to the forces acting on a body. We particularly focus on drag forces here, as we are dealing with a bluff body. An example of net forces acting on the plate for Newtonian and Viscoelastic cases is shown in Figure.4.17. The overall trend is that the net force increases linearly till about the end of acceleration T_a^*, followed by a sudden drop, after which the drag force converges to a steady-state value as the plate is moving with constant velocity. However, we note that there is an instantaneous peak at the instant of starting to accelerate, followed by relatively smaller unsteady force before reaching the steady state. The origin of the sudden peak is not clear, we suspect that it is likely due to structural stiffness or spurious measurement effects and is thus non-hydrodynamic in origin. On first impression, viscoelasticity appears to have two effects on the force, when compared with the Newtonian case: A general increase in the magnitude of the drag force during both the accelerative and steady-state phases of motion, and a reduction in the magnitude of the post-acceleration drop in force. To understand them better, let's decompose the forces into steady and unsteady components.

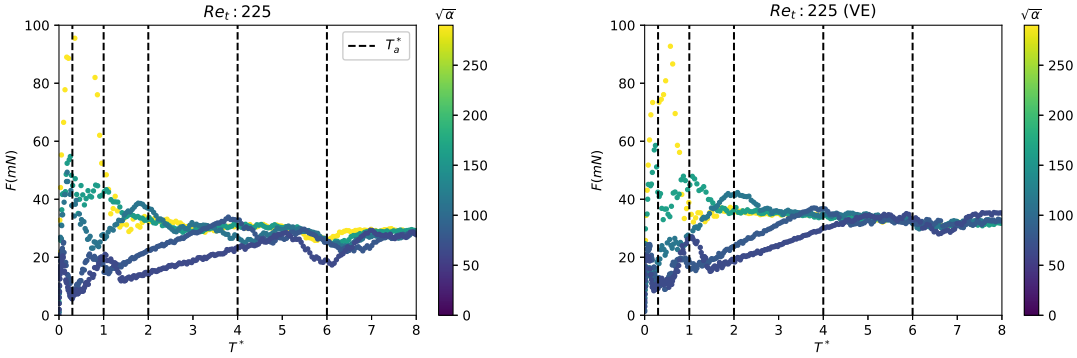

(a) Net hydrodynamic force acting on the plate in Newtonian cases with various T_a^*

(b) Net hydrodynamic force acting on the plate in viscoelastic cases with various T_a^*

Figure 4.17

4.2.1. Steady forces

We perform force measurements at various $Re_t < 225$ with impulsively started accelerations of $1.29 m/s^2$ and $0.86 m/s^2$ corresponding to $\sqrt{\alpha} = 355.8, 290.5$. The net hydrodynamic forces acting on the body are measured as discussed in section 3.4.1.The total force acting on the plate is separated into the steady force component by taking the mean of forces with $T^* > 5$, such that the effect of acceleration is avoided. The drag coefficient is calculated as the mean of two acceleration cases with corresponding standard error is shown in Figure.4.18.

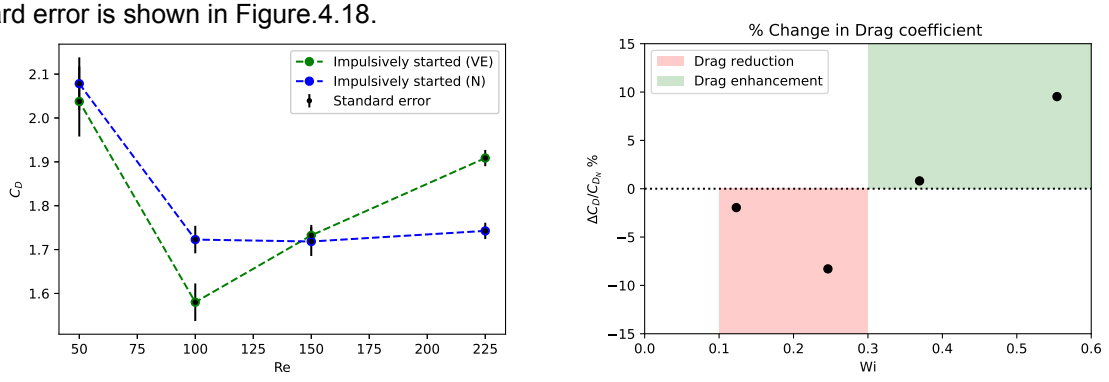

(a) Steady state drag coefficient C_D as a function of Re in Newtonian and Viscoelastic cases

(b) %Change in steady state viscoelastic drag coefficient C_D with respect to Newtonian drag coefficient C_{D_N}

Figure 4.18

It is interesting to observe that there is a drag reduction regime followed by drag enhancement

regime. Comparing Figure 4.18b with Figure 2.26, the qualitative trend of drag reduction followed by drag enhancement agrees well with the literature. Interestingly, this trend correlates well with the relative change in energy decay rate due to viscoelasticity in Figure.4.11a. The net force acting on a body is equal to rate of change of kinetic energy per unit velocity. In the viscoelastic and Newtonian cases, the velocity of plate/vortex is nearly the same, thus the change in kinetic energy rate due to viscoelasticity has to correlate with the change in forces. The aforementioned effect when occurs in the wake is bound to affect the steady drag forces acting on the plate (see equation 2.13). However, the magnitude of Wi for drag enhancement is much smaller compared to literature. We suspect this discrepancy is mainly an effect of polymer viscosity ratio as the Figure 2.26 is reported for $\beta_r = 0.01$ around cylinder, whereas the fluid in our study has $\beta_r = 0.57$ around flat normal plate. From equation 2.47, the retardation time $\lambda_r = (1-\beta_r)\lambda$, decreases as β_r increases, thus resulting in faster elastic stress response. This explains smaller Wi at higher β_r showing similar effects as in larger Wi at smaller β_r. This agrees well with the other studies [133, 176] that β_r indeed affects the vortex shedding and hence the associated forces.

4.2.2. Unsteady forces

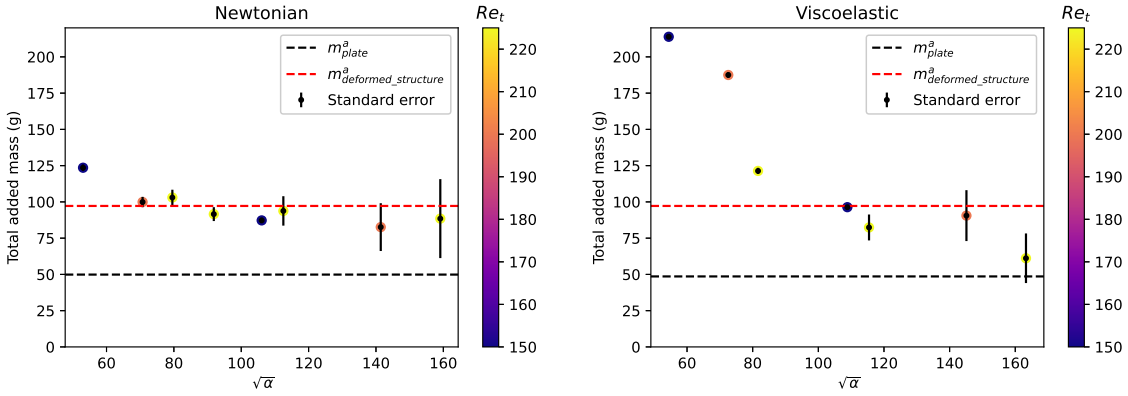

(a) Added mass in Newtonian cases

(b) Added mass in Viscoelastic cases

Figure 4.19

Once, we know how the steady forces change as a function of Re, we can extract the unsteady contribution during the acceleration phase. For this purpose, we use the drag coefficients from Figure.4.18 to remove steady force contribution in both viscous and viscoelastic cases during acceleration,

$$F_{unsteady} = F_{net-hydrodynamic} - F_{steady} \tag{4.10}$$

Then, we calculate the added mass associated with this force, dividing by the acceleration and carefully averaging the data points without structural effects ,

$$\text{Total added mass} = \overline{F_{unsteady}/a} \tag{4.11}$$

The measured added mass is plotted against $\sqrt{\alpha}$ for different cases as shown in Figure 4.19. From first look of Newtonian cases in Figure 4.19a, we can see that the added mass estimated using potential flow theory is under-predicting by 50%, where added mass of plate m^a_{plate} is given by,

$$m^a_{plate} = \underbrace{\rho\,(\pi\frac{L_c^2}{4}H)}_{\text{Drift volume}} \tag{4.12}$$

According to potential flow theory, drift volume of a plate is equivalent to that of a cylinder with equivalent diameter of plate's chord length; hence we use the volume of cylinder. To visualize this, let's look at streamlines of potential flow past flat plate (conformal mapped from cylinder-see Figure.4.20) with complex velocity,

$$U_z = U(1 - R^2/z^2)/(1 + R^2/z^2) \tag{4.13}$$

, where $R = L_c/4$ and complex plane coordinate $z = x + iy$[40]. From Figure.4.20, we can observe that for an ideal flow past a plate, the streamlines exhibit a similar behaviour as around a cylinder. If we were to put the Lagrangian particles, they would drift from the free stream based on streamline deviation with respect to the mean flow. Since the streamline deviation can be represented as a cylinder, the plate's drift volume is represented using the volume of the cylinder. This interpretation is easy to understand, especially in flow past a plate, as the presence of the solid object is infinitely thin unlike sphere or cylinder. In a real inertial-viscous flow, this approximation would not work as we have non-zero vorticity resulting in vortices. To visualize this using potential flow theory, we add an irrotational vortex pair with equal strength separated by a distance to flow past a plate, although their vorticity is zero. The angular velocity of an irrotational vortex is given by $U_\theta = \Gamma/2\pi r$. We can see from Figure.4.20 that even in a

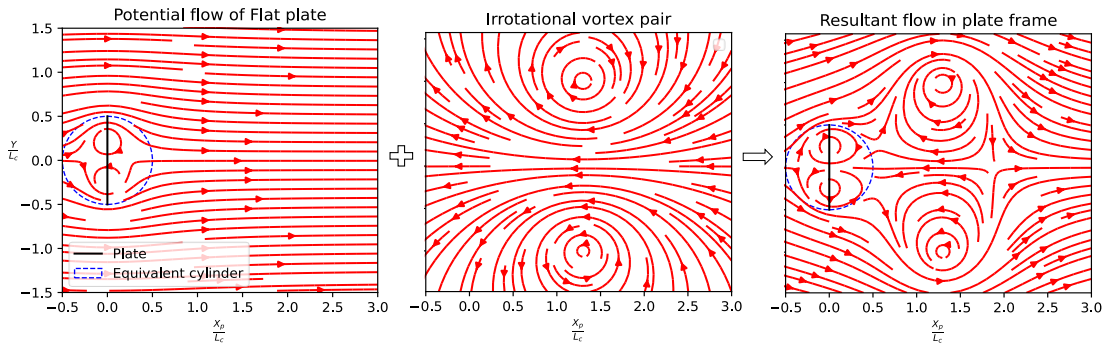

Figure 4.20: Equivalent potential flow of high acceleration cases, where plate flow is conformal mapped from cylinder

potential flow with a vortex pair, the drift volume (streamline deviation) shape looks completely different from cylinder as in a simple flow past a flat plate. Therefore, we can safely say that the vortex pair also contributes to the drift volume and so to the added mass. It has also been reported by [65], that the vortex rings have their own added mass, and it has been used in addition to geometry's added mass in a few studies dealing with animal locomotion[177]. Furthermore, this idea formed a basis for energized mass approach[63] (see equation 2.31) which tries to counter this problem using kinetic energy based on equation 2.24. However, comparing at the streamlines of our case in Figure.3.21 with Figure.4.20, we can see that there is no such cylindrical drift region before the plate in real flows and moreover the shear region connecting vortex to the plate also contributes to drift. Therefore, in this case, we cannot simply add the added mass of plate and vortex. On the other hand, the energized mass approach does not differentiate into steady and unsteady components, making it difficult to use as a simple model without PIV data. Hence, we need a simpler, generalizable and interpretable model that accounts for the presence of vortices and shear region.

4.2.3. What is added mass?

To begin with, let's look closer at the concept of added mass. In section.2.4.2, we discussed that the potential flow added mass does not predict the measured added mass well in multiple studies and many models were proposed. But most of those studies deal with turbulent high Re flows, so the mismatch of the potential flow based added mass for a laminar vortex shedding with $Re < 225$ comes as a surprise. However, it was noted by Charles Darwin in one of the earlier studies[178], that unlike an ideal flow, the real flows may have a wake (translating object) or permanently entrained eddy (rotating object) that could influence added mass solutions. It is interesting to note that a review on added mass[60] also suspected that the flow separation and vortex shedding might have effects on the added mass; however, by that time there were unclear results in the literature. Therefore, the review [60] called for more research on this aspect of added mass. This would imply that the change in added mass is not limited to turbulent flows, but also in the laminar separated flows. At this juncture, we might wonder what is added mass in separated flows? First, let's look back to the definitions of added mass,

- According to G.K.Batchelor[179]"The acceleration reaction (unsteady force) is related to the fact

that, when the velocity of the body changes, the total kinetic energy of the fluid changes also. The part of the kinetic energy of the fluid arising from the translational motion of the body, and not from any circulation which may exist, is thus representable as an amount of energy arising from a certain addition to the mass of the body (added mass)"

- According to Charles Darwin[178],
  - " Hydrodynamic (added) mass is the mass that is derived from the kinetic energy of the fluid surrounding the body".
  - "For free space the drift-volume is equal to the hydrodynamic mass; whereas Drift volume is the total displacement of a particle in the x direction, referred to axes in which the infinite parts of the fluid are at rest".
  - "An amount of fluid corresponding to the hydrodynamic mass is being really carried along by the solid body."

What are we missing ?

Now, let us use these definitions on a separated flow. The first question that we can ask is,

- **Which fluid parcels are changing their kinetic energy due to the motion of the plate ?**

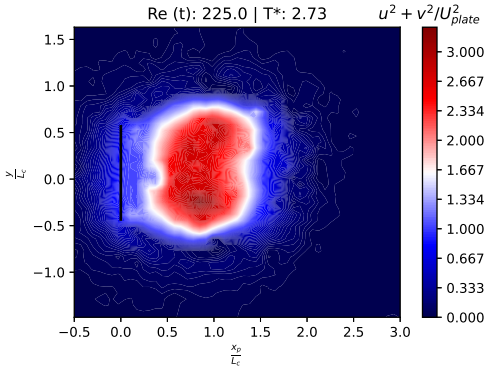

Figure 4.21: Region of high kinetic energy behind the plate, indicated by kinetic energy ratio per unit parcel

From Figure.4.21, we observe that the major changes in kinetic energy occurs behind the plate, which we call as the wake.

- **How do we measure the drift volume that corresponds to this region of high kinetic energy?** In[65], the drift volume of a vortex pair is estimated by transforming it to the vortex frame. By using that and our analogy with streamlines with previous sections, we can use the streamlines in the frame of the object of interest to see how the fluid parcels are moving around that object. The object that we are interested here is the wake, but we can use a slightly higher approximation of vortex velocity, assuming that the centroid of the vortex is slightly closer to the wake centroid towards the plate. Since we know the vortex velocity (see Figure.4.14), we approximate the average vortex velocity to be around $U_{vortex}/U_{plate} \approx 0.8$ (slightly higher than vortex velocity and lesser than plate velocity to account for total wake).
- **How do we make sure that a region of fluid moves along with the body's mass, acting as *added* mass?**
  In order to make sure that a region of fluid parcels are moving along with the plate, we can check, if they belong to the same dynamically distinct region using FTLE ridges. This also helps us in making sure that our solution is Galilean invariant.

4.2.4. Drift volume estimation

By using the aforementioned arguments, we attempt to model the net drift volume that moves with the plate, causing the unsteady added mass force. We use streamlines of the flow field with respect to vortex frame. FTLE ridges are also ideal to extract regions delineated by transport barriers which can be interpreted as coherent boundaries, causing drift of fluid parcels around them. First, we stick to

analysis of the highest acceleration Newtonian case. The FTLE ridges and vortex-frame streamlines of a vortex ring closer to FTLE based formation time $T_f \approx 2.7$ (empirical choice for initial analysis) is shown in Figure.4.22. It is notable that both approaches provide more or less the same boundary of the wake. Therefore, we will further use streamlines in the discussion as it is computationally way less expensive compared to FTLE calculations.

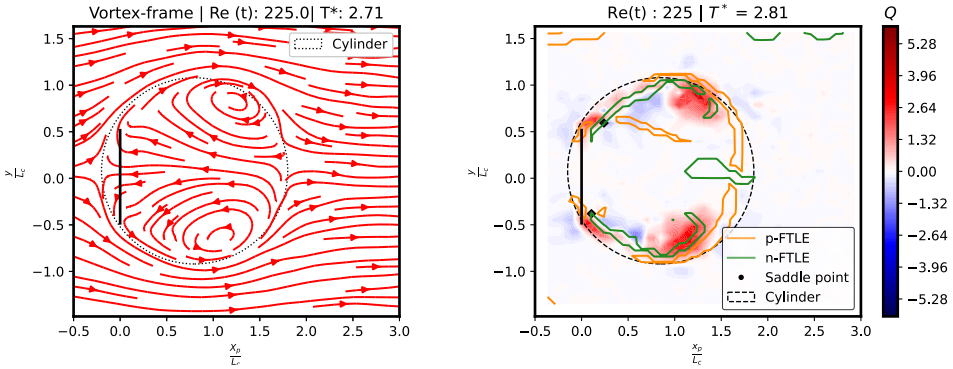

(a) Streamlines calculated in vortex frame shows the wake boundary marked by a circle for $\sqrt{\alpha} \approx 290$

(b) Calculated FTLE field closer to formation time shows the wake boundary marked by a circle for $\sqrt{\alpha} \approx 290$

Figure 4.22

Force decomposition

Before we proceed further, let's take a step back. From the above arguments, it appears that added mass is wake's mass in our case. If it is so, how about the rest of the force components? In order to have clear idea of decomposing the forces, we do a control volume analysis for mass and momentum balance. Note that velocity vectors are simply represented without vector symbols for ease of reading. The lab frame velocity of any fluid-parcel can be written as the sum of plate's velocity and velocity in plate's frame $u_{lab-frame}(t) = U_{plate}(t) + u(t)$. The chosen control volume is shown in Figure.4.23. For a deforming control volume (Wake region that is dynamically attached to plate) with instantaneous volume $V(t)$ that is translating with acceleration a along with *massless plate*, the total force is the rate of change of velocity for fluid parcels in lab-frame

$$F_{hydrodynamic} = \iiint_{wake} \rho \frac{D(U_{plate}(t) + u(t))dV}{Dt} = \underbrace{m_{wake}(t)a_{plate}}_{1} + \underbrace{\iiint_{wake} \rho \frac{Du(t)dV}{Dt}}_{2,3} \tag{4.14}$$

where $m_{wake} = \rho V_{wake}$, and V_{wake} is the wake volume. Now the acceleration (1) is taken care in the lab-frame of reference. We move to plate's frame of reference and, to estimate the drag forces, we use x-momentum (u_x) equation with free stream velocity $u_x(t) = U(t)$ for the control volume shown in Figure.4.23,

$$\iiint_{wake} \rho \frac{Du_x(t)dV}{Dt} = \rho \iiint_{wake} \frac{\partial u_x(t)dV}{\partial t} + \rho \iint_{wake} u_x(t)(u(t) \cdot \hat{n})dA \tag{4.15}$$

Since, the acceleration of free stream is already accounted for and the plate is not moving in the given control volume, only the volumetric change contributes. Here, we assume that *the local acceleration in the accelerating frame is much smaller than the frame's acceleration.*

$$\rho \iiint_{wake} \frac{\partial u_x(t)dV}{\partial t} = \rho \iiint_{wake} u_x(t) \frac{\partial dV}{\partial t} + \rho \cancelto{0}{\iiint_{wake} \frac{\partial u_x(t)}{\partial t} dV} \tag{4.16}$$

$$\rho \iint_{wake} u(t)(u(t) \cdot \hat{n})dA = \underbrace{\rho \iint_{out} u(t)^2 dA - \rho \iint_{in} U(t)u(t)dA}_{\text{(3)Momentum flux}} \tag{4.17}$$

where $U(t)$ is the velocity of inlet fluid parcels in the plate's frame. The negative sign for the inlet indicates that the normal direction of the inlet boundary opposes the fluid motion. This is what we would expect in the case of steady flow past an object (see equation.2.13). It is important to note that terms for deformation rate (2) and momentum flux (3) are functions of instantaneous velocity. These terms would be effective even in cases where the flow is steadily translating at constant velocity. Because, the vortex grows and sheds even in case of a steady flow past a flat plate. Therefore, we can safely say that the steady force acting on a fixed control volume for a given velocity can be written as,

$$F = \underbrace{\rho \iiint_{wake} u_x(t) \frac{\partial dV}{\partial t}}_{\text{(2)Deformation rate of wake}} + \underbrace{\rho \iint_{out} u(t)^2 dA - \rho \iint_{in} U(t)u(t)dA}_{\text{(3)Momentum flux}} \tag{4.18}$$

The magnitude of this force will be equal to the steady state drag F_{steady} experienced by the plate, since all of these components are a function of velocity and would be active also in constant velocity vortex shedding. Based on our experiments, all of our steady forces that are a function of velocity are captured using drag coefficients as a function of Re. Now assuming that drag coefficients as a function of time, varying with, $Re(t)$ captures these velocity forces, we can say that F_{steady} is predicted by instantaneous drag coefficients at any given instant. This would imply that, only component 1 in equation.4.14 is dependent on acceleration. Hence, we can say that the unsteady force $F_{unsteady}$ solely because of acceleration is due to the acceleration of wake mass, assuming no delay in boundary layer separation with corresponding to instantaneous Re. The total hydrodynamic force acting on an accelerating plate in equation. can be rewritten as,

$$F_{hydrodynamic} = F_{steady} + F_{unsteady} = \underbrace{C_D \frac{1}{2} \rho U_{plate}(t)^2 A_{plate}}_{\text{2,3}} + \underbrace{m(t)_{wake}\, a}_{\text{1}} \tag{4.19}$$

This decomposition can be interpreted as the sum of the force due to wake momentum lost to plate, wake mass growth rate and acceleration of wake mass along with the plate. Thus, we recover the steady-unsteady decomposition but with mass of wake as added mass instead of potential flow based added mass.

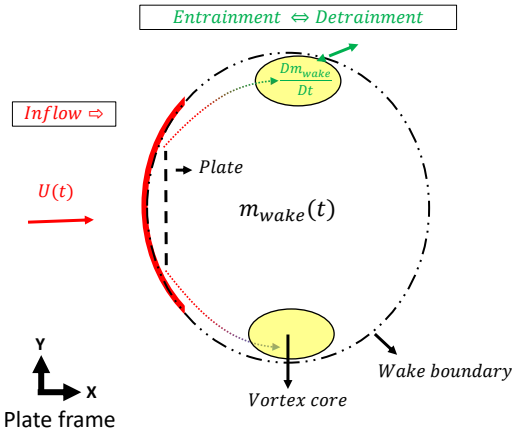

Figure 4.23: Control volume chosen for the analysis in plate frame

Elliptical vortex ring

Now, let's try to estimate a case of wake mass using streamlines and FTLE ridges in Figure.4.22a. We can observe that the drift volume can be approximated to that of a 2-D cylinder but with diameter, $D_c = 2L_c$, differing from the typical value, $D_c = L_c$, predicted using potential flow past a flat plate. Assuming that this flow field is the same throughout the span of the plate, the resulting added mass would be four times the value predicted by potential flow theory, or twice the value we measure. However, Figure.2.9 shows the existence of the axis switching behaviour of the elliptical vortex ring behind the plate at $T^* \approx 2.5$. The axis switching deformation is explained as an effect of different induced velocities at different radius of curvature (Rcc) although they would have similar circulation (related by $U_{induced} = \frac{\Gamma}{4\pi Rcc} ln(\frac{Rcc}{R_c})$ [180]) ; the axis switching behaviour has been well studied in literature[25, 180]. Since the observed diameter in the measurement plane is $2L_c$, we assume that axis switching has occurred, the out-of-plane dimension will be $\mathcal{O}(L_c)$. Hence, the added mass force acting on our AR=2 plate due to a drift volume of these dimensions can be estimated as

$$m^a_{deformed\_structure} = m_{wake} = \rho \underbrace{\pi L_c^2 (L_c)}_{\text{Drift volume}} \tag{4.20}$$

A summary of this out-of plane dimension modelling is shown in Figure.4.24.This expression estimates the measured mean added mass of almost all the Newtonian cases well as shown in Figure.4.19a.This would imply that in the matching cases, the coherent wake structures around the plate are indeed contributing to added mass. It can also be observed from Figure.4.19a that the lowest acceleration cases has a slightly higher value, because the vortex does not roll up in all the low acceleration cases. Unfortunately, we cannot model this difference as we do not know how the corresponding 3D structure may look like in unrolled up cases.

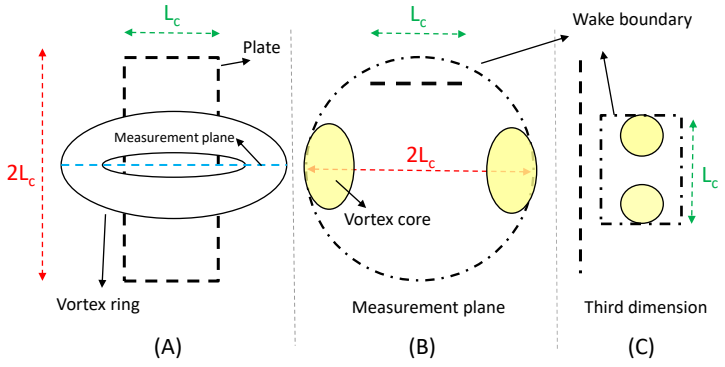

Figure 4.24: Lab-frame : (A) Vortex ring formed behind the plate undergoes axis switching. (B) The wake boundary is measured in measurement plane using Figure.4.22a C) Assuming axis-switched height, wake volume modelled as cylinder of height L_c

4.2.5. Change in added mass with time

Now, if we were to say that wake volume is equal to the drift volume; one might wonder, does added mass changes with time? Because the vortex is growing and so is wake. To understand this, we extract the wake volume for different dimensionless times, as shown in Figure.4.25a. In the optimal vortex formation cases with $AR = 2$, it has been shown by another study[181] that the vortex dynamics and forces are independent of the Re. The reason was explained as the fact that the drag forces are mainly governed by the deforming vortices, whereas the deformation is a strongly due to elliptical vortex ring curvature. Keeping this into account, we can assume that the vortex dynamics does not change

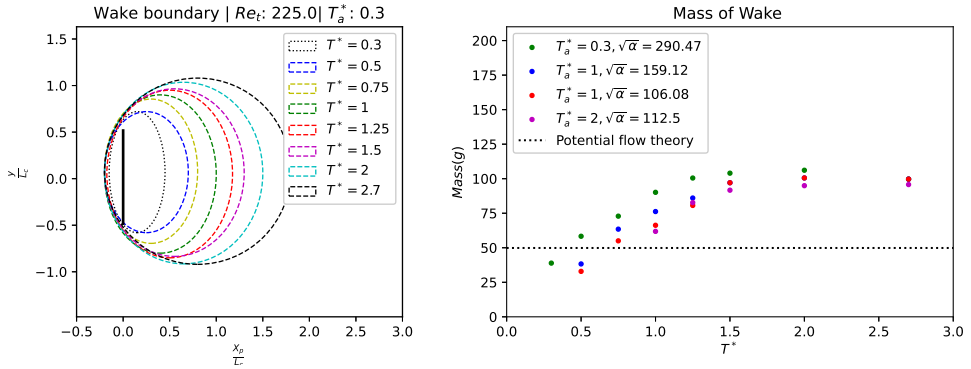

(a) Wake boundary measured using vortex frame streamlines

(b) Predicted wake mass from wake boundary taking axis-switching into account

Figure 4.25

much because of Re. We also need to note that the formation distance is not much different in the high acceleration cases (see Figure.4.7d). However, the acceleration can potentially play a role about the dynamics of the wake. The wake volume evolution with T^* in different cases can potentially provide an insight for the wake volume change over time. In order to do that, we need to know the third dimension, accounting for axis switching. In Figure.2.9 [25], the vortex axis is the same as plate axis at $T^* \approx 0.6$ ($s^* = 0.5$ in Figure.2.9) and this axis is shifted at $T^* \approx 2.5$ ($s^* = 2$ in Figure.2.9). Now, assuming that the axis switching is linear with T^* , based on Figure.4.13a for D^* growth in measurement plane; we calculate the span of the wake, thus the wake volume as shown in Figure.4.25. The overall trend is that the wake volume increases till around $T^* \approx 1 - 1.5$ and remains constant till formation $T^* \approx 2.7$. Compared to the potential flow added mass, wake mass is higher for all $T^* > 0.5$. Moreover, comparing Figure.4.25b and Figure.4.19a, we can say that the predicted wake mass resembles close to that of the measurements. Note that the mean added mass is measured only after $T^* > 0.75$ in $T_a^* = 1$ cases and for other cases more data points are used with $T^* > 1$ or $T^* > 2$ depending on T_a^*. Now that it's clear that the added mass is a function of T^*, the measured (for T_a^*) and predicted added mass are plotted over each other as a function of T^* in Figure.4.26. The overall trend looks agreeable with the experimental data. However, due to the experimental limitation in measuring smaller T^*, the growing added mass cannot be captured in our experimental data. Hence, we cannot validate the growth rate of added mass in this study.

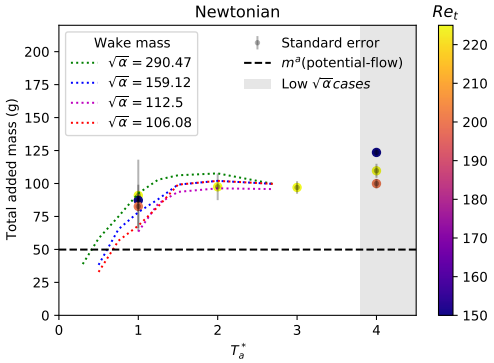

Figure 4.26: Comparing measured added mass with predicted added mass using the empirical wake volume

Effect of viscoelasticity in added mass

Now that we understand how added mass works in Newtonian cases, how does it work in viscoelastic cases? It can be observed from Figure.4.19b,that the added mass measured in viscoelastic cases varies with acceleration. At higher accelerations, the measured value approximates that we observed in the equivalent Newtonian cases, while at lower accelerations the added mass in the viscoelastic cases

is observed to be significantly higher. For the same reason of no priori knowledge on 3D structure of low acceleration cases, we cannot find the corresponding drift volume. However, this difference in added mass can be compared with the relative change in rate of change of Kinetic energy with respect to Newtonian cases of Figure.4.11b as they are equivalent by equation.2.24. The viscoelasticity is found to amplify the added mass at lower accelerations. Invoking the observation of higher circulation and energy growth rate due to viscoelasticity, this amplification can be interpreted as larger wake volume due to more entrainment of fluid parcels, which can be observed through the enhancement of steady drag. When the entrainment rate is larger, we would expect a larger wake volume. In the lower accelerations (not rolled up) that do not involve in axis-switching have larger added mass. A larger wake argument explains this increase, and it can be cross verified by increased vortex ring diameter in the measurement plane due to the presence of viscoelasticity in low acceleration cases (see Figure.4.13). Note that the wake volume does not change much in high acceleration (optimal vortex formation) cases, as the axis-switching behaviour (function of circulation and curvature alone) dominates the flow dynamics as reported in [181]. We think this is indeed the case even in the presence of viscoelasticity in our high acceleration cases that are closer to Newtonian in Figure.4.19b. Thus, we can conclude that at high accelerations in our cases, the added mass is not much affected by viscoelasticity, whereas in low accelerations, the wake volume increases causing increased added mass.

5

Conclusion

5.1. Vortex dynamics

- Depending on the acceleration, the **vortex formation type** can follow two pathways: optimal vortex formation at $T^* < 4$ independent of acceleration and vortex formation from a larger shear layer at $T^* > 4$ based on acceleration. **The limit of optimal vortex formation is $\sqrt{\alpha} >\approx 75-80$.**
- The **vortex formation** process involves two different **time scales**, one indicated by FTLE saddle points as $T^* = 2.7$ for Newtonian and $T^* = 2.3$ for viscoelastic. The other one is $T^* = 4$ as shown by E^* in this study and throughout the literature. The kinetic energy ratio and dimensionless circulation showed that the maximum is reached at the saddle point based T^*, which means no more energy/vorticity is supplied by the plate to the core. However, the rest of the filamented region between the trailing shear layer and formed vortex has to roll into the vortex and thus E^*_{min} explains that the vorticity distribution is maximum for $T^* > 4$ meaning a fully steady circular cored vortex ring.This is also when the core averaged velocity reaches its maximum and circulation decay starts. **We conclude that T_f of FTLE is the pinch-off time (Plate no longer supplies energy and vorticity to the forming core), whereas $T^*(E^*_{min})$ represents the formation time of a steady filament-free vortex ring. This extends the conclusion of [24] that E^*_{min} does not indicate pinch-off**.
- During vortex formation, the **viscoelasticity** primarily affects the **circulation growth rate and energy growth rate** by enhancing them. The circulation growth rate is enhanced by $\approx 30\%$ and energy growth rate is enhanced inversely proportional to acceleration or De. This enhancement can be interpreted as pulling of adjacent fluid parcels due to elasticity and here an effective stress relaxation is not seen as the stresses keep building at an increasing rate with time.
- After formation, the viscoelasticity increases the **dissipation rate** with Wi for a fully **steady vortex**. This follows a similar trend as of relative change in steady force on the plate. On the other hand, **circulation decay rate** increases exponentially with Wi, enabling us to reconstruct the stress relaxation as a generalized Maxwell model which is similar to Oldroyd-B.
- For a fully formed (optimal) vortex, **constant values** are reached for $\Gamma^* = 2.3, E^* \approx 0.3, U_{core}/U_{plate} = 0.5-0.6$, $E_{plate} = E_{ring}, D^*_{core} = 0.6-0.8$. Interestingly, $\Gamma^* = 2.3$ is the same found in [24] despite having a completely different order of Re, object shape and aspect ratio.

5.2. Forces

- The **Steady force** has both drag reduction and enhancement regime due to the presence of viscoelasticity. The Wi and β_r are the important parameters to characterize them, which is in agreement with CFD studies in literature.
- The **unsteady force** acting on the plate is due to the **acceleration of wake (added) mass that is hydrodynamically attached to the plate**, whereas the laminar vortex core entrainment effects are accounted for in the steady state drag forces. At lower accelerations, a slight increase in the unsteady forces is observed. It can be thought of as a combined effect of larger wake volume due

to extended shear layer along with no axis switching in delayed roll-up cases. The **viscoelasticity** is found to amplify this increased force at lower accelerations. Invoking the observation of higher circulation and energy growth rate due to viscoelasticity, this amplification can be interpreted as larger wake volume due to more entrainment of fluid parcels, which can be observed through the enhancement of steady drag. The wake volume of plate can be estimated using both the FTLE ridges and wake/vortex frame streamlines, which similar to approaches used on propulsion based animal wake[177].

References

[1] Dieter Etling. “An unusual atmospheric vortex street”. In: *Environmental Fluid Mechanics* 19.5 (2019), pp. 1379–1391.

[2] EJ Grift et al. “Drag force on an accelerating submerged plate”. In: *Journal of Fluid Mechanics* 866 (2019), pp. 369–398.

[3] Mohd Firdaus Bin Abas et al. “Flapping wing micro-aerial-vehicle: kinematics, membranes, and flapping mechanisms of ornithopter and insect flight”. In: *Chinese Journal of Aeronautics* 29.5 (2016), pp. 1159–1177.

[4] JM Verhelst. “Model evaluation and dynamics of a viscoelastic fluid in a complex flow”. Undefined/Unknown. PhD thesis. Delft University of Technology, 2001. ISBN: 90-407-2239-0.

[5] Ewoldt Research Group. *Key Rheological Phenomenon: Rod-Climbing*. 2016. URL: https://www.youtube.com/watch?v=P8hFf7e4sa4.

[6] Ada-Ioana Bunea and Rafael Taboryski. “Recent advances in microswimmers for biomedical applications”. In: *Micromachines* 11.12 (2020), p. 1048.

[7] Gaojin Li, Eric Lauga, and Arezoo M Ardekani. “Microswimming in viscoelastic fluids”. In: *Journal of Non-Newtonian Fluid Mechanics* 297 (2021), p. 104655.

[8] David N Sibley. “Viscoelastic flows of PTT fluids”. PhD thesis. University of Bath, 2010.

[9] L Kátai-Urbán and Zoltán Csépl ı. “Disaster in the Ajka Red Sludge Reservoir”. In: *Sixth Meeting of the Conference of the Parties to the Convention on the Transboundary Effects of Industrial Accidents, The Hague*. 2010, pp. 8–10.

[10] 2020. URL: https://encyclopedia.pub/entry/2680.

[11] Zhan Hanhui, Zhang Xiaoqi, and Zhan Xuehui. “Coagu-flocculation mechanism of flocculant and its physical model”. In: (2004).

[12] Li Xi. “Turbulent drag reduction by polymer additives: Fundamentals and recent advances”. In: *Physics of Fluids* 31.12 (2019), p. 121302.

[13] GE Gadd. “Turbulence damping and drag reduction produced by certain additives in water”. In: *Nature (London);(United Kingdom)* 206.4983 (1965).

[14] Nkosilathi Vundla and B Daya Reddy. “A computational study of viscoelastic blood flow in an arteriovenous fistula”. In: *arXiv preprint arXiv:2003.08176* (2020).

[15] George B Thurston and Nancy M Henderson. “Effects of flow geometry on blood viscoelasticity”. In: *Biorheology* 43.6 (2006), pp. 729–746.

[16] Morteza Gharib et al. “Optimal vortex formation as an index of cardiac health”. In: *Proceedings of the National Academy of Sciences* 103.16 (2006), pp. 6305–6308.

[17] Pijush K Kundu, Ira M Cohen, and David R Dowling. *Fluid mechanics*. Academic press, 2015.

[18] Philip G Saffman. *Vortex dynamics*. Cambridge university press, 1995.

[19] Michael Dickinson. “How to walk on water”. In: *Nature* 424.6949 (2003), pp. 621–622.

[20] *6 fundamental theorems: vorticity and circulation*. URL: https://www.eoas.ubc.ca/~swaterma/512/LectureNotes/6_Fundamental_Theorems_Vorticity_and_Circulation.pdf.

[21] H Keith Moffatt. “A brief introduction to vortex dynamics and turbulence”. In: *Environmental hazards: the fluid dynamics and geophysics of extreme events*. World Scientific, 2011, pp. 1–27.

[22] Simon J Corkery, Robbie J Stevens, and Holger Babinsky. “Low Reynolds number surge response of a flat plate wing at 90 degrees incidence”. In: *55th AIAA Aerospace Sciences Meeting*. 2017, p. 0330.

[23] John O Dabiri. “Optimal vortex formation as a unifying principle in biological propulsion”. In: *Annual review of fluid mechanics* 41 (2009), pp. 17–33.

[24] Guillaume de Guyon and Karen Mulleners. “Scaling of the translational velocity of vortex rings behind conical objects”. In: *Physical Review Fluids* 6.2 (2021), p. 024701.

[25] John N Fernando and David E Rival. “On vortex evolution in the wake of axisymmetric and non-axisymmetric low-aspect-ratio accelerating plates”. In: *Physics of Fluids* 28.1 (2016), p. 017102.

[26] Michael Shusser and Morteza Gharib. “Energy and velocity of a forming vortex ring”. In: *Physics of Fluids* 12.3 (2000), pp. 618–621.

[27] A Weigand and M Gharib. “On the evolution of laminar vortex rings”. In: *Experiments in Fluids* 22.6 (1997), pp. 447–457.

[28] *Drag of blunt bodies and streamlined bodies*. 2007. URL: https://www.princeton.edu/~asmits/Bicycle_web/blunt.html.

[29] Deepak Adhikari. “Some experimental studies on vortex ring formation and interaction”. In: (2009).

[30] Roger King. “A review of vortex shedding research and its application”. In: *Ocean Engineering* 4.3 (1977), pp. 141–171.

[31] Jie-Zhi Wu, Hui-Yang Ma, and Ming-De Zhou. *Vortical flows*. Vol. 28. Springer, 2015.

[32] Charles HK Williamson. “Vortex dynamics in the cylinder wake”. In: *Annual review of fluid mechanics* 28.1 (1996), pp. 477–539.

[33] David Jeon and Morteza Gharib. “On the relationship between the vortex formation process and cylinder wake vortex patterns”. In: *Journal of Fluid Mechanics* 519 (2004), pp. 161–181.

[34] Ludwig Prandtl. “Über Flussigkeitsbewegung bei sehr kleiner Reibung”. In: *Verhandl. III, Internat. Math.-Kong., Heidelberg, Teubner, Leipzig, 1904* (1904), pp. 484–491.

[35] Frank M White and Joseph Majdalani. *Viscous fluid flow*. Vol. 3. McGraw-Hill New York, 2006.

[36] Jérome Hœpffner and Marco Antonio Fontelos. “A model for the global structure of self-similar vortex sheet roll-up”. In: 2013.

[37] Morteza Gharib, Edmond Rambod, and Karim Shariff. “A universal time scale for vortex ring formation”. In: *Journal of Fluid Mechanics* 360 (1998), pp. 121–140.

[38] Clara O’Farrell. “A dynamical systems analysis of vortex pinch-off”. PhD thesis. California Institute of Technology, 2013.

[39] RJ Munro and MR Foster. “Vortex evolution in a rotating tank with an off-axis drain”. In: *Journal of Fluid Mechanics* 933 (2022).

[40] Christopher E Brennen. “An internet book on fluid dynamics”. In: *INDEX for INTERNET BOOK ON FLUID DYNAMICS* (2006).

[41] Xikun Wang et al. “Experimental investigation of flow past a confined bluff body: Effects of body shape, blockage ratio and Reynolds number”. In: *Ocean Engineering* 220 (2021), p. 108412.

[42] SP Singh and SANJAY Mittal. “Flow past a cylinder: shear layer instability and drag crisis”. In: *International journal for numerical methods in fluids* 47.1 (2005), pp. 75–98.

[43] Angel Rodriguez Sevillano et al. “Flow study over bluff bodies based on visualization technique”. In: 2017.

[44] SCR Dennis et al. “Viscous flow normal to a flat plate at moderate Reynolds numbers”. In: *Journal of Fluid Mechanics* 248 (1993), pp. 605–635.

[45] Arun K Saha. “Far-wake characteristics of two-dimensional flow past a normal flat plate”. In: *Physics of Fluids* 19.12 (2007), p. 128110.

[46] Fady M Najjar and Surya Pratap Vanka. “Effects of intrinsic three-dimensionality on the drag characteristics of a normal flat plate”. In: *Physics of fluids* 7.10 (1995), pp. 2516–2518.

[47] PA t Smith and PK Stansby. “Impulsively started flow around a circular cylinder by the vortex method”. In: *Journal of Fluid Mechanics* 194 (1988), pp. 45–77.

[48] SP Das, U Srinivasan, and JH Arakeri. “Unsteady separation and vortex shedding from a laminar separation bubble over a bluff body”. In: *Journal of Fluids and Structures* 40 (2013), pp. 233–245.

[49] Hiroyuki Honji and Sadatoshi Taneda. “Unsteady flow past a circular cylinder”. In: *Journal of the physical society of Japan* 27.6 (1969), pp. 1668–1677.

[50] Roger Bouard and Madeleine Coutanceau. “The early stage of development of the wake behind an impulsively started cylinder for 40< Re< 104”. In: *Journal of Fluid Mechanics* 101.3 (1980), pp. 583–607.

[51] Turgut Sarpkaya. “Nonimpulsively started steady flow about a circular cylinder”. In: *AIAA journal* 29.8 (1991), pp. 1283–1289.

[52] Sadatoshi Taneda and Hiroyuki Honji. “Unsteady flow past a flat plate normal to the direction of motion”. In: *Journal of the Physical Society of Japan* 30.1 (1971), pp. 262–272.

[53] P Koumoutsakos and D Shiels. “Simulations of the viscous flow normal to an impulsively started and uniformly accelerated flat plate”. In: *Journal of Fluid Mechanics* 328 (1996), pp. 177–227.

[54] Ling Xu and Monika Nitsche. “Start-up vortex flow past an accelerated flat plate”. In: *Physics of Fluids* 27.3 (2015), p. 033602.

[55] Q-X Lian and Z Huang. “Starting flow and structures of the starting vortex behind bluff bodies with sharp edges”. In: *Experiments in Fluids* 8.1 (1989), pp. 95–103.

[56] Derek Lee Ashton Lisoski. “Nominally two-dimensional flow about a normal flat plate”. PhD thesis. California Institute of Technology, 1993.

[57] Christoffer Norberg. “An experimental investigation of the flow around a circular cylinder: influence of aspect ratio”. In: *Journal of Fluid Mechanics* 258 (1994), pp. 287–316.

[58] Matthew J Ringuette, Michele Milano, and Morteza Gharib. “Role of the tip vortex in the force generation of low-aspect-ratio normal flat plates”. In: *Journal of Fluid Mechanics* 581 (2007), pp. 453–468.

[59] *Bluff Body, Viscous Flow Characteristics*. URL: http://www2.latech.edu/~sajones/June/Study%20Guides/chVIIb.pdf.

[60] CE Brennen. “A Review of Added Mass and Fluid Inertial Forces.” In: (1982).

[61] Yee-Tak Yu. “Virtual masses of rectangular plates and parallelepipeds in water”. In: *Journal of Applied Physics* 16.11 (1945), pp. 724–729.

[62] SJ Corkery, Holger Babinsky, and WR Graham. “Quantification of added-mass effects using particle image velocimetry data for a translating and rotating flat plate”. In: *Journal of Fluid Mechanics* 870 (2019), pp. 492–518.

[63] Joshua N Galler, Gabriel D Weymouth, and David E Rival. “On the concept of energized mass: A robust framework for low-order force modeling in flow past accelerating bodies”. In: *Physics of Fluids* 33.5 (2021), p. 057103.

[64] Joshua N Galler, Gabriel D Weymouth, and David E Rival. “Progress towards modelling unsteady forces using a drift-volume approach”. In: *AIAA Scitech 2019 Forum*. 2019, p. 1147.

[65] John O Dabiri. “Note on the induced Lagrangian drift and added-mass of a vortex”. In: *Journal of Fluid Mechanics* 547 (2006), pp. 105–113.

[66] Jifeng Peng and John O Dabiri. “An overview of a Lagrangian method for analysis of animal wake dynamics”. In: *Journal of Experimental Biology* 211.2 (2008), pp. 280–287.

[67] Yang Xiang et al. “Quantitative analysis of vortex added-mass and impulse generation during vortex ring formation based on elliptic Lagrangian coherent structures”. In: *Experimental Thermal and Fluid Science* 94 (2018), pp. 295–303.

[68] Giuseppe A Rosi and David E Rival. “A Lagrangian perspective towards studying entrainment”. In: *Experiments in Fluids* 59.1 (2018), pp. 1–17.

[69] Ali B Olcay and Paul S Krueger. “Measurement of ambient fluid entrainment during laminar vortex ring formation”. In: *Experiments in Fluids* 44.2 (2008), pp. 235–247.

[70] Octave Levenspiel. “Non-Newtonian Fluids”. In: *Engineering Flow and Heat Exchange*. Springer, 2014, pp. 99–131.

[71] A. Hallberg Kristensen. “Flow properties of water-based drilling fluids”. In: 2013.

[72] Ildebrando Pérez-Reyes et al. “Applications of Viscoelastic Fluids Involving Hydrodynamic Stability and Heat Transfer”. In: *Polymer Rheology* (2018), p. 29.

[73] Eric Lauga. “Propulsion in a viscoelastic fluid”. In: *Physics of Fluids* 19.8 (2007), p. 083104.

[74] C. W. MACOSKO. “Rheology Principles”. In: *Measurements and Applications* (1994). URL: https://ci.nii.ac.jp/naid/10005741026/en/.

[75] Pauline Banes. *Viscoelastic behavior - dielectric properties*. 2021. URL: https://www.europeanmedical.info/dielectric-properties/viscoelastic-behavior.html.

[76] Marc André Meyers and Krishan Kumar Chawla. *Mechanical behavior of materials*. Cambridge university press, 2008.

[77] Syed Ali Ashter. *Thermoforming of Single and Multilayer Laminates: Plastic Films Technologies, Testing, and Applications*. William Andrew, 2013.

[78] *An introduction to solid mechanics*. URL: https://pkel015.connect.amazon.auckland.ac.nz/SolidMechanicsBooks/Part_I/index.html.

[79] MA Alves, FTd Pinho, and Paulo J Oliveira. “Viscoelastic flow in a 3D square/square contraction: visualizations and simulations”. In: *Journal of Rheology* 52.6 (2008), pp. 1347–1368.

[80] Nickolas D Polychronopoulos and John Vlachopoulos. “Polymer processing and rheology”. In: *Functional Polymers. Polymers and Polymeric Composites: A Reference Series; Jafar Mazumder, M., Sheardown, H., Al-Ahmed, A., Eds* (2018).

[81] Diego Hayashi Alonso, Juan Sergio Romero Saenz, and Emilio Carlos Nelli Silva. “Non-newtonian laminar 2D swirl flow design by the topology optimization method”. In: *Structural and Multidisciplinary Optimization* 62.1 (2020), pp. 299–321.

[82] Samuel Gaudet and Gareth H McKinley. “Extensional deformation of non-Newtonian liquid bridges”. In: *Computational mechanics* 21.6 (1998), pp. 461–476.

[83] DV Boger and YL Yeow. “The impact of ideal elastic liquids in the development of non-Newtonian fluid mechanics”. In: *Experimental thermal and fluid science* 5.5 (1992), pp. 633–640.

[84] DV Boger. “A highly elastic constant-viscosity fluid”. In: *Journal of Non-Newtonian Fluid Mechanics* 3.1 (1977), pp. 87–91.

[85] MRJ Verhoef, BHAA Van den Brule, and MA Hulsen. “On the modelling of a PIB/PB Boger fluid in extensional flow”. In: *Journal of non-newtonian fluid mechanics* 80.2-3 (1999), pp. 155–182.

[86] Seo Gyun Kim, Chang Min Ok, and Heon Sang Lee. “Steady-state extensional viscosity of a linear polymer solution using a differential pressure extensional rheometer on a chip”. In: *Journal of Rheology* 62.5 (2018), pp. 1261–1270.

[87] David F James. “Boger fluids”. In: *Annual Review of Fluid Mechanics* 41 (2009), pp. 129–142.

[88] LE Becker et al. “The unsteady motion of a sphere in a viscoelastic fluid”. In: *Journal of Rheology* 38.2 (1994), pp. 377–403.

[89] JE López-Aguilar et al. “Numerical vs experimental pressure drops for Boger fluids in sharp-corner contraction flow”. In: *Physics of Fluids* 28.10 (2016), p. 103104.

[90] Sujit S Datta et al. “Perspectives on viscoelastic flow instabilities and elastic turbulence”. In: *arXiv preprint arXiv:2108.09841* (2021).

[91] *An introduction to solid mechanics*. URL: https://pkel015.connect.amazon.auckland.ac.nz/SolidMechanicsBooks/Part_I/index.html.

[92] GC Papanicolaou and SP Zaoutsos. “Viscoelastic constitutive modeling of creep and stress relaxation in polymers and polymer matrix composites”. In: *Creep and fatigue in polymer matrix composites*. Elsevier, 2019, pp. 3–59.

[93] Andrew Hazel. “Constitutive modelling”. In: (). URL: https://personalpages.manchester.ac.uk/staff/Andrew.Hazel/MATH45061/MATH45061_Ch5.pdf.

[94] LJ Amoreira and PJ Oliveira. “Comparison of different formulations for the numerical calculation of unsteady incompressible viscoelastic fluid flow”. In: *Adv. Appl. Math. Mech* 2.4 (2010), pp. 483–502.

[95] JH Snoeijer et al. “The relationship between viscoelasticity and elasticity”. In: *Proceedings of the Royal Society A* 476.2243 (2020), p. 20200419.

[96] E. J. Hinch. *Introduction to non-newtonian fluids*. URL: https://www.whoi.edu/cms/files/lecture01_28325.pdf.

[97] King-Hay Yang. *Basic finite element method as applied to injury biomechanics*. Academic Press, 2017.

[98] *Introduction to rheology*. URL: https://projects.iq.harvard.edu/files/weitzlab/files/introductiontorheology2.pdf.

[99] Dimitri Feys et al. “Measuring rheological properties of cement pastes: most common techniques, procedures and challenges”. In: *RILEM technical letters* 2 (2018), pp. 129–135.

[100] Edwin Wang. *Slow flow of a viscoelastic fluid past a circular cylinder*. URL: https://tspace.library.utoronto.ca/bitstream/1807/32289/3/Wang_Edwin_SW_20123_MASc_thesis.pdf.

[101] *Amplitude sweeps :: Anton Paar Wiki*. URL: https://wiki.anton-paar.com/en/amplitude-sweeps/.

[102] *Training manual UCSB*. URL: https://www.mrl.ucsb.edu/sites/default/files/mrl_docs/instruments/rheo_man_0.pdf.

[103] *Oscillatory test lecture notes*. URL: https://zeus.plmsc.psu.edu/~manias/MatSE447/07_OscillatoryShear.pdf.

[104] Webdesign Basel amp; Zürich JKweb. *LS Instruments*. URL: https://lsinstruments.ch/en/theory/rheology/maxwell-model.

[105] Wikipedia Contributors. *Time–temperature superposition*. 2022. URL: https://en.wikipedia.org/wiki/Time-temperature_superposition.

[106] Laura Campo-Deaño et al. “Flow of low viscosity Boger fluids through a microfluidic hyperbolic contraction”. In: *Journal of Non-Newtonian Fluid Mechanics* 166.21-22 (2011), pp. 1286–1296.

[107] *J.Ferry,Chapter-11*. URL: https://zeus.plmsc.psu.edu/~manias/MatSE447/10_TimeTemperSuperposition.pdf.

[108] Malcolm L Williams, Robert F Landel, and John D Ferry. “The temperature dependence of relaxation mechanisms in amorphous polymers and other glass-forming liquids”. In: *Journal of the American Chemical society* 77.14 (1955), pp. 3701–3707.

[109] Dariusz Niedziela. “On numerical simulations of viscoelastic fluids.” In: (2006).

[110] Francisco J Galindo-Rosales, MA Alves, and Mónica SN Oliveira. “Microdevices for extensional rheometry of low viscosity elastic liquids: a review”. In: *Microfluidics and nanofluidics* 14.1-2 (2013), pp. 1–19.

[111] Raj P Chhabra and John Francis Richardson. *Non-Newtonian flow and applied rheology: engineering applications*. Butterworth-Heinemann, 2011.

[112] Jeongin Han and Chongyoup Kim. “Spreading of Boger fluid on horizontal surface”. In: *Journal of Non-Newtonian Fluid Mechanics* 202 (2013), pp. 120–130.

[113] JA Odell and SP Carrington. “Extensional flow oscillatory rheometry”. In: *Journal of non-newtonian fluid mechanics* 137.1-3 (2006), pp. 110–120.

[114] VM Ribeiro et al. “Viscoelastic fluid flow past a confined cylinder: Three-dimensional effects and stability”. In: *Chemical engineering science* 111 (2014), pp. 364–380.

[115] MA Alves, FTd Pinho, and Paulo J Oliveira. “Visualizations of Boger fluid flows in a 4: 1 square–square contraction”. In: *AIChE journal* 51.11 (2005), pp. 2908–2922.

[116] KP Jackson, K Walters, and RW Williams. “A rheometrical study of boger fluids”. In: *Journal of Non-Newtonian Fluid Mechanics* 14 (1984), pp. 173–188.

[117] RV Maitri et al. “Effect of microchannel structure and fluid properties on non-inertial particle migration”. In: *Soft Matter* 15.12 (2019), pp. 2648–2656.

[118] Tienyi T Hsu et al. “Role of fluid elasticity on the dynamics of rinsing flow by an impinging jet”. In: *Physics of Fluids* 23.3 (2011), p. 033101.

[119] Alessandro Cubeddu. “Prediction of High-speed Extrusion by Means of a Hybrid-Neural-Numerical Process Control Strategy”. PhD thesis. Jan. 2017.

[120] Francesco Del Giudice, Simon J Haward, and Amy Q Shen. “Relaxation time of dilute polymer solutions: A microfluidic approach”. In: *Journal of Rheology* 61.2 (2017), pp. 327–337.

[121] Christopher M White and M Godfrey Mungal. “Mechanics and prediction of turbulent drag reduction with polymer additives”. In: *Annu. Rev. Fluid Mech.* 40 (2008), pp. 235–256.

[122] *Polymer solutions*. URL: http://soft-matter.seas.harvard.edu/index.php/Polymer_solutions.

[123] Shelley L Anna and Gareth H McKinley. “Elasto-capillary thinning and breakup of model elastic liquids”. In: *Journal of Rheology* 45.1 (2001), pp. 115–138.

[124] Lucy E Rodd et al. “Capillary break-up rheometry of low-viscosity elastic fluids”. In: *Applied Rheology* 15.1 (2005), pp. 12–27.

[125] A Deblais et al. “Self-similarity in the breakup of very dilute viscoelastic solutions”. In: *Journal of Fluid Mechanics* 904 (2020).

[126] Uddalok Sen et al. “The retraction of jetted slender viscoelastic liquid filaments”. In: *arXiv preprint arXiv:2102.08876* (2021).

[127] Jens Eggers, Miguel Angel Herrada, and JH Snoeijer. “Self-similar breakup of polymeric threads as described by the Oldroyd-B model”. In: *Journal of fluid mechanics* 887 (2020).

[128] *The oldroyd-b fluid*. URL: https://www.ucl.ac.uk/~ucahhwi/GM05/lecture6.pdf.

[129] Gareth H McKinley et al. “Extensional rheometry of polymeric fluids and the uniaxial elongation of viscoelastic filaments”. In: *15th International Polymer Processing Society, Netherlands* 83 (1999), pp. 653–670.

[130] RJ Poole. “The deborah and weissenberg numbers”. In: *Rheol. Bull* 53.2 (2012), pp. 32–39.

[131] David F James and Allan J Acosta. “The laminar flow of dilute polymer solutions around circular cylinders”. In: *Journal of Fluid Mechanics* 42.2 (1970), pp. 269–288.

[132] PY Huang and J Feng. “Wall effects on the flow of viscoelastic fluids around a circular cylinder”. In: *Journal of non-newtonian fluid mechanics* 60.2-3 (1995), pp. 179–198.

[133] YL Xiong, Charles-Henri Bruneau, and D Yang. “Numerical study on viscoelastic fluid flow past a rigid body”. In: *Applied Mathematical Modelling* 42 (2017), pp. 188–208.

[134] PM Coelho and FT Pinho. “Vortex shedding in cylinder flow of shear-thinning fluids: I. Identification and demarcation of flow regimes”. In: *Journal of non-newtonian fluid mechanics* 110.2-3 (2003), pp. 143–176.

[135] Christopher Pipe. *Experiments investigating the effects of fluid elasticity on laminar vortex shedding from a cylinder*. Tech. rep. EPFL, 2005.

[136] Mehmet Sahin and Robert G Owens. “On the effects of viscoelasticity on two-dimensional vortex dynamics in the cylinder wake”. In: *Journal of non-newtonian fluid mechanics* 123.2-3 (2004), pp. 121–139.

[137] Gareth H McKinley, Robert C Armstrong, and Robert Brown. “The wake instability in viscoelastic flow past confined circular cylinders”. In: *Philosophical Transactions of the Royal Society of London. Series A: Physical and Engineering Sciences* 344.1671 (1993), pp. 265–304.

[138] Boyang Qin et al. “Upstream vortex and elastic wave in the viscoelastic flow around a confined cylinder”. In: *Journal of fluid mechanics* 864 (2019).

[139] Robert A Hermes and AG Fredrickson. “Flow of viscoelastic fluids past a flat plate”. In: *AIChE Journal* 13.2 (1967), pp. 253–259.

[140] Junseong Lee et al. “Unsteady flow of shear-thickening fluids around an impulsively moving circular cylinder”. In: *Journal of Non-Newtonian Fluid Mechanics* 272 (2019), p. 104163.

[141] MD Atkins. “Velocity field measurement using particle image velocimetry (PIV)”. In: *Application of Thermo-Fluidic Measurement Techniques*. Elsevier, 2016, pp. 125–166.

[142] Markus Raffel, Christian E Willert, Jürgen Kompenhans, et al. *Particle image velocimetry: a practical guide*. Vol. 2. Springer, 1998.

[143] *PIV digital book*. 2022. URL: http://pivbook.org/digital-content/historical-background/index.html.

[144] Sven Scharnowski and Christian J Kähler. “Particle image velocimetry-Classical operating rules from today’s perspective”. In: *Optics and Lasers in Engineering* 135 (2020), p. 106185.

[145] Eize J Stamhuis. “Basics and principles of particle image velocimetry (PIV) for mapping biogenic and biologically relevant flows”. In: *Aquatic Ecology* 40.4 (2006), pp. 463–479.

[146] Bernhard Wieneke. “PIV uncertainty quantification from correlation statistics”. In: *Measurement Science and Technology* 26.7 (2015), p. 074002.

[147] Alireza Mirsepassi and Derek Dunn Rankin. “Particle image velocimetry in viscoelastic fluids and particle interaction effects”. In: *Experiments in fluids* 55.1 (2014), pp. 1–7.

[148] Jian Zhou and Ian Papautsky. “Viscoelastic microfluidics: Progress and challenges”. In: *Microsystems & Nanoengineering* 6.1 (2020), pp. 1–24.

[149] Pinaki Chakraborty, Sivaramakrishnan Balachandar, and Ronald J Adrian. “On the relationships between local vortex identification schemes”. In: *Journal of fluid mechanics* 535 (2005), pp. 189–214.

[150] George Haller. “Lagrangian coherent structures”. In: *Annual Review of Fluid Mechanics* 47 (2015), pp. 137–162.

[151] *LCS tutorial*. 2022. URL: https://shaddenlab.berkeley.edu/uploads/LCS-tutorial/motivation.html.

[152] M Ament et al. “GPU-based two-dimensional flow simulation steering using coherent structures”. In: *Proceedings of the Second International Conference on Parallel, Distributed, Grid and Cloud Computing for Engineering (Stirlingshire, United Kingdom, 2011), Iványi P., Topping BHV,(Eds.), Civil-Comp Press. doi: http://dx. doi. org/10.4203/ccp*. Vol. 95. 2011, p. 18.

[153] Shawn C Shadden, Francois Lekien, and Jerrold E Marsden. “Definition and properties of Lagrangian coherent structures from finite-time Lyapunov exponents in two-dimensional aperiodic flows”. In: *Physica D: Nonlinear Phenomena* 212.3-4 (2005), pp. 271–304.

[154] Matthew Rockwood, Yangzi Huang, and Melissa Green. “Tracking coherent structures in massively-separated and turbulent flows”. In: *Physical Review Fluids* 3.1 (2018), p. 014702.

[155] Justin Finn and Sourabh V Apte. “Integrated computation of finite-time Lyapunov exponent fields during direct numerical simulation of unsteady flows”. In: *Chaos: An Interdisciplinary Journal of Nonlinear Science* 23.1 (2013), p. 013145.

[156] George Haller. “A variational theory of hyperbolic Lagrangian coherent structures”. In: *Physica D: Nonlinear Phenomena* 240.7 (2011), pp. 574–598.

[157] Mohammad Farazmand and George Haller. “Computing Lagrangian coherent structures from their variational theory”. In: *Chaos: An Interdisciplinary Journal of Nonlinear Science* 22.1 (2012), p. 013128.

[158] George Haller et al. “Defining coherent vortices objectively from the vorticity”. In: *Journal of Fluid Mechanics* 795 (2016), pp. 136–173.

[159] Gregory Kamykowski. *TA instruments Rheology ppt*. URL: https://www.tainstruments.com/wp-content/uploads/2019-04-AM-Rheology.pdf.

[160] Agustín Trujillo-Pino et al. “Accurate subpixel edge location based on partial area effect”. In: *Image and Vision Computing* 31.1 (2013), pp. 72–90.

[161] Macosko CW. *Rheology: principles, measurements and applications*. 1994.

[162] GS West and CJ Apelt. “The effects of tunnel blockage and aspect ratio on the mean flow past a circular cylinder with Reynolds numbers between 104 and 105”. In: *Journal of Fluid mechanics* 114 (1982), pp. 361–377.

[163] Andreas Volk and Christian J Kähler. “Density model for aqueous glycerol solutions”. In: *Experiments in Fluids* 59.5 (2018), pp. 1–4.

[164] Lara Adrian, Ronald J Adrian, and Jerry Westerweel. *Particle image velocimetry*. 30. Cambridge university press, 2011.

[165] EFJ Overmars. “Bias errors in PIV: the pixel locking effect revisited. EFJ Overmars, NGW Warncke, C. Poelma and J. Westerweel”. In: ().

[166] Jerry Westerweel and Fulvio Scarano. “Universal outlier detection for PIV data”. In: *Experiments in fluids* 39.6 (2005), pp. 1096–1100.

[167] Alireza Hadjighasem et al. “A critical comparison of Lagrangian methods for coherent structure detection”. In: *Chaos: An Interdisciplinary Journal of Nonlinear Science* 27.5 (2017), p. 053104.

[168] Yangzi Huang. “Vortex detection and tracking in massively separated and turbulent flows”. PhD thesis. Syracuse University, 2018.

[169] Daniel F Carlson et al. “Deducing an upper bound to the horizontal eddy diffusivity using a stochastic Lagrangian model”. In: *Environmental fluid mechanics* 10.5 (2010), pp. 499–520.

[170] Sung-Ik Sohn. “Singularity formation and nonlinear evolution of a viscous vortex sheet model”. In: *Physics of Fluids* 25.1 (2013), p. 014106.

[171] Michael Shusser and Morteza Gharib. “A model for vortex ring formation in a starting buoyant plume”. In: *Journal of Fluid Mechanics* 416 (2000), pp. 173–185.

[172] Yasuhide Fukumoto. “Kinematic variational principle for vortical structure of Euler flows and beyond (Modern approach and developments to Onsager’s theory on statistical vortices)”. In: □□□□□□□□□□ 1798 (2012), pp. 198–212.

[173] Ionut Danaila, Felix Kaplanski, and Sergei S Sazhin. *Vortex Ring Models*. Springer, 2021.

[174] Jia Cheng Hu. “An exploration of isolated vortex collisions”. In: (2021).

[175] *what is linear viscoelasticity?* URL: https://academic.csuohio.edu/duffy_s/Linear_Visco.pdf.

[176] Ali Minaeian et al. “Effects of viscoelasticity on the onset of vortex shedding and forces applied on a cylinder in unsteady flow regime”. In: *Physics of Fluids* 34.1 (2022), p. 013106.

[177] John O Dabiri. “On the estimation of swimming and flying forces from wake measurements”. In: *The Journal of Experimental Biology* 208 (), pp. 3519–3532.

[178] Charles Darwin. “Note on hydrodynamics”. In: *Mathematical Proceedings of the Cambridge Philosophical Society*. Vol. 49. 2. Cambridge University Press. 1953, pp. 342–354.

[179] George Keith Batchelor. *An introduction to fluid dynamics*. Cambridge university press, 2000.

[180] Beverley Green. *Fluid vortices*. Vol. 30. Springer Science & Business Media, 1995.

[181] John N Fernando and David E Rival. “Reynolds-number scaling of vortex pinch-off on low-aspect-ratio propulsors”. In: *Journal of Fluid Mechanics* 799 (2016).